Diploma Thesis

Pulse Profile Decomposition of the Accreting X-ray Pulsar V0332+53

submitted by

Daniela Müller

September, 2010

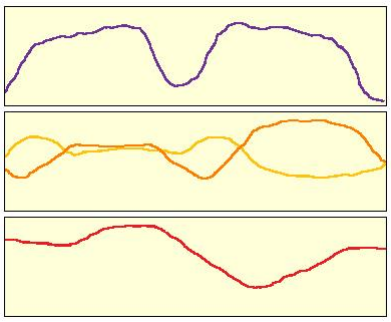

Institut für Astronomie and Astrophysik

Eberhard Karls Universität Tübingen

Pulsprofilzerlegung des akkretierenden Röntgenpulsares V0332+53

Inhalt

Im Rahmen dieser Diplomarbeit wurde der akkretierende Röntgenpulsar V0332+53 analysiert und die genaue Lage der magnetischen Pole bestimmt. Das Ziel der Arbeit bestand darin, mit Hilfe der von Ute Kraus entwickelten Methode der Pulsprofilzerlegung die genaue Position der magnetischen Pole zu bestimmen und für jeden Pol eine Strahlungscharakteristik zu erstellen. Um diese Methode anzuwenden müssen jedoch einige Annahmen gemacht werden: Die Asymmetrie der Pulsprofile kommt von den beiden nicht genau gegenüberliegenden Magnetpolen und die jeweiligen Emissionsgebiete sind gleich, wobei jeder der Pole ein symmetrisches Emissionsprofil besitzt. Die Idee der Zerlegungsmethode ist es, die Pulsprofile durch eine Fourier-Reihe darzustellen, und diese daraufhin in die jeweiligen Beiträge der einzelnen Pole zu zerlegen. Diese beiden Einzelpolkomponenten kann man daraufhin in Strahlungsprofile umwandeln und erhält durch deren Überlagerung die gesamte einsehbare Strahlungscharakteristik eines einzelnen Poles. Da Neutronensterne sehr kompakte Objekte wurden abschließend noch die Effekte der relativistischen Lichtablenkung berücksichtigt, um die intrinsische Emissionscharakteristik eines einzelnen Poles zu erhalten.

V0332+53 ist ein Be-Doppelsternsystem und besteht aus einem Röntgenpulsar mit Pulsationsperiode $P_{\mathrm{pulse}} \approx 4.375\,\mathrm{s}$ und dem optischen Begleitstern BQ Cam. Das System befindet sich in einer Entfernung von etwa 7 kpc und wurde 1973 während eines Typ II Ausbruches entdeckt. Die für unsere Analyse verwendeten Daten wurden vom Röntgensatelliten RXTE (Rossi X-ray Timing Explorer) aufgezeichnet und stammen von einem sehr starken Ausbruch der Quelle, der von Dezember 2004 bis Februar 2005 andauerte. Die maximale Leuchtkraft erreichte dabei Werte von 1 bis 2 Crab.

Um die Quelle genauer analysieren zu können, wurden die Daten zunächst reduziert und anschließend Lichtkurven für die verschiedenen Beobachtungen von RXTE erstellt. Mit den gemessenen Lichtkurven und den daraus berechneten Pulsperioden wurden für vier Energiebereiche ($0 - 7\,\mathrm{keV}$, $7 - 20\,\mathrm{keV}$, $20 - 30\,\mathrm{keV}$ und $> 30\,\mathrm{keV}$) Pulsprofile erstellt. Die so erhaltenen Pulsprofile hängen dabei sowohl von der Leuchtkraft des Systems, als auch vom Energiebereich ab. Zudem sind die Pulsprofile auffällig asymmetrisch, woraus abgeleitet wird, dass die beiden magnetischen Pole des Neutronensternes nicht genau gegenüber voneinander liegen, es sich also um keinen exakten Dipol handelt.

Die Methode der Pulsprofilzerlegung wurde für V0332+53 durchgeführt. Dabei entstanden verschiedene Bereiche, in denen gute Zerlegungen vorhanden waren. Nach Anwendung aller Schritte und Auswertung der Lösungen, reduzierte sich die Anzahl guter Regionen auf zwei: Region C ($\phi_1 = 55 - 100$, $\Delta = 3 - 21$) und Region G ($\phi_1 = 0 - 40$, $\Delta = 50 - 75$). Von diesen beiden Lösungen wird die von Region C bevorzugt, da deren Ergebnis sehr ähnlich zu Zerlegungen anderer Quellen, wie zum Beispiel von Her X-1 oder Cen X-3, ist und wir die Emissionscharakteristiken daher mit dem Modell einer hohlen Akkretionssäule erklären können. Dabei geht man davon aus, dass die Materie, welche auf die magnetischen Pole des Neutronenstromes akkretiert wird, in Form einer Hohlsäule auf den Pol herabgeht. Für kleine Leuchtkräfte beobachtet man daher die Strahlung, welche direkt vom Gebiet des magnetischen Pols und von der darum liegenden Corona stammt, während sich für höhere Leuchtkräfte zusätzliche Strukturen ergeben.

Bei dieser Analyse wurde gezeigt, dass das Modell einer hohlen Akkretionssäule auch durch die Pulsprofilzerlegung von V0332+53 bekräftigt wird. Zudem konnten wir eine mögliche Position der beiden Pole bestimmen. Für eine Lösung in der bevorzugten Region C ergibt sich eine Position der Pole bei $\phi_1 = 100°$, $\Theta_1 = 38°$ und $\phi_2 = 295°$, $\Theta_2 = 142°$, während die magnetischen Pole bei der Lösung im Gebiet G bei $\phi_1 = 12°$, $\Theta_1 = 30°$ und $\phi_2 = 260°$, $\Theta_2 = 150°$ liegen. Ob die Akkretion auf den Neutronenstern für diese Klasse von Röntgendoppelsternsystemen wirklich in Form einer Hohlsäule geschieht, bleibt zu untersuchen.

Pulse Profile Decomposition of the Accreting X-ray Pulsar V0332+53

Abstract

The subject of this diploma thesis is the analysis and modeling of the accreting X-ray pulsar V0332+53. V0332+53 is a Be-/X-ray binary system, located at a distance of about 7 kpc. It consists of a neutron star with a pulse period of about $P_{\mathrm{pulse}} = 4.375\,\mathrm{s}$ and a companion star, namely BQ Cam. The system was discovered in 1973 by the Vela satellites during a bright outburst of type II. The outburst, which we analyzed during this work is the bright type II outburst of 2004/2005. For this analysis, we used data from the X-ray satellite RXTE (Rossi X-ray Timing Explorer), which measured a peak luminosity of 1-2 Crab.

The aim of this work is to estimate the exact position of the two magnetic poles of the neutron star and to produce an intrinsic beam pattern for each of them. To do this, we applied the method of pulse profile decomposition, described in Kraus et al. (1995). This method is based on some fundamental assumptions: The observed asymmetry in the pulse profiles is thought to originate from a displaced magnetic field and each emission region is thought to be symmetric and equal to the other one. The idea of the decomposition method is, to decompose the pulse profiles into their respective Fourier sums and hereupon to separate the contributions from each pole. The two single-pole contribution can then be transformed into a section of beam pattern. By overlaying similar sections of beam patterns from the two poles we get the total observed section of the beam pattern. Due to the high compactness of a neutron star, the beam patterns are finally transformed into intrinsic beam patterns by taking into account the effects of relativistic light deflection.

First of all, we performed data reduction to get lightcurves for the various observations of RXTE. Using those lightcurves we calculated the pulse period and then produced pulse profiles. We did this for four energy bands: $0-7\,\mathrm{keV}$, $7-20\,\mathrm{keV}$, $20-30\,\mathrm{keV}$ and for $\mathrm{E} > 30\,\mathrm{keV}$. The pulse profiles show a notable asymmetry, as well as a strong dependence on the source luminosity and the energy band. One idea is that this asymmetry arises from the two non-antipodal magnetic poles.

We applied the pulse profile decomposition method to V0332+53 and got various regions with acceptable decompositions. We were able to reduce the number of good decompositions by using certain criteria and by comparing the results for the different regions. At the end, two good regions emerged characterized by $\phi_1 = 55-100$, $\Delta = 3-21$ (region C) and $\phi_1 = 0-40$, $\Delta = 50-75$ (region G). We

favor the first solution because the beam patterns look very similar to those of other sources and can also be described using the same model of a hollow column. In this model, it is thought that the accreted matter goes down onto the magnetic poles of the neutron star in form of a hollow column. For low source luminosities, we observe the emission from the surrounding corona and from the magnetic poles itself, whereas for higher luminosities, we get additional components originating from the inner and outer walls of the hollow column.

The pulse profile decomposition of V0332+53 showed, that also for this source the model of a hollow accretion column can give an accurate description of all the observed emission features. Additionally, we were able to determine the position of the two magnetic poles of the neutron star. For our favored solution, the one of region C, the poles are located at $\phi_1 = 100°$, $\Theta_1 = 38°$ and $\phi_2 = 295°$, $\Theta_2 = 142°$, while for the solution of region G, we got a position of $\phi_1 = 12°$, $\Theta_1 = 30°$ and $\phi_2 = 260°$, $\Theta_2 = 150°$. Further analysis of other X-ray sources could confirm the applied method of pulse profile decomposition, as well as the hollow column accretion model.

Contents

List of Figures

List of Tables

Chapter 1

Neutron stars, pulsars and accretion

1.1 Introduction to neutron stars

1.1.1 History

According to the explanations of Trümper and Hasinger in their book *The Universe in X-rays* (Trümper & Hasinger, 2008), the original idea of the existence of a neutron star evolved in the early 30's as the questions emerged: What happens to a star after having burned all its nuclear fuel and hereupon, how can a star sustain against gravity? What about a star that consists entirely of neutrons? Subrahmanyan Chandrasekhar asked himself this question shortly after the first discovery of the neutron in 1932. Not long after, Walter Baade and Fritz Zwicky had the idea of neutron stars formed out of supernova explosions (see e.g. Zwicky, 1938). It didn't take long until the first models for neutron stars were made by Oppenheimer and Volkoff in 1939 (Oppenheimer & Volkoff, 1939). The big question was: how we can observe neutron stars to get a real evidence for their existence? As nobody had a good idea how to do this, there wasn't much going on for the following years.

This changed as the first radio pulsar (PSR1919+21) was discovered by Jocelyn Bell, a student of Antoni Hewish in 1967 (Hewish et al., 1968). A discovery, for which Hewish got the Nobel Prize in 1974. Soon after this monumental discovery, two of the most famous pulsars were detected, the Crab pulsar in the Crab Nebula and the Vela pulsar, each of them in the corresponding supernova remnants (Trümper & Hasinger, 2008). This, by the way, corroborated the idea of Baade and Zwicky. Another big step in neutron star physics was the launch of the satellite UHURU in 1970, which operated until 1973. UHURU detected pulsations from the accreting X-ray binary pulsar Cen X-3 (Giacconi et al., 1971)

as well as 338 other X-ray sources, listed in the *4th Uhuru catalogue*. Among those sources are binaries, supernova remnants, Seyfert galaxies and cluster of galaxies (*http://heasarc.gsfc.nasa.gov/docs/uhuru/uhuru.html*). In 1976, Trümper et al. (Trümper et al., 1978, 1977) measured the magnetic field of a neutron star for the first time. They analyzed the spectrum of the prominent source Her X-1 and observed a cyclotron line at an energy of about 58 keV, which was thought to be caused by a magnetic field of $B \approx 5.3 \cdot 10^{12}$ G.

1.1.2 General information

Typical values for neutron stars can be read below (Longair, 2002; P. A. Charles, 1995):

$$\boxed{\begin{aligned} &M_{\mathrm{ns}} = 1 - 2\,\mathrm{M}_{\odot}, \\ &R_{\mathrm{ns}} \approx 10^{-5}\,\mathrm{R}_{\odot} \approx 10 - 15\,\mathrm{km}, \\ &\rho_{\mathrm{ns}} \approx 10^{6} - 10^{15}\,\mathrm{g/cm^3}. \end{aligned}}$$

Neutron stars are one of three possible endpoints of stellar evolution (Longair, 2002). Stars which have an original mass of $1 \leq M \leq 4\,\mathrm{M}_{\odot}$ or a mass of the core of $M_{\mathrm{core}} < 1.4\,\mathrm{M}_{\odot}$ become, after having burned all their fuel, a planetary nebula and later a white dwarf. Neutron stars are formed by stars with an original mass of $4 \leq M \leq 10\,\mathrm{M}_{\odot}$ or $M_{\mathrm{core}} > 1.4\,\mathrm{M}_{\odot}$. In this case, the original star will explode in a supernova and later form a neutron star. If the original star has a mass of $M \geq 10\,\mathrm{M}_{\odot}$ the end of the star will be the presence of a black hole.

But how exactly does the neutron star formation take place?

For such high densities as inside a white dwarf or a neutron star we can't apply classical gas equations but have to use the Heisenberg's uncertainty principle and the Fermi exclusion principle for fermions. The particles cannot occupy the same quantum states, as there is the formation of a degenerate gas. Therefore the mass limit of the compact object is the result of applying the equation of state for degenerate matter (also see Longair, 2002).

In free space the neutron is unstable and will decay within a half life time of $T = 617\,\mathrm{s}$ because the mass of the neutron is around 1.5 MeV larger, in terms of rest mass energy, than the mass of the products of the neutron decay as can be seen in equation 1.1 (Unsöld & Baschek, 1999):

$$n \longrightarrow p^{+} + e^{-} + \overline{\nu}_{\mathrm{e}}, \qquad T = 617\,\mathrm{s}. \tag{1.1}$$

In the degenerate star, above a certain energy of around $E_0 > 0.78\,\mathrm{MeV}$ (Unsöld & Baschek, 1999) it is favorable to have neutrons (see equation 1.2, Unsöld & Baschek, 1999)), also because there is no free space for electrons left due to the compression of the star. The density at which this value of the energy E_0 is reached is at about $\rho \approx 10^7\,\mathrm{g/cm^3}$ (Unsöld & Baschek, 1999), a little bit higher as the critical density for white dwarfs.

$$m_\mathrm{p} + m_\mathrm{e} + E_0 > m_\mathrm{n}, \qquad E_0 > 0.78\,\mathrm{MeV}, \tag{1.2a}$$

$$p^+ + e^- \longrightarrow n + \nu_\mathrm{e}. \tag{1.2b}$$

For increasing energy the star is getting more and more neutron-rich, until at a density of about $\rho \approx 10^7\,\mathrm{g/cm^3}$, almost all matter of the star is converted into neutrons. This marks the birth of the neutron star.

The physics of neutron stars is similar to that of white dwarfs, but neutrons are about 2000 times heavier and therefore the degeneracy sets in at higher densities. The following equations give us the relation between pressure P_ns and density ρ for the non-relativistic (see equation 1.3a) and for the relativistic case (see equation 1.3b, Longair, 2002).

$$P_\mathrm{ns} = \frac{1}{5\mathrm{m_n}}\Big(\frac{3\mathrm{h}^3}{8\pi}\Big)^{2/3}\Big(\frac{\rho}{\mathrm{m_n}}\Big)^{5/3}, \tag{1.3a}$$

$$P_\mathrm{ns} = \frac{\mathrm{c}}{4}\Big(\frac{3\mathrm{h}^3}{8\pi}\Big)^{1/3}\Big(\frac{\rho}{\mathrm{m_n}}\Big)^{4/3}. \tag{1.3b}$$

Now, we can also understand one possible way of formation of a neutron star, namely the neutron stars out of white dwarfs. For a white dwarf there exists a maximum limit of mass, the Chandrasekhar limit (Longair, 2002):

$$M_\mathrm{Ch} \approx 1.46\,\mathrm{M_\odot} \qquad \textit{Chandrasekhar limit} \tag{1.4}$$

If an accreting white dwarf which reaches a mass bigger than the Chandrasekhar limit the electrons in the white dwarf get relativistic. Therefore the equation of state of the electron-contented white dwarf gets weaker, which means that the pressure increases proportional to $P_\mathrm{e} \propto \rho^{4/3}$ instead of $P_\mathrm{e} \propto \rho^{5/3}$ as in the non-relativistic case before (Longair, 2002). Thus, at some point the pressure gets too small and the white dwarf collapses because the star can't sustain the pressure anymore. This

process can only be stopped through neutron degeneration and therefore through the formation of a neutron star.

To obtain the Chandrasekhar limit exactly through calculation, we only have to apply two equations, the hydrostatic equilibrium and the conservation of mass (Longair, 2002):

$$\begin{aligned} \frac{dp}{dr} &= -\frac{\mathrm{G}M\rho}{r^2} \qquad \textit{hydrostatic equilibrium,} \\ \frac{dM}{dr} &= 4\pi r^2 \rho \qquad \textit{conservation of mass.} \end{aligned} \tag{1.5}$$

In our case the pressure should only depend on the density as it is the case for a polytrop $p = \kappa\rho^{\gamma}$ with polytropic index $\gamma = 1 + \frac{1}{n}$:

$$\begin{aligned} &\rho\,(r) = \rho_{\mathrm{c}} w^n \\ &\gamma = \frac{5}{3} \quad \text{(non-relat.)} \quad \longrightarrow \quad n = \frac{3}{2}, \\ &\gamma = \frac{4}{3} \quad \text{(relat.)} \qquad \longrightarrow \quad n = 3. \end{aligned} \tag{1.6}$$

What we get by reorganizing the equations and by the use of dimensionless variables and a little bit analysis is the famous Lane-Emden equation:

$$\left.\begin{aligned} &\frac{d}{dr}\Big(\frac{r^2}{\rho}\frac{dp}{dr}\Big) + 4\pi\mathrm{G}\rho r^2 = 0 \\ &\text{with } r = az,\ a = \Big[\frac{(n+1)\,\kappa\rho_{\mathrm{c}}^{(1/n)-1}}{4\pi\mathrm{G}}\Big]^{1/2} \end{aligned}\right\} \quad \begin{aligned} &\frac{1}{z^2}\Big[\frac{d}{dz}\Big(z^2\frac{dw}{dz}\Big)\Big] + w^n = 0 \\ &\textit{Lane-Emden equation} \end{aligned} \tag{1.7}$$

Now, we have to look for those values of z for which w goes to zero to get a relation for the central density ρ_{c} and the corresponding radius R. The surface of the star corresponds to $R = az_{\mathrm{n}}$, the value for which the density goes to zero. What we get is:

$$\rho_{\mathrm{c}} \propto R^{2n(1-n)} \tag{1.8}$$

By integrating the density and using the Lane-Emden equation we can obtain the mass of the star:

$$M \propto \rho_{\mathrm{c}} R^3 \propto R^{(3-n)/(1-n)} \tag{1.9}$$

If we take for example $n = \frac{3}{2}$, we get a mass which is related to the radius as $M \propto R^{-3}$. The radius of the star is decreasing with increasing mass, while the central density is increasing with the mass until at some point the critical density is reached and we have to apply the relativistic equations (n=3). For n=3 the mass gets independent of the radius and calculations of the mass (with $\mu_e = 2$) give us a value of $M_{\mathrm{Ch}} = 1.46\,\mathrm{M}_\odot$ which is the maximum mass of a white dwarf.
By doing the same calculations for a neutron star and applying the laws of general relativity, one can obtain the upper mass limit of a neutron star at about $M \approx 3\,\mathrm{M}_\odot$.

1.1.3 Structure of a neutron star

To this day, one unsolved problem is the structure and the equation of state of a neutron star. We know the composition for the outer parts quite well, but for the inner parts it is still unconstrained, also because we cannot rebuild the high density core in a laboratory and conclude from such an experiment.

In figure 1.1 on page 5 you may see the rough structure of a neutron star.

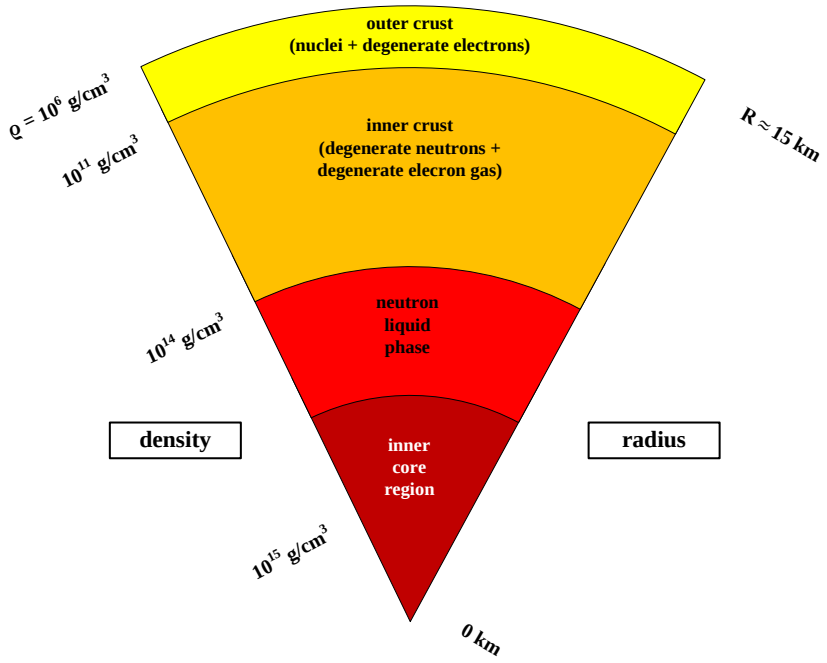

Figure 1.1: Structure of a neutron star

In accordance with Longair (Longair, 2002), the atmosphere of a neutron star consists of a plasma of H, He, C, Fe as well as other elements and has a density

of about up to $\rho < 10^6\,\mathrm{g/cm^3}$. The outer crust is mainly formed out of a degenerate electron gas and also consists of nuclei, as for example ^{62}Ni, which is produced by inverse β-decay and has got a density of the order of $\rho \approx 10^6 - 10^{11}\,\mathrm{g/cm^3}$. Going further inside the neutron star we have the inner crust with a density of $\rho \approx 10^{11} - 10^{14}\,\mathrm{g/cm^3}$, mainly made up of free degenerate neutrons and a degenerate electron gas. Reaching higher densities there is the neutron liquid phase, in which we already reach values up to $\rho \approx 10^{14}\,\mathrm{g/cm^3}$. The neutron liquid phase mainly consists of suprafluid neutrons and some superconducting electrons. At the end there remains the inner core region. There are different ideas about how the dense inner core may look like. Probably there is a Bose-Einstein Condensate or hadronic matter or probably there are quarks, but it's still undetermined, also because we still don't know the nuclear reactions going on inside a neutron star. The same applies for the equation of state which is still unknown because all models depend on assumptions about the inner core. But what we know is that the density for the inner core region reaches extremely high values up to $\rho = 10^{15}\,\mathrm{g/cm^3}$.

1.1.4 Properties of neutron stars

Neutron stars are very fast rotators. If we look at the conservation of angular momentum and assume typical values for the mass and the radius of a neutron star of the order of $1\,\mathrm{M_\odot}$ and 10 km and compare it to our sun, we get a rotational period of about $P_\mathrm{ns} = 0.001\,\mathrm{s}$ (see equation 1.10, Unsöld & Baschek, 1999).

$$\left.\begin{array}{lcl} I_\mathrm{i}\omega_\mathrm{i} = I_\mathrm{f}\omega_\mathrm{f} & \longrightarrow & \dfrac{2}{5}M_\mathrm{i}R_\mathrm{i}^2\omega_\mathrm{i} = \dfrac{2}{5}M_\mathrm{f}R_\mathrm{f}^2\omega_\mathrm{f} \\ M_\mathrm{f} \approx M_\mathrm{i} & \longrightarrow & \dfrac{\omega_\mathrm{f}}{\omega_\mathrm{i}} \approx \dfrac{R_\mathrm{i}^2}{R_\mathrm{f}^2} \end{array}\right\} \quad P_\mathrm{ns} = 0.001\,\mathrm{s} \tag{1.10}$$

$R_\mathrm{i} = R_\odot = 700 \cdot 10^3\,\mathrm{km}$, $P_\mathrm{i} = P_\odot = 27\,\mathrm{d}$, $R_\mathrm{f} = 10\,\mathrm{km}$

Neutron stars also have got enormous magnetic fields which one may estimate by assuming conservation of magnetic flux. What we get out are magnetic fields of the order of $B_\mathrm{ns} \approx 10^{12} - 10^{13}\,\mathrm{G}$ (see equation 1.11, Unsöld & Baschek, 1999).

$$\left.\begin{array}{l} B_\mathrm{i} \cdot 4\pi R_\mathrm{i}^2 = B_\mathrm{f} \cdot 4\pi R_\mathrm{f}^2 \quad \longrightarrow \quad B_\mathrm{f} = B_\mathrm{i} \cdot \left(\dfrac{R_\mathrm{i}}{R_\mathrm{f}}\right)^2 \\ B_\mathrm{i} = B_\odot = 1\,\mathrm{kG},\ R_\mathrm{i} = 10^6\,\mathrm{km} \end{array}\right\} \quad B_\mathrm{ns} \approx 10^{12} - 10^{13}\,\mathrm{G} \tag{1.11}$$

1.2 Pulsars

In the previous paragraph I gave a schematic overview of the different components and the properties of a neutron star. Spinning neutron stars which have got a displacement of the magnetic axis with respect to the axis of rotation emit radiation along the magnetic field axis in form of a beam. They are called pulsars. Due to the non-aligned axis a distant observer will observe a periodic signal. The emitted radiation can only be seen each time the beam cone crosses the line of sight of the observer which occurs once each period for one pole. What is observed is a periodic signal similar to the periodic light cone from a lighthouse (from Longair, 2002; Unsöld & Baschek, 1999).

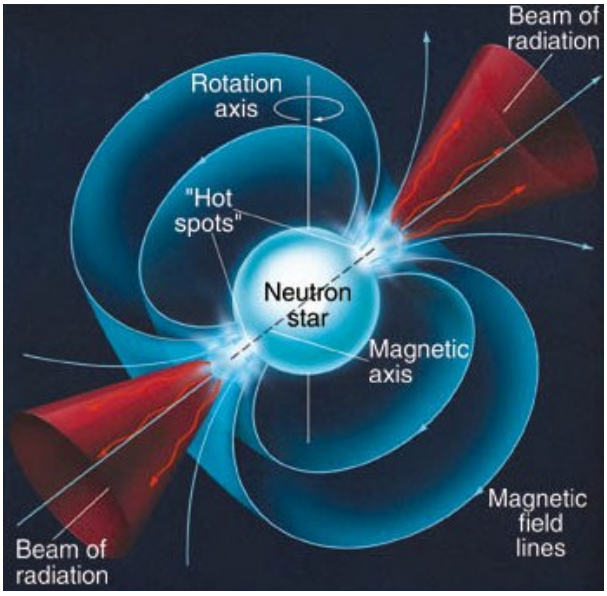

Figure 1.2: Schematic view of a pulsar (*http://lifeng.lamost.org/courses/astrotoday/CHAISSON/AT322/HTML/AT32202.HTM*)

There are two different types of pulsars. The accretion-powered X-ray pulsars in binary systems and the isolated, rotation-powered pulsars or magnetars (e.g. Klochkov, 2007; Lamb et al., 1973; Pringle & Rees, 1972). A schematic view of a pulsar with its two magnetic poles and the magnetic field lines is shown in figure 1.2. Pulsars have got an open and a closed magnetosphere (Longair, 2002). Inside the closed magnetosphere charged particles are trapped and forced to follow the magnetic field lines onto the magnetic poles. The accretion radius is determined by the magnetic pressure which means by the strength of the magnetic field. Particles on open magnetic field lines do escape and therefore won't reach the poles on the neutron star, which means no accretion.

1.3 Isolated neutron stars and magnetars

In the following section I want to give an overview of the group of X-ray pulsars which are powered by rotational energy loss or magnetic field decay. The most acknowledged scenario for the coherent emission of radio pulsars is explained in Longair (2002). Pulsars have got very high potential differences between their magnetic poles and the equator of the order of $10^{16}\,\mathrm{V}$ (for a 1 s pulsar with $B = 10^8\,\mathrm{T}$). Therefore, charged particles can be accelerated up to very high energies, which means energies about 10^6 times bigger than the rest mass of the electron. Due to the fact that charged particles are forced to follow the magnetic field lines there will be production of curvature radiation (synchrotron radiation with a very high radius) which is emitted along the magnetic axis in form of a beam. Afterwards, the so produced photons can interact with high energy electrons via Inverse Compton effect or with other photons and produce $e^+ - e^-$ pairs (Longair, 2002, see equations 1.12). The produced electrons and positrons radiate high energy photons which will again produce photons and $e^+ - e^-$ pairs. This process will go on and on and at the end there will form a cascade of electrons and photons (model originally by Ruderman and Sutherland, 1975).

$$\begin{aligned} e^- + \gamma \quad &\longrightarrow \quad e^- + \gamma', \qquad E_{\gamma'} > E_\gamma, \\ \gamma + \gamma \quad &\longrightarrow \quad e^- + e^+. \end{aligned} \tag{1.12}$$

The change in the rotational energy of a pulsar leads, in turn, to a change in the pulsar's period with the time, which can be described by following equation:

$$\frac{dE}{dt} = \frac{d}{dt}(\frac{1}{2} I\Omega^2) = I\Omega\dot{\Omega} \propto \frac{\dot{P}}{P^3} \tag{1.13}$$

E: rotational energy; I: moment of inertia; Ω: angular velocity.

For the Crab Pulsar the change in the period is around $\dot{P}_{\mathrm{Crab}} = \frac{d}{dt}\left(\frac{1}{\nu}\right) = \frac{\dot{\nu}}{\nu^2} = \frac{3.7 \cdot 10^{-10}}{29.78^2}\frac{\mathrm{s}}{\mathrm{s}} = 4.26 \cdot 10^{-13}\ \frac{\mathrm{s}}{\mathrm{s}}$ which leads to a luminosity or rather energy loss of $-\frac{dE}{dt} \approx 4.4 \cdot 10^{38}\,\frac{\mathrm{erg}}{\mathrm{s}}$ until today (Abbott et al., 2008).

One can describe the change in the period and the inferred loss of rotational energy with the braking torque model. In this model the change in the pulse period is described by a braking index n (see equation 1.14, Longair, 2002). The braking index n may give us important information about the exact way of the slowing down of a pulsar.

$$\dot{\Omega} = -\text{const} \cdot \Omega^n \qquad \Omega\text{: rotational frequency} \tag{1.14}$$

$$n = \frac{\Omega\ddot{\Omega}}{\dot{\Omega}^2} = \frac{P\ddot{P}}{\dot{P}^2} \tag{1.15}$$

Because of the immense magnetic fields of the pulsars the most important actuator of energy loss is magnetic braking. The dipole moment of the neutron star changes all the time due to the non-aligned axis and for this reason there is emission of electromagnetic radiation (see equation 1.16, Longair, 2002). In case of the magnetic dipole radiation the braking index is $n = 3$. By knowing the pulse period and its derivatives quite well, the braking index can be easily calculated (see equation 1.15, Longair, 2002) and we get values such as $n = 2.515 \pm 0.005$ for the Crab (Longair, 2002).

$$-\frac{dE}{dt} = \frac{\mu_0 |\ddot{\mathbf{p}}_\mathrm{m}|^2}{6\pi \mathrm{c}^3} \tag{1.16}$$

$\mathbf{p}_\mathrm{m}$: magnetic dipole moment

In case of magnetic dipole radiation ($\mathbf{p}_\mathrm{m} \propto \mathbf{sin}(\mathbf{\Omega t})$) the infered energy loss is $-\frac{dE}{dt} \propto \Omega^4$ (according to equation 1.16). Comparing this value to the one of equation 1.13 ($\frac{dE}{dt} \propto I\Omega\dot{\Omega}$), we get $\Omega^4 \propto \Omega\dot{\Omega}$ and therefore a braking index of $n = 3$ ($\dot{\Omega} \propto \Omega^3$), as mentioned before.

By assuming that the magnetic braking is responsible for the slowing-down of the neutron star, one can calculate the magnetic field on the surface of a neutron star. Equalizing $\dot{E}_\mathrm{brake} = \dot{E}_\mathrm{rot}$, we get a magnetic field of about $B \approx 2 \cdot 10^6 - 2 \cdot 10^9\,\mathrm{T}$ respectively for millisecond pulsars smaller (see equation 1.17, Longair, 2002).

$$B_\mathrm{s} = \left(\frac{3\mu_0 \mathrm{c}^3 M}{80\pi^3 R^4}\right)^{1/2} \left(P\dot{P}\right)^{1/2} \approx 3 \cdot 10^{15} \left(P\dot{P}\right)^{1/2}\ \mathrm{T} \tag{1.17}$$

Knowing the pulse period and the changes in the pulse period, one can also estimate the age of the pulsar. To do so one has to assume a constant braking index n over the whole lifetime of a neutron star. By integrating equation 1.14 and assuming a braking index of $n > 1$ and an initial angular frequency $\Omega_0 \gg \Omega$ one gets a lifetime of (see equation 1.18, Longair, 2002):

$$\tau = \frac{\Omega^{-(n-1)}}{\text{const} \cdot (n-1)} = \frac{-\Omega}{(n-1)\,\dot{P}} = \frac{P}{(n-1)\,\dot{P}} \tag{1.18}$$

By using a conventional value for the braking index of about $n = 3$ one can plot the time derivative of the pulse period $\dot{P}$ over the period P, as shown in figure 1.3, to get a better view of the way of life of a pulsar. In the $P - \dot{P}$ - diagram we can see that the magnetic braking explains the measured distribution of the ages of pulsars (Longair, 2002).

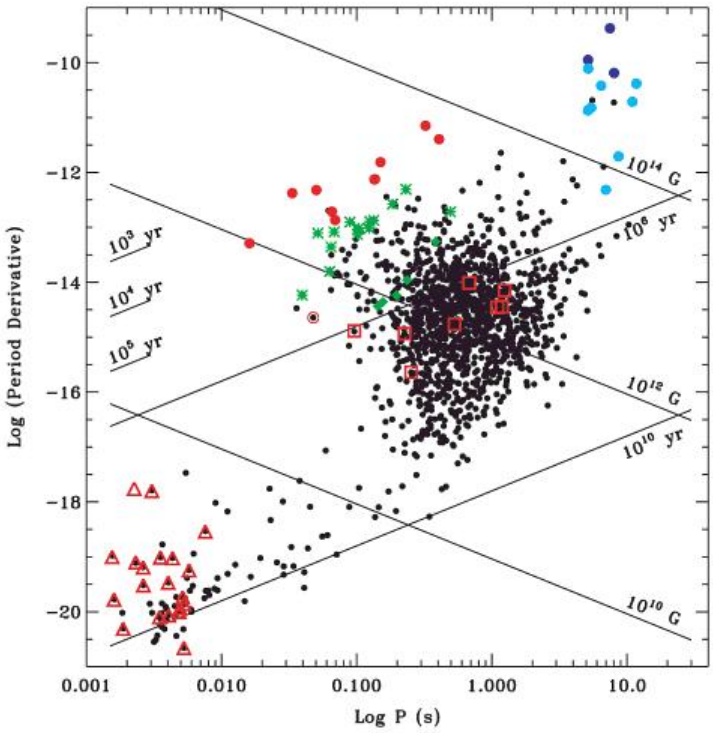

Figure 1.3: Period evolution of rotation-powered pulsars (*small black dots*). Straight lines are constant ages and constant magnetic field strength. *dark blue* - soft gamma repeaters, *light blue* - anomalous X-ray pulsars, *red filled circles* - Crab-like pulsars, *green stars* - Vela-like pulsars, *green diamonds* - X-ray detected cooling stars and *red squares* - million years old pulsars. From Trümper & Hasinger (2008).

As shown in figure 1.3, there are two groups of pulsars. The main group consists of pulsars with a period of about a second while there is also a smaller group of the so called millisecond pulsars. One idea of the formation of those millisecond pulsars and the associated spin-up process is the accretion in a binary system.

Another class of pulsars are the magnetars. Magnetars are pulsars with ultra strong magnetic fields of the order of $B \approx 10^{14}-10^{15}$ G. Magnetars have got very short pulse periods of about 1 ms but quickly lose most of their rotational energy by magnetic braking (Duncan & Thompson, 1992). They are difficult to detect because they lose

all their energy relatively fast. Magnetars are unlikely to stay bound in binaries or in the galaxy. They may be observed in connection with gamma-ray bursts which are powered by the energy loss of the magnetar. A subclass of the magnetars are the soft gamma repeaters (SGRs), which emit short bursts with a soft spectrum (Duncan & Thompson, 1992), as well as the anomalous X-ray pulsars (AXPs) (Mereghetti, 2001). The AXPs have got periods of some seconds and no detected connection to a companion (Mereghetti, 2001).

1.4 Accreting X-ray pulsars

Accretion is the general and most effective mechanism for production of high energy radiation in the universe. Its main process is the transformation of gravitational energy into radiation. The energy release ΔE by accreting matter m from infinite distance onto the surface of the star at radius R can be easily calculated by just using the gravitational potential of the star, see equation 1.19 (Unsöld & Baschek, 1999).

$$\Delta E = \frac{\mathrm{G}mM}{R} \tag{1.19}$$

The most effective process is the accretion onto a compact object, for example onto a white dwarf, a neutron star or a black hole. Systems that consist of a compact object and a companion star and therefore emit X-rays are called X-ray binaries. Below we will focus on the accretion onto a neutron star.

Matter falling onto a neutron star from infinity to the radius R of the star has got a kinetic energy of $\frac{1}{2}m_\mathrm{p}v^2 = \frac{\mathrm{G}Mm_\mathrm{p}}{R}$. Here, we just consider protons because the gravitational energy on a proton is about a factor of 2000 higher than on an electron due to their mass. By reaching the surface of the star the particles are decelerated and the kinetic energy is radiated away (Longair, 2002). The rate of this energy dissipation can be calculated and gives us the luminosity of the accretion process:

$$L = \frac{1}{2}\dot{m}v^2 = \eta\Big(\frac{\mathrm{G}M_\mathrm{ns}\dot{m}}{R_\mathrm{ns}}\Big) = \frac{1}{2}\dot{m}\mathrm{c}^2\frac{r_\mathrm{S}}{R_\mathrm{ns}} = \eta\dot{m}c^2 \tag{1.20}$$

$\dot{m}$: mass accretion rate; M_ns: mass of neutron star; R_ns: radius of neutron star; $r_\mathrm{S} = \frac{2\mathrm{G}M}{\mathrm{c}^2}$: Schwarzschild radius; $\eta = \frac{1}{2}\Big(\frac{r_\mathrm{S}}{R}\Big)$: energy conversion coefficient.

Using typical values we obtain:

$$L_\mathrm{acc} \approx 10^{37}\Big(\frac{\dot{m}}{10^{17}\,\mathrm{g/s}}\Big)\Big(\frac{M_\mathrm{ns}}{\mathrm{M}_\odot}\Big)\Big(\frac{R_\mathrm{ns}}{10\,\mathrm{km}}\Big)^{-1}\,\mathrm{erg/s} \approx 10^{37}\,\mathrm{erg/s} \tag{1.21}$$

The energy conversion coefficient η is used to express the luminosity as a function of rest mass energy converted to heat and radiation which can be released. For a neutron star the energy is converted into X-rays on the surface of the star. The conversion coefficient is typically $\eta \approx 0.1$. Accretion is a much more powerful process than nuclear energy production, as for example in the p-p chain ($\eta = 7 \cdot 10^{-3}$, Longair, 2002). You may compare the value for η of a neutron star to those of a white dwarf or a black hole. For a white dwarf with one solar mass and a radius of $r = 5 \cdot 10^6\,\mathrm{m}$ the conversion coefficient η is around $\eta \approx 3 \cdot 10^{-4}$, thus much smaller than the one for a neutron star. Looking at black holes we have $\eta \approx 0.06$ for a Schwarzschild black hole (non-rotating) and $\eta \approx 0.426$ for a Kerr black hole (rotating) for the accretion of matter to the last stable orbit (Longair, 2002).

There are different types of accretion which will be explained in the following, namely accretion through Roche Lobe overflow in Low Mass X-ray Binaries and accretion through stellar winds in High Mass X-ray Binaries (Trümper & Hasinger, 2008). Which kind of accretion we have depends, as the name already says, upon the mass of the companion star. The mass of the stars in a binary can be measured directly by observing the orbital motion of the system.

1.4.1 Low Mass X-ray binaries

For Low Mass X-ray binaries the companion of the neutron star has got a mass smaller than two solar masses and a spectral type of class A or later (Trümper & Hasinger, 2008). The orbital period is of the order of hours to days. The accretion process is taking place through Roche Lobe overflow over the inner Lagrangian point as can be seen in figures 1.4 and 1.5.

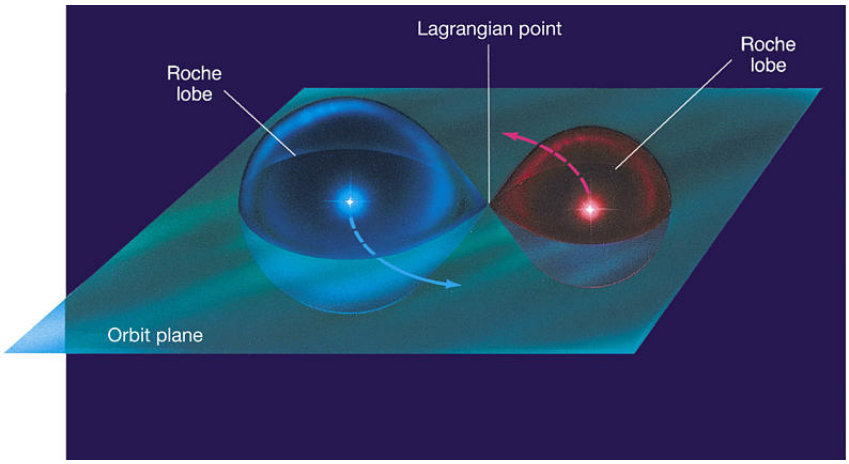

Figure 1.4: Roche Lobe of a binary system (*http://physics.uoregon.edu/~jimbrau/BrauImNew/Chap20/FG20_21.jpg*)

The different lines in the figure above represent the equipotential surfaces of the rotating binary system and are shown in form of an equation in 1.22 (Longair, 2002). There are two gravitation potential terms, one for each star, and one term characterizing the centrifugal potential of the binary motion, which we take as the reference frame.

$$\phi = \frac{GM_1}{r_1} + \frac{GM_2}{r_2} - \Omega^2 r^2 = \text{const.} \tag{1.22}$$

r: distance to centre of mass; $r_1(r_2)$: distance to centre of star with $M_1(M_2)$

There is one equipotential line which connects both stars, the Roche Lobe. Accretion takes place through the inner Lagrangian point that connects both Roche Lobes, because matter always aims for the smallest gravitational potential. At this point there is no net force on a particle (Longair, 2002).The equipotential lines with the various Lagrangian points, the inner Lagrangian L_1 and the outer Lagrangians, as well as the Roche Lobe is also shown in figure 1.5.

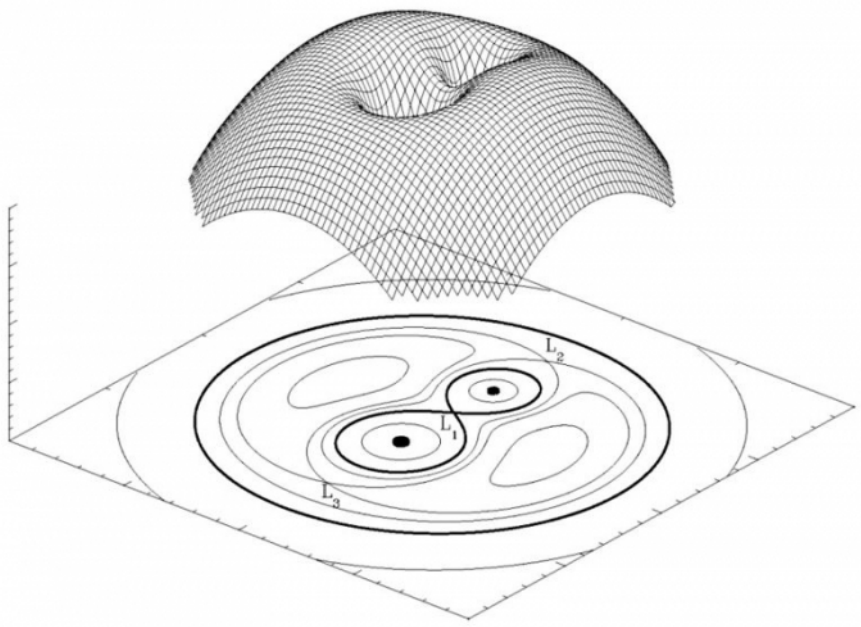

Figure 1.5: Equipotential lines and Roche Lobe (in bold) of a binary system with the according Lagrangian points (*https://www.e-education.psu.edu/astro801/content/l6_p6.html*)

In the Low Mass X-ray binary systems there will be the formation of an accretion disk because of the conservation of angular momentum (Longair, 2002). The material has to get rid of its angular momentum before it is able to be accreted. While the neutron star accretes matter the gravitational energy decreases and while the material is falling inwards it also loses angular momentum, so that it is possible that the material is falling deeper into the gravity of the compact object. This loss of angular momentum is compensated by the gain of angular momentum of the outer parts of the disk, the angular momentum is transported outwards by viscosity (Longair, 2002). Considering the Virial Theorem ($-\frac{1}{2}U(r) = E_{\mathrm{k}}$), half of the initial gravitational energy is radiated away in the disk due to friction and the other half goes into kinetic energy of the particles (Unsöld & Baschek, 1999).

1.4.2 High Mass X-ray binaries

The optical counterpart of a High Mass X-ray binary is a Be star with a mass of $M \geq 5\,\mathrm{M}_{\odot}$ or an OB supergiant ($M \geq 15\,\mathrm{M}_{\odot}$) (Trümper & Hasinger, 2008). Those systems have got long orbital periods of the order of days to tens of days and because most companions don't fill their Roche Lobe the mass transfer occurs mainly through accretion of stellar wind (but also Roche Lobe overflow possible) (Trümper & Hasinger, 2008).

So, how much material will be accreted in a High Mass X-ray binary?

The wind material will be only captured if it passes within a certain radius, the accretion radius r_{acc} (see equation 1.23, P. A. Charles, 1995). Assuming typical values of wind velocity ($v_{\mathrm{wind}} \approx 10^3\,\mathrm{km/s}$, I. Caballero, 2009) and mass of the accretor we get an accretion radius of $r_{\mathrm{acc}} = 10^{10}\,\mathrm{cm}$ (I. Caballero, 2009) and a mass accretion rate of about $\dot{M} \approx 10^{-4}\ \dot{M}_{\mathrm{wind}} \approx 10^{-6}\,\mathrm{M}_{\odot}/\mathrm{yr}$ (P. A. Charles, 1995).

$$\begin{aligned} & U(r) + E_{\mathrm{k}} < 0 \\ & -\frac{\mathrm{G}M}{r} + \frac{v_{\mathrm{rel}}^2}{2} < 0 \\ \longrightarrow \quad & r < r_{\mathrm{acc}} = \frac{2\mathrm{G}M}{v_{\mathrm{rel}}^2} \end{aligned} \tag{1.23}$$

v_{rel}: $v_{\mathrm{rel}}^2 = v_{\mathrm{wind}}^2 + v_{\mathrm{ns}}^2 \approx v_{\mathrm{wind}}^2$ relative velocity of accretor with respect to wind

Wind accretion is much less effective than accretion by Roche Lobe overflow because only a very small fraction of the matter, ejected by the wind, is accreted onto the neutron star.

$$\dot{M} \approx \frac{\pi r_{\mathrm{acc}}^2}{\Omega a^2} \dot{M}_{\mathrm{wind}} \approx 10^{-4}\, \dot{\mathrm{M}}_{\mathrm{wind}} \tag{1.24}$$

$v_{\mathrm{wind}} \approx 10^3\,\mathrm{km/s}$; $a \approx 10^{12}\,\mathrm{cm}$: orbit radius; $\Omega \approx 4\pi$: isotropic wind emission angle for B stars (I. Caballero, 2009).

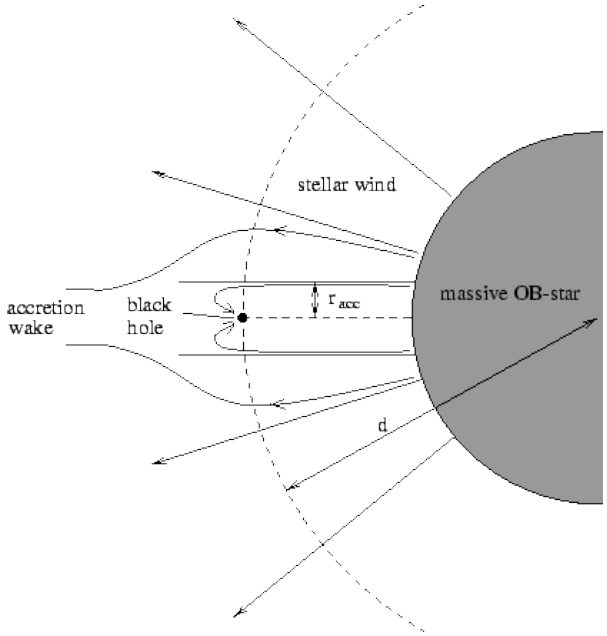

Figure 1.6: Accretion through stellar wind (*http://ttt.astro.su.se/groups/head/ /sara/img44.gif*)

1.4.3 Be systems

There is another subgroup of High Mass X-ray binaries, the Be/X-ray binary systems, which are the most common type of binaries (about 60 % of all HMXBs (114 HMXBs are listed in the 4th edition of the *Catalogue of high-mass X-ray binaries in the Galaxy*) are Be systems according to Liu et al. (Liu et al., 2006). Most X-ray sources in binary systems with Be stars are transients demonstrating outbursting activity, connected with the evolution of a normal star. Be stars are stars of the spectral class B (**B**e) that show emission lines (B**e**) and have formed a disk around its equator, which was probably built due to the star's fast rotational speed. They are rotating very fast with a dense, but radially slow, stellar wind which forms an equatorial disk around the star (Negueruela, 1998; Okazaki & Negueruela, 2001; Tsygankov et al., 2006).

If now, a compact object is orbiting around the Be star and traversing through the Be star's ring or atmosphere there will be an increase of the X-ray output of the compact object (Hanuschik, 1996; Quirrenbach et al., 1997). This happens if the centrifugal barrier allows accretion onto the compact object. For an eccentric orbit one observes an X-ray activity which is modulated with the orbital period of the compact object around the companion star (P. A. Charles, 1995). This type of X-ray outburst lasts from days to weeks and reaches luminosities of $L_{\mathrm{x}} \approx 10^{36} - 10^{37}\,\mathrm{erg/s}$. They are named (Normal) Type I outbursts (classification according to Stella et al., 1986). But there are also bursts which are not related to any orbital behavior and reach much higher luminosities ($L > 10^{37}\,\mathrm{erg/s}$). We call them Type II outbursts or Giant outbursts. They normally last for over a few weeks and are triggered by an increase of the activity of the Be companion star, which leads to a blowing up of the stars envelope. For this reason the neutron star may form a disk around itself. At least, the Be systems can also be quiet, which means that they have a luminosity of $L < 10^{36}\,\mathrm{erg/s}$ (Coe, 2000; I. Caballero, 2009; Ziolkowski, 2002).

1.5 Mechanisms of accretion

The Eddington luminosity L_{edd} is the maximal value of luminosity up to which accretion is still possible. One can calculate L_{edd} by just equating outwards and inwards forces which means radiation force F_{rad} and gravity F_{grav} (see equation 1.25, P. A. Charles, 1995).

$$\left.\begin{aligned} F_{\mathrm{rad}} &= \sigma_T \frac{L}{4\pi r^2 \mathrm{c}} \\ F_{\mathrm{grav}} &= \frac{\mathrm{G}M m_{\mathrm{p}}}{r^2} \end{aligned}\right\} \quad \begin{aligned} L_{\mathrm{edd}} &= \frac{4\pi \mathrm{G} m_{\mathrm{p}} \mathrm{c}}{\sigma_{\mathrm{T}}} M_\odot = 1.3 \cdot 10^{38} \Big(\frac{M}{M_\odot}\Big)\ \mathrm{erg/s} \\ &\textit{Eddington luminosity} \end{aligned} \tag{1.25}$$

$\sigma_{\mathrm{T}} = 6.65 \cdot 10^{-25}\,\mathrm{cm}^2$: Thomson cross-section

If the radiation pressure is getting bigger than gravity the matter can't be accreted anymore and is pressed outwards. This process is cutting-off the energy supply and the luminosity is decreasing. At some point, the luminosity is so small that accretion can take place again until it hits L_{edd} again (Trümper & Hasinger, 2008).

Gravity dominates the regions far away from the neutron star while it can be neglected for distances smaller than the Alfvén radius (or magnetospheric radius). In this region magnetospheric effects dominate the accretion process. The Alfvén radius marks the distance at which the effects of magnetic pressure and gravity are equal (Ghosh & Lamb, 1979b; Klochkov, 2007; Lamb et al., 1973). For typical

neutron star parameters the Alfvén radius has got values of about $10^2 - 10^3$ km (Lamb et al., 1973).

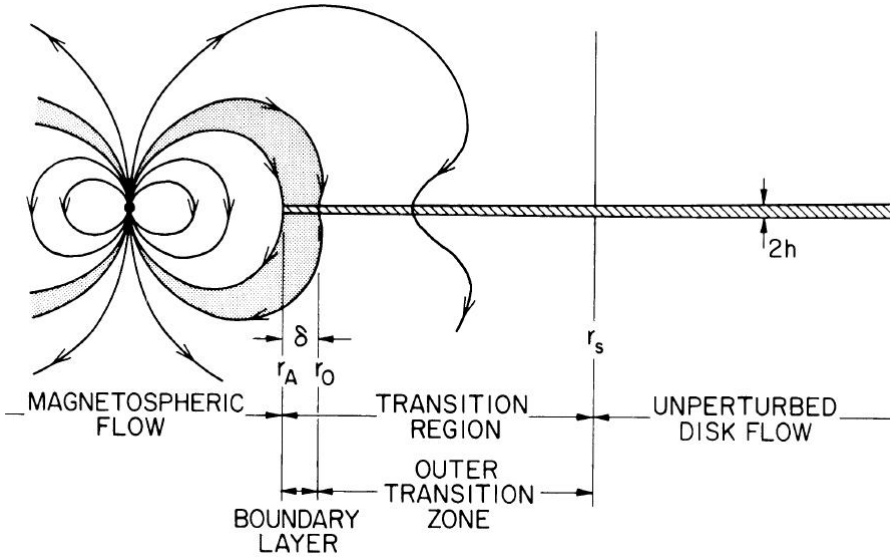

Figure 1.7: Schematic view of an accreting X-ray pulsar. Marked is the corotation radius (r_O), the Alfvén radius (r_A) as well as the boundary layer and the different transition regions and the region of unperturbed disk flow (Ghosh & Lamb, 1978).

As shown in figure 1.7, there are different regions of an accreting X-ray pulsar. Above r_S the disk flow is unperturbed by the magnetosphere and the matter is predominantly effected by gravity. This changes when the particles get closer to the neutron star. In the transition zone there occurs a change from a gravity dominated flow to a magnetic dominated accretion. It splits in two parts, an outer and an inner transition zone. In the outer transition zone, viscosity effects dominate the accretion while reaching the boundary layer, magnetospheric stresses are predominantly (Ghosh & Lamb, 1978). At the Alfvén radius, which is determined by the star's magnetic field and the resulting magnetic pressure, the accretion disk is interrupted because the pressure of the magnetic field destroys the disk and the particles are funneled along the field lines onto the magnetic poles (Basko & Sunyaev, 1976). The corotation radius marks the distance where the Keplerian disk velocity is equal to the angular velocity of the magnetosphere (Ghosh & Lamb, 1978; Klochkov, 2007).

1.5.1 Accretion torques

The spin period evolution of an accreting pulsar can be described with the torque theory. The acreting pulsar can spin-up if the accreted matter has an angular momentum. The magnetic coupling between the star and the plasma is noticeable. Therefore the spin-up torque on fast rotators is less than that on slower rotators (Ghosh & Lamb, 1979b). For accretion from a disk, the disk exerts a torque on the neutron star and causes the spin-up of the star as in Ghosh & Lamb (1979b); I. Caballero (2009):

$$-\dot{P} = 5.0 \cdot 10^{-5} \mu_{30}^{2/7} n(\omega_S) S_1(M) (P L_{37}^{3/7})^2 s/yr \tag{1.26}$$

μ_{30}: magnetic moment in $10^{30} gcm^3$, ω_S: fastness parameter or dimensionless stellar angular velocity, $n(\omega_S)$: dimensionless torque, $S_1(M)$: structure function and L_{37}: luminosity in 10^{37} erg/s.

According to Bildsten et al. (1997); Pringle & Rees (1972) the spin-up torque exerted from the accretion disk on the neutron star is

$$N \approx \dot{m} \sqrt{G m r_m} \tag{1.27}$$

r_m: magnetospheric radius.

By taking into account that the luminosity L_x is proportional to the mass accretion rate $\dot{m}$ (see equation 1.20) and that $N = \frac{dI\omega}{dt}$ (with I: moment of inertia, ω: angular frequency), the change in the period can be calculated using torque theory (Ghosh & Lamb, 1979b; Schönherr, 2007). We get approximately a behaviour of the pulse period as

$$-\frac{\dot{P}}{P} \propto L^{6/7}. \tag{1.28}$$

A more detailed description should also take into account the slow-down processes of a neutron star due to spin-down torques. Those torques result from an interaction at distances beyond the corotation radius of the magnetic field lines with the accretion disk (Schönherr, 2007). For more information about the torque theory have a look at e.g. Ghosh & Lamb (1979b); Pringle & Rees (1972).

1.5.2 Accretion column

As was explained in the paragraph before, there are two different mechanisms of accretion: accretion through Roche Lobe overflow and accretion by stellar winds.

Regardless of the distant mechanism, inside the Alfvén radius the accretion is dominated by magnetospheric effects. The accreted matter is forced to follow the magnetic field lines onto the magnetic poles of the neutron star generating an accretion column. Going down onto the magnetic poles a free-fall flow is generated which can reach free-fall velocities of about 0.5 c. A small region of about 1 km^2 which is characterized by high temperatures arises. We call this region hot spot. Depending on the accretion rate we will have a different scenario (see e.g. figure 1.8) and a different shape of the accretion column (Basko & Sunyaev, 1976; I. Caballero, 2009; Meszaros, 1984b; Riffert & Meszaros, 1988).

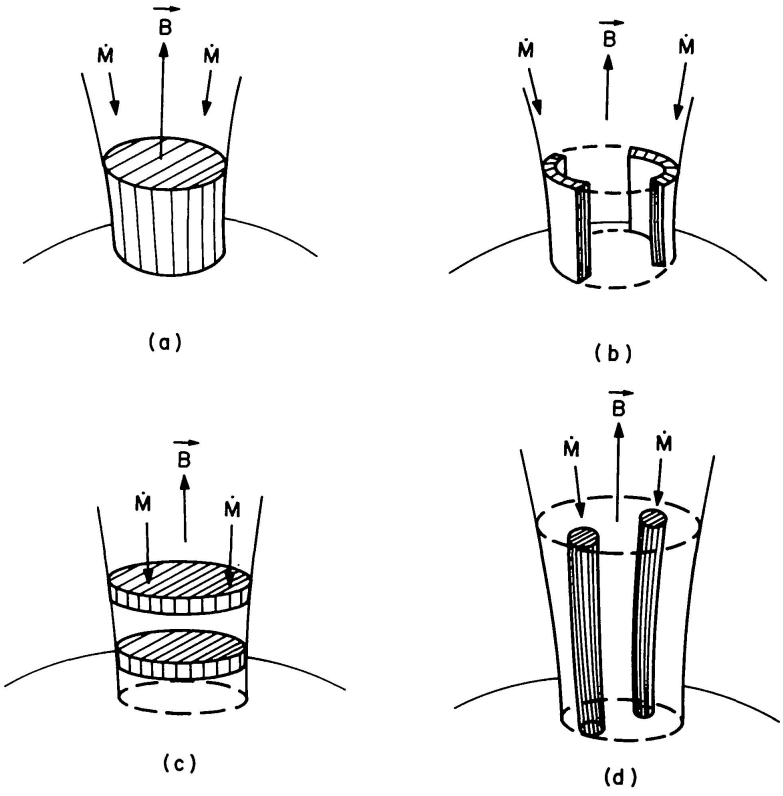

Figure 1.8: Possible accretion scenarios: (a) *filled funnel* (b) *hollow sectional funnel* (c) *pancakes* (d) *spaghettis*. From Meszaros (1984a).

For high accretion rates and luminosities $L > L_{\mathrm{edd}}$ we will have the formation of a shock. The radiation pressure is much bigger than the pressure of the gas. The plasma is going down onto the magnetic poles of the neutron star and will be decelerated and heated. While the plasma is falling down onto the surface of the star the thereby emitted photons can only escape perpendicularly. What we observe is

basically a black body of the shock front, a radiation-dominated shock high above the neutron star surface. The resulting beam from the side of the column looks like a fan and is therefore called fan beam. For lower accretion rates which means luminosities smaller than the Eddington luminosity ($L < L_{\mathrm{edd}}$) there is no shock formation. The free-fall zone of the matter extends almost down to the neutron star's surface. The plasma is decelerated by emission of bremsstrahlung and by Compton Cooling, the radiation can escape along the accretion column and the resulting beam is called pencil beam (Basko & Sunyaev, 1976; Meszaros, 1984b; Riffert & Meszaros, 1988; Tsygankov et al., 2006).

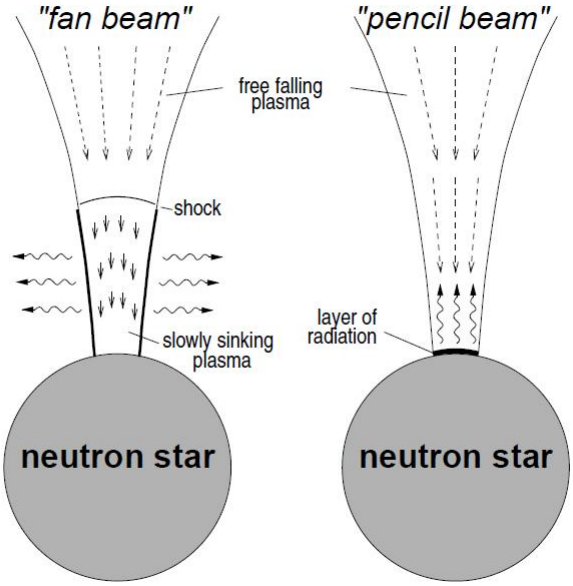

Figure 1.9: Mechanism of fan- and pencil-beam emission (Kretschmar, 2006)

The height of the shock can also be calculated. It changes nearly linearly with the source luminosity and is related to the mass accretion rate $\dot{m}$ as (Tsygankov et al., 2006):

$$h \approx \dot{m} R_{\mathrm{ns}} ln\Big(\eta \frac{1+\dot{m}}{\dot{m}^{5/4}}\Big) \tag{1.29}$$

$\dot{m}$ in 10^{39} erg/s,
η function of magnetic field of neutron star and thickness of accretion column.

Chapter 2

RXTE

The Rossi X-ray Timing Explorer (RXTE) is a spacecraft observing, as the name already says, in the X-ray regime. A huge amount of information about this project can be found on the web, but we will concentrate on the official pages of the NASA HEASARC (*http://heasarc.gsfc.nasa.gov/docs/xte/XTE.html* and *http://heasarc.nasa.gov/docs/xte/learning_center*). The satellite was designed for the sensitive observation of fast-moving and high-energetic objects as there are for example neutron stars, pulsars, black holes, X-ray binaries consisting of those compact objects and X-ray bursts in general. By making measurements in the range of milliseconds to years, one might obtain new knowledge about the behavior and the structure and processes inside those sources. RXTE was launched by a Delta II rocket from Kennedy Space Center at the end of December 1995 and still performs in these days. The spacecraft now circulates at a low Earth orbit of 580 km with an inclination of 23 degrees, and therefore circulates the earth once every 90 minutes.

RXTE consists of three instruments plus a data processing system. The two pointed instruments, the Proportional Counter Array (PCA) and the High Energy X-ray Timing Explorer (HEXTE), cover the energy ranges of 2-60 keV and 15-250 keV, respectively. In addition, there is an All-Sky Monitor (ASM) on board of the satellite, which scans nearly the whole sky (about 80 %) in each orbit. For data processing of the PCA instrument and the ASM there is the Experiment Data System (EDS). For an artistic view of the RXTE satellite see also figure 2.1.

2.1 Proportional Counter Array (PCA)

The PCA instrument on board of RXTE is, as it is HEXTE, a pointed instrument designed for the lower X-ray energies, ranging from about 2-60 keV. It consists of five co aligned proportional modules filled with Xenon gas, which form a total collecting area of 6500 cm^2. Each module is referred to as a Proportional Counter Unit (PCU),

Figure 2.1: Rossi X-ray Timing Explorer (RXTE) (*http://heasarc.gsfc.nasa.gov/docs/xte/learning_center/gifs/discover/xte.jpg*)

numbered from 0 to 4 (*http://heasarc.nasa.gov/docs/xte/abc/contents.html*). The technical properties of the PCA are shown in table 2.1.

Energy range	2-60 keV
Energy resolution	$<$ 18 % at 6 keV
Time resolution	1 microsec
Spatial resolution	collimator with 1 degree FWHM
Detectors	5 proportional counters
Collecting area	6500 cm^2
Layers	1 Propane veto; 3 Xenon; 1 Xenon veto layer
Sensitivity	0.1 mCrab
Background	2 mCrab

Table 2.1: PCA properties (*http://heasarc.gsfc.nasa.gov/docs/xte/XTE.html*)

2.2 High Energy X-ray Timing Explorer (HEXTE)

The main properties of HEXTE are listed in table 2.2. HEXTE is built for higher energies than the PCA and extends the X-ray range of the satellite up to 250 keV. Those energies are measured by two clusters of respectively four phoswich scintillation detectors of which each cluster can be oriented in opponent directions and thus offer background measurements about a few degrees away from the source. HEXTE data are not processed by the EDS but has its own data processing system.

Energy range	15-250 keV
Energy resolution	$<$ 15 % at 60 keV
Time resolution	8 microsec
Spatial resolution	collimator with 1 degree FWHM
Detectors	2 clusters of 4 NaI/CsI scintillation counters
Collecting area	2 x 800 cm^2
Sensitivity	1 Crab = 360 counts/s per HEXTE cluster
Background	50 counts/s per HEXTE cluster

Table 2.2: HEXTE properties (*http://heasarc.gsfc.nasa.gov/docs/xte/XTE.html*)

2.3 All-Sky Monitor (ASM)

The All-Sky Monitor images, as the name already says, the whole sky. During each 90 min orbit around the earth, about 80 % of the whole sky are covered by a total collecting area of 90 cm^2 of the three wide-angle shadow cameras. Its main purpose is to measure the long-time behavior of X-ray sources.

Energy range	2-10 keV
Time resolution	80 % of the sky every 90 min
Spatial resolution	$3'$ x $15'$
Number of shadow cameras	3, each with 6 x 90 degrees FOV
Detector	Xenon proportional counter, position-sensitive
Collecting area	90 cm^2
Sensitivity	30 mCrab

Table 2.3: ASM properties (*http://heasarc.gsfc.nasa.gov/docs/xte/XTE.html*)

2.4 Experiment Data System (EDS)

The EDS processes data from the ASM and the PCA. It has got eight Event Analyzers (EA) in total, six for the PCA and the other two for the ASM, which can work independently in different modes. For us the most important modes are the Event mode, which uses one or two EAs, and the Binned mode, in which there is a time and/or energy binning. This system can process up to 500 000 counts/s and the arrival time of X-rays can be measured with an accuracy of about 1 microsecond (*http://heasarc.gsfc.nasa.gov/docs/xte/XTE.html*).

Chapter 3

V0332+53

3.1 Introduction

The Be-/High Mass X-ray binary V0332+53 was discovered in 1973 by the Vela satellite Vela 5b (Zhang et al., 2005). The source was detected during a type II outburst (Zhang et al., 2005) which lasted for a time of about 3 months (Tsygankov et al., 2006) and reached a peak intensity of 1.6 Crab (Zhang et al., 2005). Type II outbursts are, in contrast to type I outbursts, not related to any orbital behavior and show irregular transient activity (Coe, 2000; Ziolkowski, 2002). At that time the pulse period could already be determined to a value of 4.37 s, while an orbital period of 34 days (Zhang et al., 2005) was measured. Ten years later, there was a second outburst, this time of type I, detected with the Tenma satellite(Zhang et al., 2005). Type I outbursts show periodic transient activities with occurrence times close to periastron passage, which means a modulation with the orbital period of the binary system (Zhang et al., 2005). The source became again active in 1989 in form of a type II outburst (Zhang et al., 2005) until the next huge outburst of type II was measured at the end of 2004 (December 2004 to February 2005) (Mowlavi et al., 2006).

In this last-mentioned outburst, the source intensity was increasing nearly linearly for about 30 days, then stayed near the maximum flux for another 10 days, until the intensity decreased again over the next 50 days (Tsygankov et al., 2006) (see also figure 3.1). The decline phase can be split up in two parts: an exponential decay for about 20-30 days (20 days for energies <20 keV and 30 days for energies above 20 keV (Mowlavi et al., 2006)), and a following linear decrease (Mowlavi et al., 2006). From those two decay time scales one can infer, according to Mowlavi et al. (Mowlavi et al., 2006), that there are two regions that contribute to the X-ray continuum: A hard component which could come out from the accretion column near the resonant scattering region and a softer component from a region higher up in the accretion

column. For this type II outburst (Tsygankov et al., 2006), INTEGRAL measured a peak intensity at the 22nd of December of about 1.2 Crab in the 1.5-12 keV band and 2.2 Crab in the 5-12 keV band (Zhang et al., 2005). The average flux reached values of 550 mCrab for 20-60 keV, respectively 700 mCrab in the higher 3-10 keV range (Kreykenbohm et al., 2005).

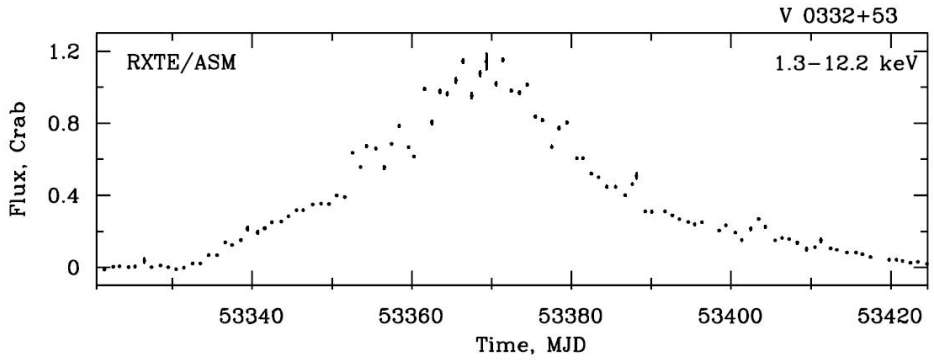

Figure 3.1: Lightcurve from the 2004/2005 outburst measured from the All-Sky Monitor on board of RXTE (Tsygankov et al., 2006)

The binary system is located at celestial coordinates of $RA = 03^h34^m59^s.89$, $Dec\, 0+53°10'23''.6$ at a distance of about 7 kpc away from us (Kreykenbohm et al., 2005). The orbital parameters of this system have been determined in 1983 by Stella et al. (Stella et al., 1985) and have been improved by Zhang et al. in 2005 (Zhang et al., 2005) by fitting the radial velocity curve (see table 3.1 for the parameters of the system). By updating those parameters, Zhang et al. could also redetermine the luminosity of the source to a value of $L \approx 5 \cdot 10^{37}$ erg/s.

The companion of the neutron star is the early-type star of spectral class O8-9Ve, BQ Cam (Tsygankov et al., 2006), which has got a visual brightness of $M_v = 15.4 \pm 0.02$ (Kreykenbohm et al., 2005). Right before each X-ray burst, about a year earlier, one could observe the brightening of the optical companion (Kreykenbohm et al., 2005) which is probably triggered by a sudden increase of the mass ejection rate from the companion star (Mowlavi et al., 2006).

3.2 Pulse Profiles

The pulse profiles of the source V0332+53 are highly asymmetric (Tsygankov et al., 2006) and intensity dependent (Zhang et al., 2005) (see figure 3.2). One can observe a change in the structure of the profiles from double-peaked to single-peaked (Tsygankov et al., 2006) and also a change of the phase separation of the double

$a_{\mathrm{x}} sini$	86^{+6}_{-10} lt − s
P_{spin}	$4.37480^{+0.00009}_{-0.00005}$ s
P_{orbit}	$34.67^{+0.38}_{-0.24}$ days
ϵ	$0.37^{+0.11}_{-0.12}$
ω	286 ± 14 degrees
$T_{\mathrm{periastron}}$	53367 ± 1 MJD
$\dot{P}_{\mathrm{spin}}$	$-8.01^{+1.00}_{-1.14} \cdot 10^{-6}$ s/day
$\dot{P}_{\mathrm{spin}}/P_{\mathrm{spin}}$	$-(1.83 \pm 0.23 \cdot 10^{-6}\,\mathrm{yr})$

Table 3.1: Parameters of V0332+53 (Zhang et al., 2005) with: $a_{\mathrm{x}} sini$: projected orbital radius in light seconds, P_{spin}: spin period, P_{orbit}: orbital period, *eccentricity*: eccentricity, ω: longitude of periastron, $T_{\mathrm{periastron}}$: time of periastron passage, $\dot{P}_{\mathrm{spin}}$: time derivative of spin period.

pulses with the source luminosity (Zhang et al., 2005). While the source was bright, the phase separation remained nearly constant at a value of about 0.47 and went down to 0.37 within a short time of about three days during which the source's luminosity decreased after the maximum intensity was reached (Zhang et al., 2005). Significant changes of the double-peaked structure of the pulse profiles can be seen as the intensity of the source goes down (Tsygankov et al., 2006). For a luminosity of about $L \approx 7.3 \cdot 10^{37}$ erg/s the profiles become asymmetric single-peaked at energies below the energy of the main harmonic cyclotron line, while it remains double-peaked above this energy (Tsygankov et al., 2006). According to Zhang et al. (Zhang et al., 2005) this may be explained due to a change of the dominance between fan- and pencil-beam emission. For high luminosities ($L > 10^{37}$ erg/s) the particles, which are decelerated on the neutron star's surface produce a radiative shock of photons, which can only escape perpendicularly to the magnetic axis of the star and therefore produce a fan-beam (Basko & Sunyaev, 1976). In this region, the pulse profiles are dominated by a double-peaked structure with a phase separation of about 0.47 (Zhang et al., 2005). This happens because we don't only see emission from one pole but also emission from the second pole. Due to the bright emission by the fan-beam, the second pole can also be seen if we don't look exactly onto the pole region. While the luminosity of the source is decreasing ($L < 10^{37}$ erg/s), there will be more and more contribution of a pencil-beam emission, for which the photons can escape along the direction of the magnetic axis of the neutron star (Zhang et al., 2005). This can also be seen in the pulse profiles in form of some emission in between the double-peaks which produces a broadened pulse and therefore a smaller phase separation (Zhang et al., 2005).

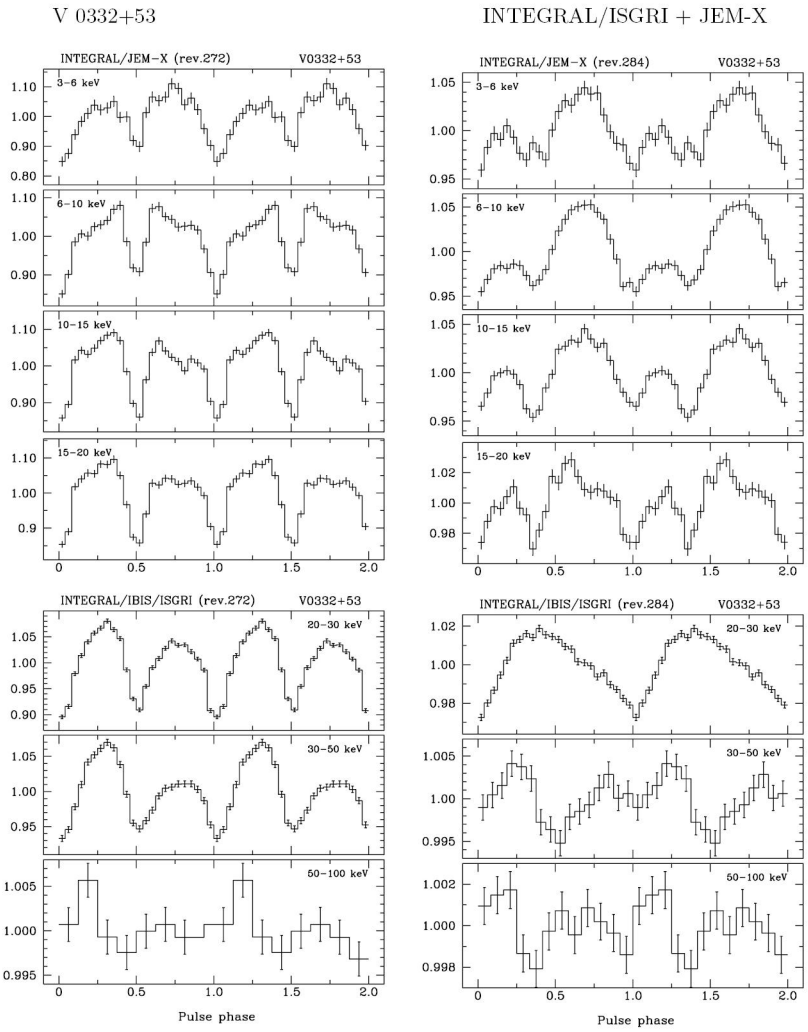

Figure 3.2: Pulse profiles of V0332+53 from Integral/ISGRI (15 keV-1 MeV (*http://hal.archives-ouvertes.fr/docs/00/03/04/06/PDF/PC3paper.pdf*)) and JEM-X (3-35 keV (*http://sci.esa.int/science-e/www/ object/ index.cfm? fobjectid=31175& fbodylongid=721*)) for different source intensities. Figure from Tsygankov et al. (2006).

3.3 Spectrum

Remarkable about this source is the presence of three cyclotron lines (Tsygankov et al., 2006) (see also figure 3.3 for a view of the energy spectrum of V0332+53). V0332+53 is only the second X-ray accreting pulsar which has got at least three cyclotron resonance scattering features, the main harmonic at $E_{\mathrm{cycl},1} \approx 26\,\mathrm{keV}$ and the first and second harmonics at $E_{\mathrm{cycl},2} \approx 50\,\mathrm{keV}$ and $E_{\mathrm{cycl},3} \approx 73\,\mathrm{keV}$ respectively (Tsygankov et al., 2006).

Those cyclotron lines origin from the quantized energy levels (Landau levels) perpendicular to the magnetic field lines. The spacing between those levels, can approximately be calculated to

$$E_{\text{cycl}} \approx \frac{\hbar e B}{m_e c} \approx 11.6 \frac{B}{10^{12}\,\text{G}} keV. \tag{3.1}$$

E_{cycl} is the energy of the fundamental cyclotron line and linearly related to the magnetic field strength of the neutron star. Cyclotron lines are observed as absorption lines in the spectrum (see e.g. figure 3.3).

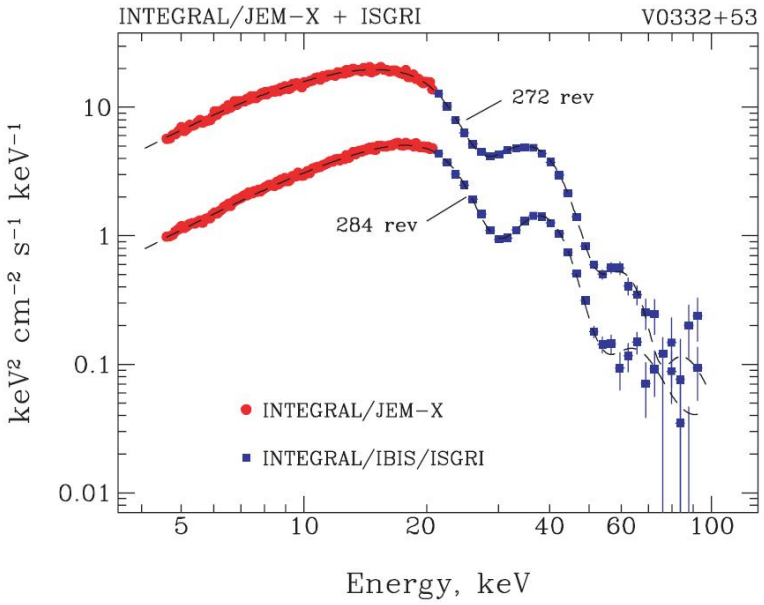

Figure 3.3: Energy spectrum of V0332+53 (Tsygankov et al., 2006)

The spectrum can be fitted using the cutoffpl model in xspec (see equation 3.2, Mowlavi et al., 2006), which consists of a power-law with an exponential cut-off to which one has to add three additional absorption lines (see equation 3.3, Mowlavi et al., 2006) representing the cyclotron resonance scattering features (Tsygankov et al., 2006).

Cutoffpl model: power-law plus exponential cut-off:

$$F(E) = A \cdot E^{-\Gamma} \cdot e^{-E/E_{fold}} \qquad \textit{Cutoffpl model} \tag{3.2}$$

Γ: power law index (differs from -0.18 to -0.4)

The three cyclotron lines can be fitted with (Mowlavi et al., 2006):

$$G_i\left(E\right) = \tau_i \cdot e^{\left(\frac{E-E_{cycl,i}}{\sigma_i}\right)^2} \tag{3.3}$$

$E_{\mathrm{cycl,i}}, \sigma_{\mathrm{i}}, \tau_{\mathrm{i}}$: cyclotron line energy, width and optical depth at center

Combining the cutoffpl model with the fit of the cyclotron absorption lines one gets the over-all spectral model of V0332+53 (see equation 3.4, Mowlavi et al., 2006). Mowlavi et al. only used two cyclotron lines for the fit, because the third has not enough statistics.

$$f\left(E\right) = F\left(E\right) \cdot e^{-G_1(E)} \cdot e^{-G_2(E)} \tag{3.4}$$

Appreciable is also the evolution of the line energy with the flux of the source (see figure 3.4, Tsygankov et al., 2006). For decreasing source luminosity the main harmonic cyclotron line energy increases nearly linearly, $E_{\mathrm{cycl,1}} \approx -0.10\,\mathrm{L}_{37} + 28.97\,\mathrm{keV}$ (L_{37}: L in $10^{37}\,\mathrm{erg/s}$), as well for the second harmonic, $E_{\mathrm{cycl,2}} \propto -0.1\,\mathrm{L}_{37}$ (Tsygankov et al., 2006). The coupling factor between fundamental and first harmonic cyclotron line is indeed 2.0 while it is a little bit lower as expected for the fundamental and second harmonic for which Kreykenbohm et al. (Kreykenbohm et al., 2005) determined a value of 2.85.

By having a look at the cyclotron line energies one can also estimate the magnetic field of the neutron star. Assuming that for low luminosities, the cyclotron line resonance scattering features originate from close to the surface of the star (Tsygankov et al., 2006), one gets a magnetic field of (Kreykenbohm et al., 2005):

$$B = \frac{1+z}{11.6} \cdot E_{\mathrm{cycl}} \cdot 10^{12}\,\mathrm{G} \approx 2.8 \cdot 10^{12}\,\mathrm{G} \tag{3.5}$$

for gravitational redshift $z \approx 0.25$ and $E_{\mathrm{cycl}} \approx 26\,\mathrm{keV}$.

For V0332+53, it is also important to mention that there are two Quasi Periodic Oscillations, one at 0.05 Hz and the other one at 0.23 Hz, which can be clearly seen in the power spectrum (Mowlavi et al., 2006). Those features originate from a region around the neutron star which is co-rotating with the pulsar (Mowlavi et al., 2006).

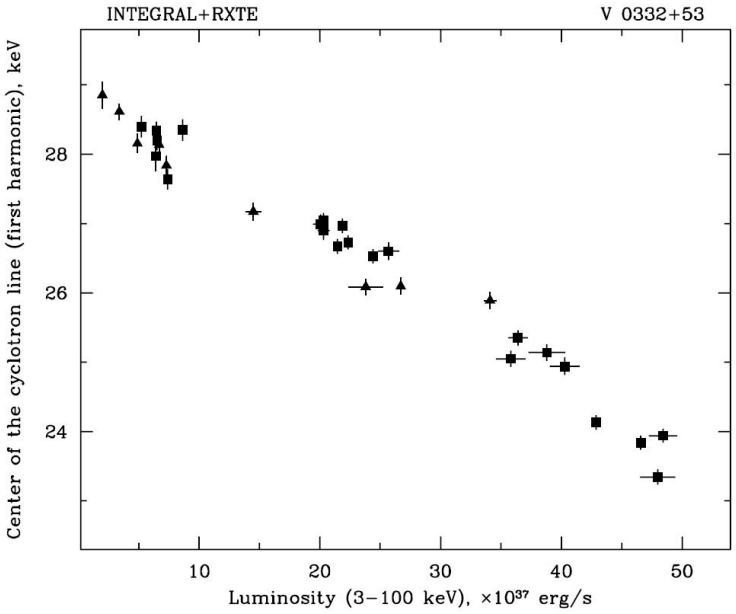

Figure 3.4: Linear decrease of the cyclotron line energy of the main fundamental cyclotron line with the intensity of the source (Tsygankov et al., 2006)

Chapter 4

Data reduction

4.1 Data files and modes

The data for the selected source V0332+53 were downloaded from the NASA Heasarc Browse on the NASA homepage (*http://heasarc.gsfc.nasa.gov/W3Browse/*). We downloaded data for the following observations:

- P90014
- P90089
- P90427

The downloaded data from RXTE are in form of FITS files. You may read more about all the headers and extensions and also the structure of those files in the ABC of XTE, available on the NASA's homepage (*http://heasarc.nasa.gov/docs/xte/abc/contents.html*).

As it can be read on this webpage, there are two main data formats, the science array format (extension XTE_SA), used for binned data, and the science event format (extension XTE_SE), which is used for unbinned data. To look at the header and extension header of the data file, to learn more about the configuration of the system, one uses the FTOOL **fdump**. In the header there is all the information about the data mode (keyword DATAMODE), the observatory and instrument (keyword TDDES), and the data in the several columns (keyword TDDESn). For example, TDDES1 represents the time column and in TDDES2 in a PCA Standard1 file the used detectors (e.g. D[1] means PCU 1 was on) and channels (e.g. C[0∼255] means channels 0 to 255) are shown. Additionally there are two extensions dealing with Good Time Intervals (GTI). The first GTI extension contains the times when: telemetred data are present, the satellite is pointing at the nominal source position

(as derived from the spacecraft attitude), the nominal source position is not occulted by the Earth (as predicted by mission operations) and the satellite is outside the South Atlantic Anomaly (SAA) (also predicted by mission operations). The second GTI extension contains the GTI corresponding to the times when telemetred data are present, for example just the first of the four criteria in the first GTI extension is applied (*http://heasarc.nasa.gov/docs/xte/abc/contents.html*).

For the selection of good data one needs the **Filter file** which can be found in the Standard Product subsystem. Filter files consist of BKGD_THETA, BKGD_PHI, TIME_SINCE_SAA, and ELECTRONn columns (*http://heasarc.nasa.gov/docs/xte/abc/contents.html*).

To look at the data we used the **XTE Data Viewer** (command >**xdf**). This tool allows us to find the **FITS files** necessary for further analysis. For the following analysis and work with those FITS files we used the **FTOOLS** version 30Nov2009_V6.8 package. To look in the files we worked with the program **fits view** which is started by the command >**fv**.

Due to the fact that we only used PCA data the following explanations about data reduction will focus on the PCA system. Before the measured data are telemetred to the ground the data are processed by the EDS on board of the RXTE satellite. The EDS consists of six Event Analyzers (EAs) for the PCA instrument. Two of them are always run in the Standard-1 and Standard-2 configuration. For the others there are seven basic configurations in which they can be run. Furthermore, the EDS rejects the background coming from the electronic system and adds the corresponding arrival time to each event. The main modes in which the Event Analyzers can be run are listed below (*http://heasarc.nasa.gov/docs/xte/abc/contents.html*). Note that the two modes we used are printed in bold and described in more detail.

- **Event mode:** data as a time-series of unevenly spaced events, each event described by arrival time, pulse height, PCU ID, etc. ;
  there are different configurations: Generic event, e.g. E_62us_0_17_500ms (means: 62 microsec time bin, channels 0 to 17, 500 ms read out time), Good Xenon and Transparent
- **Single-Bit:** stream of ones and zeros representing events and clock ticks, e.g. SB_125us_0_49_1s
- Binned data
- Burst Catcher mode
- Delta-binned mode

- Fast Fourier Transform mode
- Pulsar Fold mode

4.2 Data extraction

First of all we had to reduce the data to good events and get rid of unwanted data. To filter out bad data we needed to create a GTI file which means an interval in which we have got only good events and for this process we need the Standard 2 file. There are different criteria which are important for the filtering process. You may read more about them below.

Before filtering, it is good to have a short look at the filter file to see which values for the different parameters make sense. To do this, you can either plot different columns of the filter file by using **fplot** or you can plot all columns by running the command >**xv** on the files in the directories **stdprod/GIFS/*_xfl.gif** for each observation. An example is plotted below (figure 4.1).

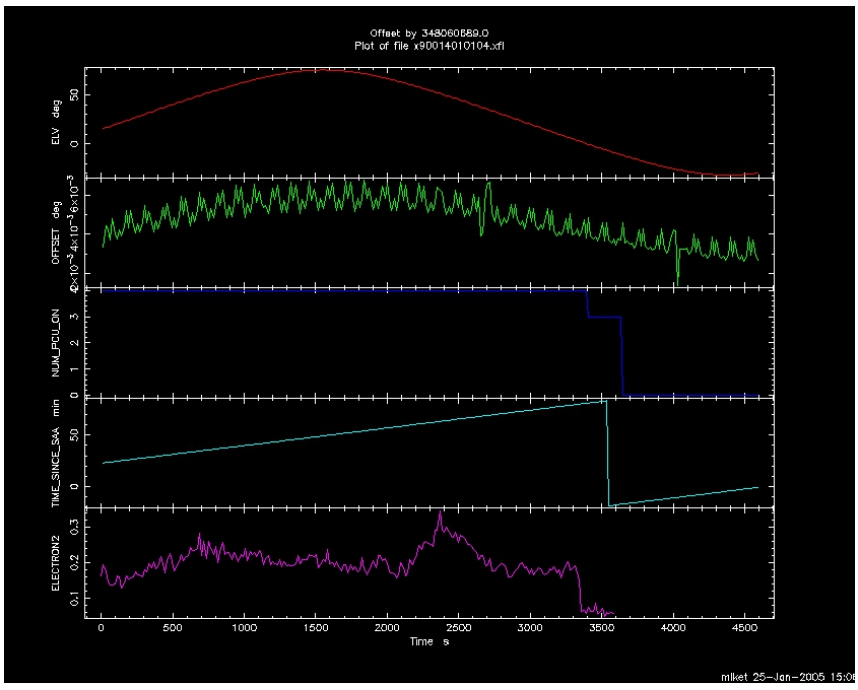

Figure 4.1: Information from the filter file plotted in order to look for wise filtering criteria

The filter file is used as input for the FTOOL **maketime** which produces the GTI file. What we get out is a file named ***.gti**. The program is called in accordance to the following example:

```
>maketime
Name of FITS file and [ext#][] /integralscratch/mueller/P90014/
90014-01-01-06/stdprod/x90014010106.xfl
Name of output FITS file[] 90014-01-01-06_basic.gti
Selection Expression[] ELV.gt.10.and.OFFSET.lt.0.02.and.NUM_PCU_ON.eq.3
Flag, yes if HK format is compact[yes] no
Column containing HK parameter times[TIME]
```

More details about the different filter criteria are listed in the following paragraph.

- OFFSET (pointing position): This column gives the difference between the source position and the pointing direction of the satellite. Sometimes, however, the on-source data file will contain short stretches of slew data at the beginning or end of an observation. These should be filtered out using the criterion: OFFSET < 0.02 (*http://heasarc.nasa.gov/docs/xte/abc/contents.html*).

- ELV (elevation angle): This column contains the angle, in degrees, between the Earth's limb and the target subtended by the spacecraft. Because the Earth's atmosphere absorbs X-rays the shape of the source spectrum is distorted when the elevation angle is low. One should limit the elevation angle for example to values greater than 10 degrees. A lower limit can be used for timing studies (*http://heasarc.nasa.gov/docs/xte/abc/contents.html*).

- PCUn_ON and NUM_PCU_ON: PCUn_ON is 1 when the PCU is completely turned on. One can plot all of the PCUn_ON columns to see which detectors are on and at what times (usually, they all go off and on together as they go in and out of the South Atlantic Anomaly (SAA)). The column NUM_PCU_ON is the sum of these columns. Data where different numbers of PCU are on must be analyzed separately (*http://heasarc.nasa.gov/docs/xte/abc/contents.html*).

- TIME_SINCE_SAA: Time in minutes to wait after a passage of the South Atlantic Anomaly (*http://pulsar.sternwarte.uni-erlangen.de/ wilms/ research/analysis/rxte/standard.html*). It is parameterized so that it jumps to negative values before SAA, and has a value of 99.99999 for orbits in which there is no SAA passage. When TIME_SINCE_SAA is between zero and for example 30 minutes, the background will increase dramatically, resulting in a lowering of the signal to noise. One should discard such data for faint sources (*http://heasarc.nasa.gov/docs/xte/abc/contents.html*). With newer PCA background models, a shorter time period, such as 10 minutes, is often enough (*http://pulsar.sternwarte.uni-erlangen.de/wilms/research/analysis/rxte/ standard.html*). We used 10 minutes because otherwise we would have discarded too much data.

- ELECTRONn: The PCA is subject to contamination from electrons trapped in the earth's magnetosphere or from solar flare activity. Such electrons increase the background at low energies. These electron values are usually identical across all the PCUs (*http://heasarc.nasa.gov/docs/xte/abc/contents.html*). Above this threshold value the particle background is considered too strong and no data are taken (*http://pulsar.sternwarte.uni-erlangen.de/wilms/research/analysis/rxte/standard.html*). We used a value which differs from 0.15 to 0.2 and 0.3 because otherwise we didn't have enough usable data points.

4.2.1 Create a bitmask

To exclude certain EDS housekeeping flags one has to apply a bitmask. To do so, one can use the program >**sefilter** which works as following:

```
>sefilter
Enter SE FITS file for filtering:[ ]@90014-01-01-06_genev.xdf
Input file is:
/integralscratch/mueller/P90014/90014-01-01-06/pca/FS4f_14bb3010-14bb3749
Enter the M-token to be processed (M[1]{1}):[M[1]{1}]
Enter the column name to be operated upon (Event):[Event]
Enter the output bitfile name to contain processed boolean expression:
[bitfile] 90014-01-01-06_bitfile
...
D-token values from 0 to 4 are present.
Do you want to filter on the D-token? [Yes, No]: yes
Enter the detector numbers of interest: [0,2-4]
The above syntax must be followed: 0,2,3
You entered 0,2,3.
Is this correct? [Yes, No]: yes
...
Enter the output filename to contain the processed data:
90014-01-01-06_ev.fits
Using output of sebitmask as input and running Fselect:
Completed running fselect and created 90014-01-01-06_ev.fits
```

4.2.2 Background estimation

The background estimation is done using the program >**runpcabackest** and works in detail as following example shows.

```
List of Standard mode 2 Science array FITS files (@filename):
@90014-01-01-06_std2.xdf
Output file which will contain the LIST of output files?:
90014-01-01-06_bkg.xdf
Suffix appended to the output background files (after underscore _):bkg
XTE Filter file: /integralscratch/mueller/P90014/90014-01-01-06/stdprod/
x90014010106.xfl (in filter.xdf)
```

```
PCA Background model file:[@modelfile]/xtescratch/sasaki/
pca_bkgd_cmbrightvle_eMv20051128.mdl
Seconds between succesive estimates:[16]0.125
Include individual xenon layer spectra? (Yes, No):[yes]no
Correct for PCU Xenon gain variations? (Yes, No):[no]yes
EDS gain correction file (CALDB) :[]caldb
PCA SAA passage history file:/xtescratch/sasaki/pca_saa_history.gz
Compute systematic error estimate? (Yes, No):no
...
Generated output file: bkg.xdf.
This file contains the names of the output files.
This file can be input into SAEXTRCT using the @filename option.
Update Parameter file for PCABACKEST? (Yes, No):yes
PCABACKEST parameter file updated.
```

4.2.3 Create background subtracted lightcurves

To create lightcurves we used >**saextrct** (for binned data) or >**seextrct** (for event data) depending on the data mode. An example for the calling sequence of the program is shown below.

```
>seextrct infile="90014-01-01-06_ev.fits" gtiorfile=APPLY gtiandfile=
"90014-01-01-06_basic.gti" outroot="90014-01-01-06_ev_21_60 timecol="TIME"
columns="EVENT" binsz=0.125 printmode=LIGHTCURVE lcmode=RATE
spmode=SUM timemin=INDEF timemax=INDEF timeint=INDEF chmin=51 chmax=140
chint="INDEF" chbin="INDEF"
```

The same kind of extraction can be done for the background.

```
>saextrct infile="@90014-01-01-06_bkg.xdf" gtiorfile=APPLY gtiandfile=
"90014-01-01-06_basic.gti" outroot="90014-01-01-06_bkg_21_60" accumulate=
"ONE" timecol="TIME" columns="GOOD" binsz=0.125 printmode=LIGHTCURVE
lcmode=RATE spmode=SUM timemin=INDEF timemax=INDEF timeint=INDEF chmin=51
chmax=140 chint="INDEF" chbin="INDEF"
```

The subtraction of the background can be done using the tool **lcmath** as following.

```
>lcmath infile="90014-01-01-06_ev_21_60.lc" bgfile="90014-01-01-06_bkg_21_60
.lc" outfile="90014-01-01-06_ev_21_60_bkgsub.lc" multi=1. multb=1.
addsubr=no
```

4.2.4 Barycentre correction

Due to the movement of the satellite around the earth and of the earth around the sun one should correct the effects of this motion by applying a correction of the times to the Solar System Barycentre. This is done by using the program >**faxbary** plus the ephemerides data which can be downloaded from the XTE Data Viewer.

```
faxbary barytime=no infile="90014-01-01-06_ev_21_60_bkgsub.lc" outfile=
"90014-01-01-06_ev_21_60_bary.lc" orbitfiles="@90014-01-01-06_ephem.xdf"
```

What we get out are files which are named as for example ***_bary.lc**.

4.2.5 Data extraction and reduction for all observations

This process of making the GTI file and discarding bad data and applying a barycentre correction, as described above, can be done step by step or, as we did for the high number of all observations, by the use of a routine. We used a routine, written by Jörn Wilms, who has been working at our institut (Institut for Astronomie and Astrophysics, Uni Tübingen). For the standard analysis we used the program **allex** and for the extraction of high resolution data the program **allex_hires**. A short script which runs those routines can be read below.

Script for program **allex**:

```
setenv XTETOOLS /xtearray/xtescripts
setenv PCACAL /xtearray/calibration/

set pcaex= $ {XTETOOLS}/pcaextract
set obspath=/integralscratch/mueller/P90089/

foreach obsid (P90089/*)
cd $obsid
${pcaex} $obsid ${obspath} 00.01 \
-saa=10 -electron=0.15 -full
cd ..
end
```

This scripts runs **pca_standard** (or eaextract if selected).

The parameters chosen in the script above say that the time since SAA passage is 10 minutes and that the electron ratio is 0.15. The argument **-full** produces a full energy resolution raw background file in the pcabackest_full directory and is necessary to be able to produce the background for high-resolution lightcurves and spectra later.

To extract high resolution lightcurves and spectra one needs to run the program **eaextract** which is called from the **pcaextract** program. The standard_2f data products should be extracted before, using the **pca_standard** script (e.g. called by **pcaextract**). pcaextract is run with the option **-ea=N**, where N is the number of the event analyzer (EA) for which we want to extract high-resolution data. For analyzing **GoodXenon** data, we had to set **-ea=-1**. To produce background lightcurve for the corresponding energy range we used the option **-ea=backfull**. The background is only available with a time resolution of 16 s. Therefore, it is

necessary to interpolate it before the subtraction from the source lightcurve, which is done automatically using lcmath.

Script for program **allex_hires**:

```
setenv XTETOOLS /science/satscripts/xtescripts
setenv PCACAL /xtearray/calibration/

set pcaex=$ {XTETOOLS}/pcaextract
set obspath=/integralscratch/mueller/P90089/

foreach obsid (90089*)
cd $ obsid $ {pcaex} $ obsid $ {obspath} 00.01
-ea=1 -dt=7 -bary 50  71 cd ..
end
```

With:
-ea: Event Analyzer number
-dt: time interval (small $\rightarrow$ higher resolution) e.g. dt=7 $\rightarrow \frac{1}{2^7}$
-bary: also produces barycentre corrected time column
channels: minimum and maximum channel

Having a look at the output data one can see which PCU were out, for example ***.ea1.log** means PCU 1 was out. What we get out from the script allex_hires are 2 files, ***.lc** and ***_bary.lc**. In the *_bary.lc file there are two time columns, the first column TIME is the original non-barycentre corrected time, while the fifth column BARYTIME shows the barycentre corrected time, which we are going to use for the following analysis.

4.3 Background subtraction

By running the program from above again with the parameter **-ea** set to **-ea=backfull**, we could extract the high resolution background lightcurves for the according energy bands. Afterwards, we could subtract the background using a script which subtracts the background for each observation and each energy band using lcmath (in directory **/integralscratch/mueller/behelfsprogramme/backgroundsubtract/backgroundsubtract.tcsh**). The output files are called ***_backsub_bary.lc**. Although the background has only a time resolution of 16 s the subtraction process doesn't make any problems because lcmath interpolates in between the data points automatically.

4.4 Binary correction

To correct the effects of the binary motion we used the program **fits_ binarycor_0.pro** which has to be run on IDL and uses the T0 time (time in

MJD at which the mean orbital longitude of the neutron star is 0°). As input time one has to take the barycentre corrected time, namely the column BARYTIME. To do so, we wrote a little script, called **binarycor.tcsh** in the directory **feinaufteilung_backsub_bary_bincor/gutepulsprofile/binarycor.tcsh**.

We used the orbital parameters of S. Zhang et al. who determined the ephemerides for the outburst of 2004/2005 (Zhang et al., 2005). The orbital parameters can be read in table 3.1. The output files were named ***_backsub_bary_bincor.lc** and are located in the folder ***/feinaufteilung_backsub_bary_bincor/gutepulsprofile/*backsub_bary_bincor.lc**. The column BARYTIME was changed to the binary corrected time. We did the binary correction only for the files we later used for the following up analysis (see section 4.7 *Selected observations and additional data*).

4.5 Search for the period

To search for the period of the neutron star we used the FTOOL **efsearch**. This tool works with the epoch folding technique. In this technique, the events are summed up according to their phase with respect to a trial period. Then, a value χ^2 is calculated which gives us the deviation from a flat distribution. So, what one needs is the lightcurve and a trial period P and a start time, for example the time for the first event (used by just typing INDEF when asked in the program). If the trial period and the lightcurve fit together well, one gets a high value for χ^2. At the end χ^2 should be maximal.

We wrote a script **period_efsearch_routine.tcsh** which takes all observations, one after the other, and has a start value for the period of P=4.375 s, which we got from various papers. The routine searches for a better period fit and thereby uses the obtained value for the period as a new start value for the next run. We started the search with a resolution of dres=0.001 s and went down to 0.000 000 1 s. The periods obtained after the last run were written in a text file **period.txt**.

4.6 Produce pulse profiles

4.6.1 Fold lightcurve

By using the FTOOL **efold** one can fold the lightcurve ***_backsub_bary_bincor.lc** with the period obtained from the epoche folding technique described above. To do this for all the observations we used a script **fold.tcsh** and got output files ***_backsub_ bary.fef** and postscript files ***_backsub_bary.ps**.

4.6.2 Shift and norm pulse profiles

First of all we plotted the pulse profiles over two phases for a better view of the different features. This is done with the routine **phase2.tcsh** located in **feinaufteilung_backsub_bary_bincor/gutepulsprofile/** which runs the IDL program **plot_2ph.pro** and produces profiles plotted over two phases and normed to one. It makes sense to shift all pulse profiles with respect to a certain feature in order to be able to compare the different profiles better. We did this by fitting the minimum with a Gaussian corresponding to phase zero with the program **find_ph0.pro**. Because the pulse profiles often have got two minima and it is difficult to say which minima correspond to each other, we also looked onto the evolution of the different pulse profiles and compared profiles which should have about the same luminosity in order to identify the minima. Afterwards we were able to shift all the profiles with respect to the reference phase found before. This is done by the routine **calc_ph0_norm.pro** which produces files ***_backsub_bary_ph0_norm.dat**.

4.7 Selected observations and additional data

To select observations for the pulse profile decomposition we looked at the statistics of each observation by using the FTOOL **fstatistic** which gives us the sum and mean count rate for a certain observation. We selected observations with high statistics which were distributed over the whole outburst and for which we had data of the same energy ranges. All the good files were put in a directory **/feinaufteilung_backsub_bary_bincor/gutepulsprofile/**. The selected energy bands are:

channels	**energy range**
0-17	0-7 keV
18-49	7-20 keV
50-71	20-30 keV
72-255	$>$ 30 keV

As we learned later, while doing the pulse profile decomposition, we needed some more decompositions for the time of the end of the outburst. Those pulse profiles were put in a directory **add_data**.

A list of all observations selected and later used for the decomposition method is shown in table 4.1. The luminosity was taken from Tsygankov et al. (2006)

(3-100 keV range) and for the missing observations scaled with the averaged PCA countrates from rxtescreen.

observation ID	date	MJD	exp. time (s)	L_{37}
90089-11-02-08	2004-12-07	53346	2735	25.8
90089-11-03-04	2004-12-14	53353	3317	41.0
90089-11-04-03	2004-12-19	53358	1415	45.7
90427-01-01-01	2004-12-29	53368	2248	48.1
90427-01-02-02	2005-01-06	53376	887	38.7
90014-01-01-04	2005-01-11	53381	3383	33.5
90014-01-05-01	2005-02-06	53407	8515	11.4
90427-01-04-04	2005-02-13	53414	10143	7.9

Table 4.1: Selected observations for the pulse profile decomposition method. The luminosity L_{37} is measured in 10^{37} erg/s.

The selected observations are also marked in an ASM lightcurve of the 2004/2005 outburst to get a better overview of the time of the observation relative to the outburst maximum (see figure 4.2).

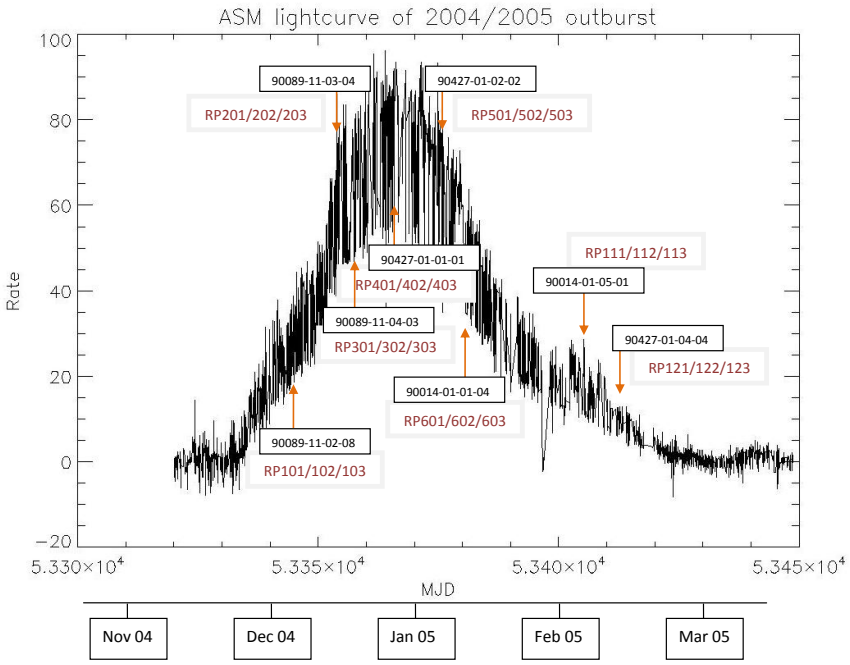

Figure 4.2: Lightcurve of the 2004/2005 outburst from the ASM, the selected observations for the pulse profile decomposition are marked

The corresponding pulse profiles for all four energy ranges are attached in the figures 4.7 and 4.8 on page 46/47.

At the end, we copied the files ***_ph0_norm.dat** to the directory **/zerlegen_ueberlegen/zerlegen/input_profiles** and the additional data to **/zerlegen_ueberlegen/zerlegen/add_data/add_input_profiles/**.

4.8 Long time lightcurve

4.8.1 RXTE screen

Using **rxtescreen** which runs the program screen.pro on IDL, one can plot a long time lightcurve of all observations and for each single observation a lightcurve and the information in the filter file. A plot for the outburst of 2004/2005 is shown in figure 4.4 and additionally with the two more recent outbursts in figure 4.3.

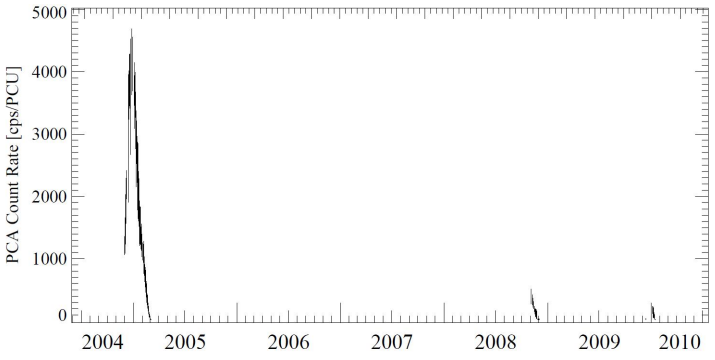

Figure 4.3: Long time lightcurve made with rxtescreen for the 2004/2005, the 2008 and the 2009/2010 outburst

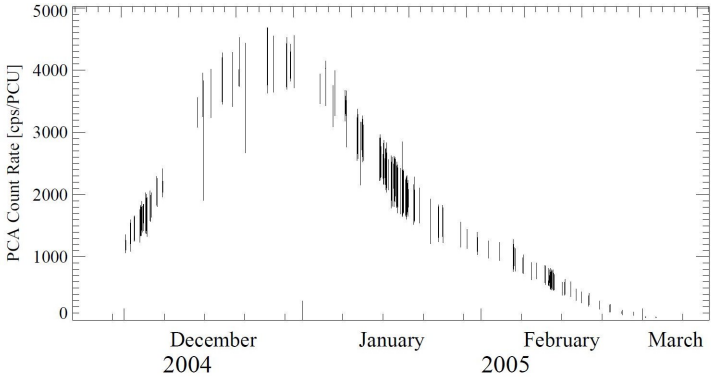

Figure 4.4: Long time lightcurve made with rxtescreen for the 2004/2005 outburst

4.8.2 ASM

Another possibility to produce a long time lightcurve for a certain source is to use the data from the ASM. One can obtain ASM data from *http://xte.mit.edu/ASM_lc.html*. Then, the data should be copied to a list as text file, for example **ASM_04_05.txt**. In this file one can see the different columns: time in MJD, Intensity, Uncertainty of Intensity. To plot the lightcurve we run the script **ASM_04_05.pro** on IDL which reads the text file from before and plots the time versus the ASM count rate for a certain x-range. A lightcurve of the 2004 and the two recent outbursts is shown in figure 4.5 and a plot zooming to the outburst of 2004/2005 in figure 4.6. Note that we just plotted the data from the ASM without making any reduction only to give you an idea of the long time behavior of the source.

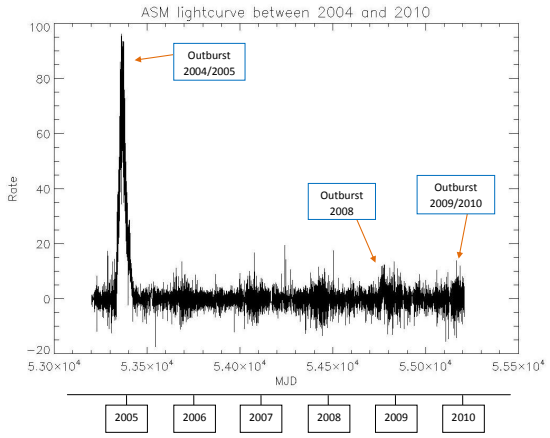

Figure 4.5: ASM lightcurve of the 2004/2005 outburst and the two less intense outbursts of 2008 and 2009/2010

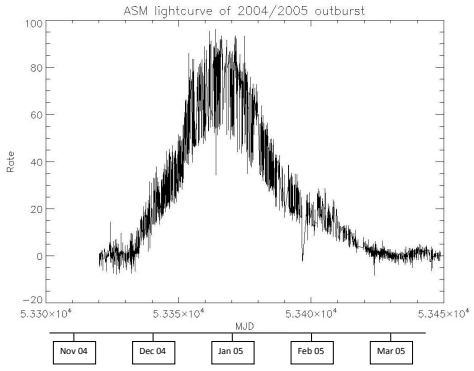

Figure 4.6: ASM lightcurve of the 2004/2005 outburst

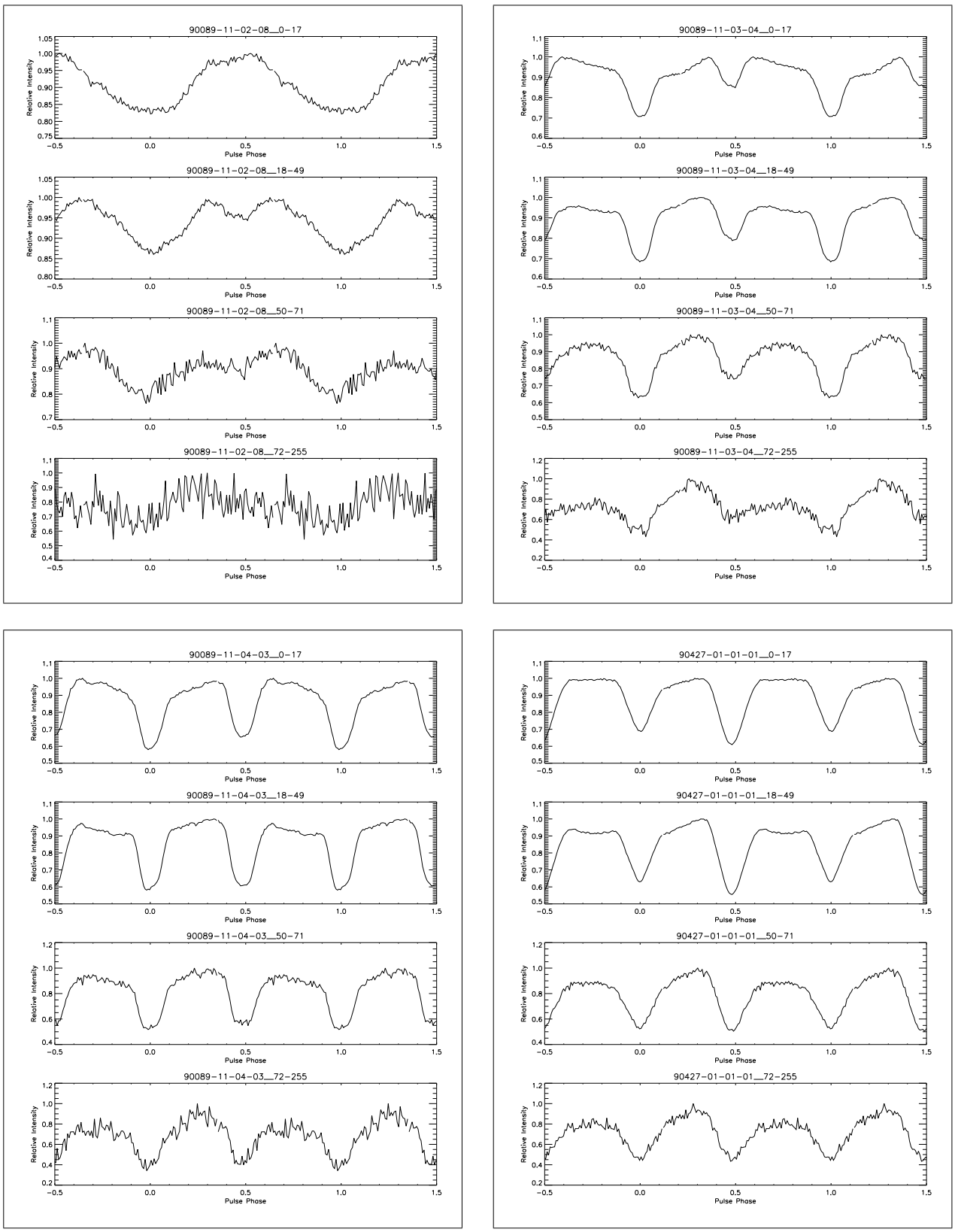

Figure 4.7: Pulse profiles of the first four from eight selected observations for respectively four energy bands (0-7 keV,7-20 keV, 20-30 keV, $>$ 30 keV, sorted from up to down). The profiles are sorted according to the start time of their observation (MJD 53346 - up left, 53353 - up right, 53358 - down left, 53368 - down right).

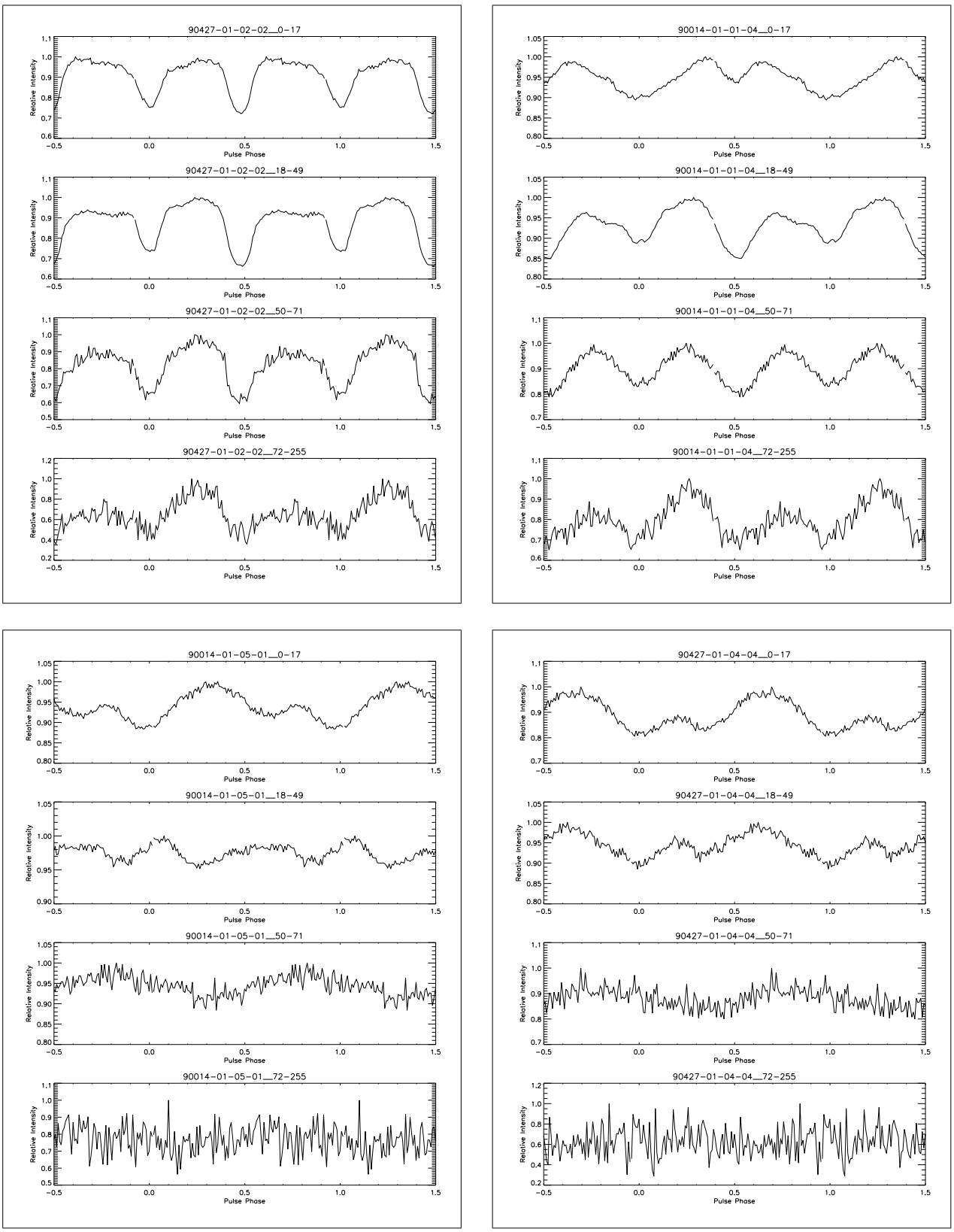

Figure 4.8: Pulse profiles of the first four from eight selected observations for respectively four energy bands (0-7 keV,7-20 keV, 20-30 keV, $>$ 30 keV, sorted from up to down). The profiles are sorted according to the start time of their observation (MJD 53376 - up left, 53381 - up right, 53407 - down left, 53414 - down right).

Chapter 5

Decomposition

5.1 General method

The method about the **decomposition of pulse profiles to their single-pole contributions** was originally developed and improved by Ute Kraus (see e.g. Kraus et al., 1995; U. Kraus, 2007). For a better understanding of the following description of the method we suggest first to take a look at the plots below (figure 5.1) to get a better overview of the geometry of the neutron star.

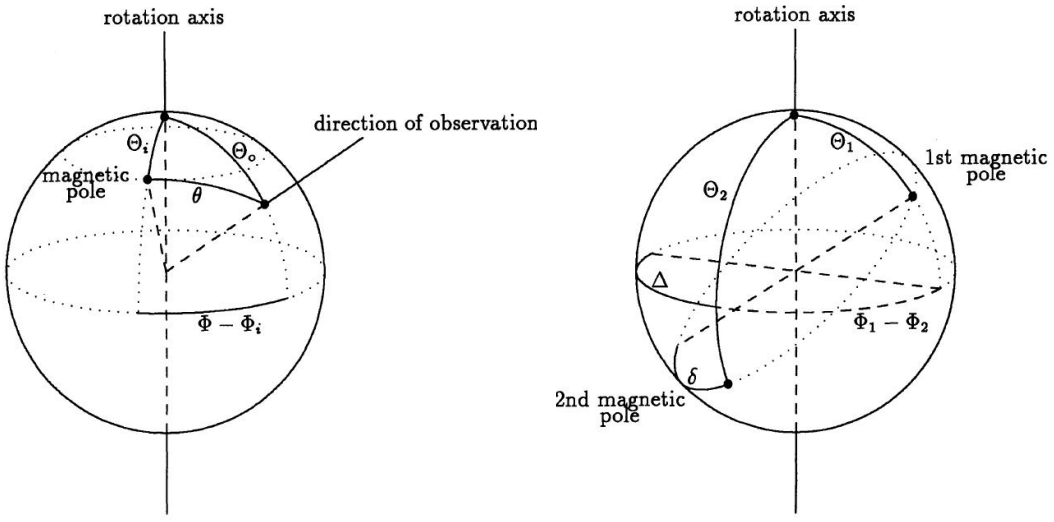

Figure 5.1: Schematic view of the geometry of a neutron star: Θ_0 polar angle between direction to the observer and rotation axis, Θ_1 polar angle of pole 1, Θ_2 polar angle of pole 2, Θ viewing angle between direction of observation and axis through magnetic pole, ϕ rotation angle of neutron star, $\phi_1 - \phi_2 = \pi - \Delta$ difference in azimuthal angles, δ angular distance of second pole from antipodal position. See Kraus et al. (1995).

So, how do we get from the intrinsic emission region and characteristics to the observed asymmetric and energy dependent pulse profiles?

The observed beam pattern of each pole is determined by the local emission characteristics and also by the relativistic light deflection due to the high compactness of a neutron star (Blum & Kraus, 2000). The beam pattern combined with the geometry of the system gives us the pulse profile of one single pole. Now, taking both poles together, one gets the total pulse profile which is observed by a distant observer (Blum & Kraus, 2000).

The method is based on two fundamental assumptions:

- **Asymmetry in pulse profiles due to a distorted magnetic field**
- **Single-pole pulse profiles are symmetric**

Those assumptions are essential for being able to apply the decomposition method. However, the asymmetry of the observed pulse profiles could also originate for example from the presence of an accretion disk for which the magnetic axis is not orientated perpendicular to the disk. Here, the accretion rate may be higher in the leading side of the accretion region and the beam patterns may not be symmetric anymore (Kraus et al., 1995). We now assume that there is no asymmetry somewhere in the accretion process but an asymmetry of the position of the two magnetic poles is present. That means, the two poles are not located opposite from each other and therefore the symmetry points, one for each single-pole pulse profile, do not coincide (Kraus et al., 1995). The second assumption, that the single-pole pulse profiles are symmetric, means that the emission regions have got axisymmetric beam patterns Kraus et al. (1995).

To give an overview over the following much more detailed steps of the pulse profile decomposition method we want to summarize them shortly.

We start from the total pulse profile that consists of contributions from each single pole. We then decompose the total pulse profile into two single-pole profiles which are symmetric. Then, each single-pole pulse profile can be transformed into a section of beam pattern. By having a closer look at the two beam patterns, one for each pole, one may recognize a similar section in the beam patterns. By shifting one beam pattern with respect to the other, it is possible to overlay the beam patterns and get the total visible part of beam pattern for one magnetic pole. Finally, one should also take into account the relativistic light deflection due to the compactness of the neutron star and what we get is the intrinsic

emission beam pattern of one single pole. What remains is the final interpretation of the obtained solutions. In the following we will go through all those steps in detail.

5.1.1 Decomposition of total pulse profile into single-pole contributions

As amentioned above, we assume that **each single-pole pulse profile is symmetric** which basically means that we have got **two equal emission regions** (Kraus et al., 1995). If those **two symmetric contribution $\mathbf{f_1}$** and **$\mathbf{f_2}$** have **symmetry points $\boldsymbol{\phi_1}$** and **$\boldsymbol{\phi_2 + \pi}$** which do not coincide, the sum of the two parts gives an **asymmetric total function $\mathbf{F}(\boldsymbol{\phi})$** (see equation 5.4) which represents the total pulse profile.

What we now do is we write the total asymmetric but periodic pulse profile $F(\phi)$ as a **Fourier sum**, which means as a sum of symmetric functions (see equation 5.1). The pulse profile should be completely determined by the n Fourier coefficients. The same can be done for the single-pole pulse profiles for which we get a Fourier series with symmetry points ϕ_1 (see equation 5.2) and $\phi_2 + \pi$ (equation 5.3). Here, symmetry point means that the coefficients of the sinus terms vanish in the Fourier decomposition.

$$F(\phi) = \frac{1}{2}u_0 + \sum_{k=1}^{(n/2)-1} [u_\mathrm{k}\ cos(k\phi) + v_\mathrm{k}\ sin(k\phi)] + u_{\mathrm{n}/2}\ cos\Big(\frac{n}{2}\phi\Big) \tag{5.1}$$

$$f_1(\phi) = \frac{1}{2}c_0 + \sum_{k=1}^{n/2} c_\mathrm{k}\ cos[k(\phi - \phi_1)] \tag{5.2}$$

$$f_2(\phi) = \frac{1}{2}d_0 + \sum_{k=1}^{n/2} d_\mathrm{k}\ cos\{k[\phi - (\phi_2 + \pi)]\} \tag{5.3}$$

$$F = f_1 + f_2 \tag{5.4}$$

If the function (f_1-constant) is a solution, (f_2+constant) is a solution as well. Therefore, each choice of symmetry points corresponds to a unique decomposition into two symmetric functions (Blum & Kraus, 2000). If we now compare the coefficients of the $sin(k\phi)$ and $cos(k\phi)$ terms we get some relations for the different coefficients:

$$u_0 = c_0 + d_0 \tag{5.5}$$

$$u_\mathrm{k} = c_\mathrm{k}\ cos(k\phi_1) + d_\mathrm{k}\ cos[k(\phi_2 + \pi)] \tag{5.6}$$

$$v_\mathrm{k} = c_\mathrm{k}\ sin(k\phi_1) + d_\mathrm{k}\ sin[k(\phi_2 + \pi)] \tag{5.7}$$

Then, we can change the form of the equations a little bit by transforming the two dimensional parameter space of ϕ_1 and ϕ_2 to ϕ_1 and $\boldsymbol{\Delta = \pi - (\phi_1 - \phi_2)}$ to get a better view of the regions with positive decompositions (see equations 5.8 and 5.9).

$$\tilde{u}_\mathrm{k} = c_\mathrm{k} + d_\mathrm{k}\ cos(k\Delta) \tag{5.8}$$

$$\tilde{v}_\mathrm{k} = d_\mathrm{k}\ sin(k\Delta) \tag{5.9}$$

This gives us the shift from the antipodal position in terms of rotation angle. The symmetry point of the first pulse profile ϕ_1 is displaced by a value Δ with respect to the second symmetry point $\phi_2 + \pi$.

$$\tilde{u}_\mathrm{k} = u_\mathrm{k}\ cos(k\phi_1) + v_\mathrm{k}\ sin(k\phi_1) \tag{5.10}$$

$$\tilde{v}_\mathrm{k} = -u_\mathrm{k}\ sin(k\phi_1) + v_\mathrm{k}\ cos(k\phi_1) \tag{5.11}$$

After having done the steps from above we typically get, of course depending on the case, a huge number of possible decompositions. To reduce this number of mathematical solutions one should take into account physics. Mainly there are three physical criteria which have to be applied in order to get a reasonable solution:

- f_1 **and** f_2 **not negative:** Because f_1 and f_2 are representing fluxes, they shouldn't be negative in order to represent a reasonable physical solution
- **no-ripples criterion:** The two single-pole profiles shouldn't have too many ripples which are exactly cancelling out in their sum. This can be explained by two ideas. On the one hand, one doesn't expect the single-pole pulse profiles to be much more complicated than the total pulse profile and on the other hand, the single-pole pulse profiles are generated independently and without being in connection to each other. Therefore, they shouldn't have features which cancel

out exactly in the sum (see also figure 5.2 for a pulse profile which should be rejected) (Kraus et al., 1995).

- **decomposition energy independent:** The solution of the decomposition is simply a geometric result. If one does the decomposition independently for different energy bands there should somehow arise some regions in which we have a good decomposition for all energy bands, because the location of the poles should not change with the energy.

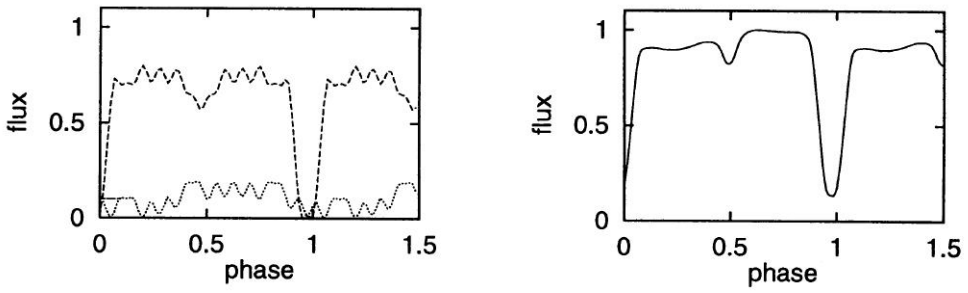

Figure 5.2: Decomposition of a pulse profile in two single-pole contributions. This pulse profile should be rejected due to the no-ripples criterion (Kraus et al., 1995).

5.1.2 Transformation into total visible part of beam pattern

If we now have a look at the single-pole pulse profiles we can transform them into a **section of beam pattern** by writing them as a function of $\mathbf{cos}(\boldsymbol{\phi} - \boldsymbol{\phi}_\mathrm{i})$. Here ϕ_i is the rotation angle with the smallest value of viewing angle Θ. The viewing angle Θ changes with the rotational angle ϕ (Blum & Kraus, 2000). One ambiguity arises because by doing this transformation one cannot exactly say which symmetry point of the pulse profile corresponds to ϕ_1. Therefore we just pick one symmetry point ϕ_1' and for the second pulse profile we take the one which is nearest to the antipodal position which means nearest to $\phi_1' + \pi$ and call it ϕ_2'. Now, we can write the beam patterns as a function of $cos(\phi - \phi_1')$ and $cos(\phi - \phi_2')$. Because we don't know if the symmetry point is ϕ_1' or $\phi_1' + \pi$, we always get two solutions, a *plus* and a *minus* solution (see equation 5.12).

$$cos(\phi - \phi_\mathrm{i}) = \pm cos(\phi - \phi_\mathrm{i}') \tag{5.12}$$

The decision which solution is the right one can only be made by looking at the beam patterns and thinking about possible physical explanations.

If we now have a look at the different sections of beam patterns from the two poles, we might see some similarity. If this is the case we can shift one beam pattern with respect to the other in order to get the total beam pattern (see equation 5.13). This is possible if we have got an **overlapping region**. At a certain angle ϕ'_1 some part of the emission region of the first pole is seen while at another angle ϕ'_2 the same part of emission region of the second pole is seen (Blum & Kraus, 2000). The size of this overlapping region is determined by the geometry of the system and therefore should be the same for different energy bands. We get

$$cos(\phi - \phi'_1) = a' + b'\ cos(\tilde{\phi} - \phi'_2) \tag{5.13}$$

for ϕ and $\tilde{\phi}$ in overlapping region.

To obtain the complete geometric location of the poles one has to determine or assume an additional parameter, the angle between rotation axis and axis to the observer Θ_0 to get all four parameters (Θ_1, Θ_2, Δ and Θ_0). For each value of Θ_0 there are two possible solutions (*plus* and *minus*) for Θ_1 and Θ_2 corresponding to the two choices of $\phi'_{\rm i}$ (Kraus et al., 1995). At the end you may express the total visible section of beam pattern as function of $cos\Theta$ and from that as function of Θ (see equation 5.14).

$$cos\Theta = cos\Theta_0\ cos\Theta_{\rm i}\ +\ sin\Theta_0\ sin\Theta_1 cos(\phi - \phi_{\rm i}) \tag{5.14}$$

The range in the values of Θ depends upon the location of the magnetic poles and upon the **direction to the observer $\mathbf{\Theta_0}$**. You should also keep in mind that the assumption of a certain value for Θ_0 remains a big factor of uncertainty over the whole process of beam pattern determination (Kraus, 2001).

5.1.3 Intrinsic beam pattern

To get the intrinsic emission characteristics of the magnetic poles of the neutron star one has to use a model. Additionally, one should take into account **relativistic light deflection** due to the compactness of the neutron star. The radiation which is emitted by the neutron star is attracted to itself by its own gravitation. The **intrinsic emission angle $\mathbf{\Theta}_{\rm intr}$** of the radiation is therefore not the same as the angle Θ under which we observe the radiation from a distant point of view (see figure 5.3). To get the intrinsic beam pattern one has to make some assumptions. First of all, we assume that the radiation originates from a point source on the surface of the neutron star and then, we also assume a certain mass and radius. By tracing back

the track of the radiation and assuming that the radiation follows a null geodesic in Schwarzschild space time we can get the intrinsic emission characteristics from the beam pattern observed by a distant observer by equating the fluxes in corresponding elements of solid angle. The Schwarzschild metric is appropriate to use for slowly rotating neutron stars (Kraus, 2001).

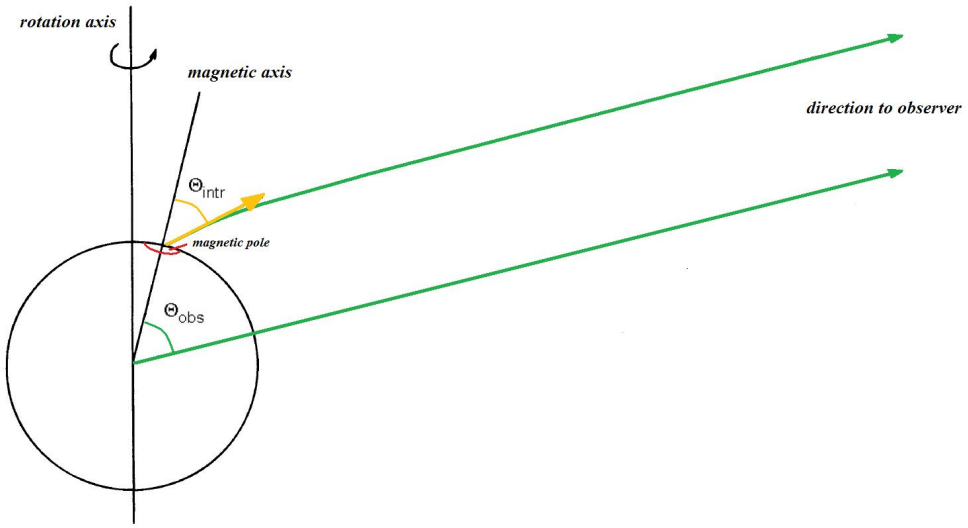

Figure 5.3: Relativistic light deflection: intrinsic emission angle $\Theta_{\rm intr}$ and observed emission angle Θ. Original figure from Kraus et al. (1996).

5.2 Application to V0332+53

5.2.1 Decomposition

For the pulse profile decomposition we selected a set of observations covering the whole span of time of the 2004/2005 outburst from the beginning of December 2004 until mid of February 2005. We selected observations which have got good statistics and for which the energy disposition was possible in the following energy bands:

- 0-7 keV
- 7-20 keV
- 20-30 keV
- $>$ 30 keV

The input profiles were produced as described in the chapter *Data reduction*. We copied those profiles in a new directory **/integralscratch/mueller/**

zerlegen_ueberlegen/zerlegen/input_profiles. The whole process of pulse profile decomposition described above is done using the program **zerl** which reads a script **zerl.ein**. At the beginning we renamed the observations according to table 5.1.

Observation	Energy channels	renamed as	Luminosity
90089-11-02-08	0-17 18-49 50-71 72-255	RP101 RP102 RP103 RP104	25.8 x 10^{37} erg/s
90089-11-03-04	0-17 18-49 50-71 72-255	RP201 RP202 RP203 RP204	41.0 x 10^{37} erg/s
90089-11-04-03	0-17 18-49 50-71 72-255	RP301 RP302 RP303 RP304	45.7 x 10^{37} erg/s
90427-01-01-01	0-17 18-49 50-71 72-255	RP401 RP402 RP403 RP404	48.1 x 10^{37} erg/s
90427-01-02-02	0-17 18-49 50-71 72-255	RP501 RP502 RP503 RP504	38.7 x 10^{37} erg/s
90014-01-01-04	0-17 18-49 50-71 72-255	RP601 RP602 RP603 RP604	33.5 x 10^{37} erg/s
90014-01-05-01	0-17 18-49 50-71 72-255	RP111 RP112 RP113 RP114	11.4 x 10^{37} erg/s
90427-01-04-04	0-17 18-49 50-71 72-255	RP121 RP122 RP123 RP124	7.9 x 10^{37} erg/s

Table 5.1: Naming of observations for pulse profile decomposition. Luminosity as in section *4.7*.

The whole process of pulse profile decomposition is done using the manual *ZERLegen von Pulsprofilen und UEBerlagern von Einpolpulsen* U. Kraus (2007) written by Ute Kraus and Steffen Blum. The first step of the method is, as described above, the decomposition of the total asymmetric pulse profile into two symmetric contributions f_1 and f_2. We write the total pulse profile as a Fourier sum F. $F(\phi)$ can then be written as a sum of f_1 and f_2 which have got symmetry points ϕ_1 and ϕ_2 respectively. For the Fourier decomposition we only used so many coefficients that the original pulse profile is described well and all important features are represented. We took 38 Fourier coefficients in order to get useful results. The reproduced pulse profiles can be seen by plotting the file ***.npuls** in gnuplot. To compare the original pulse profiles with the reproduced ones we used the script **plot.pulsprofiles+fourier** which has to be loaded in gnuplot (see figure 5.4).

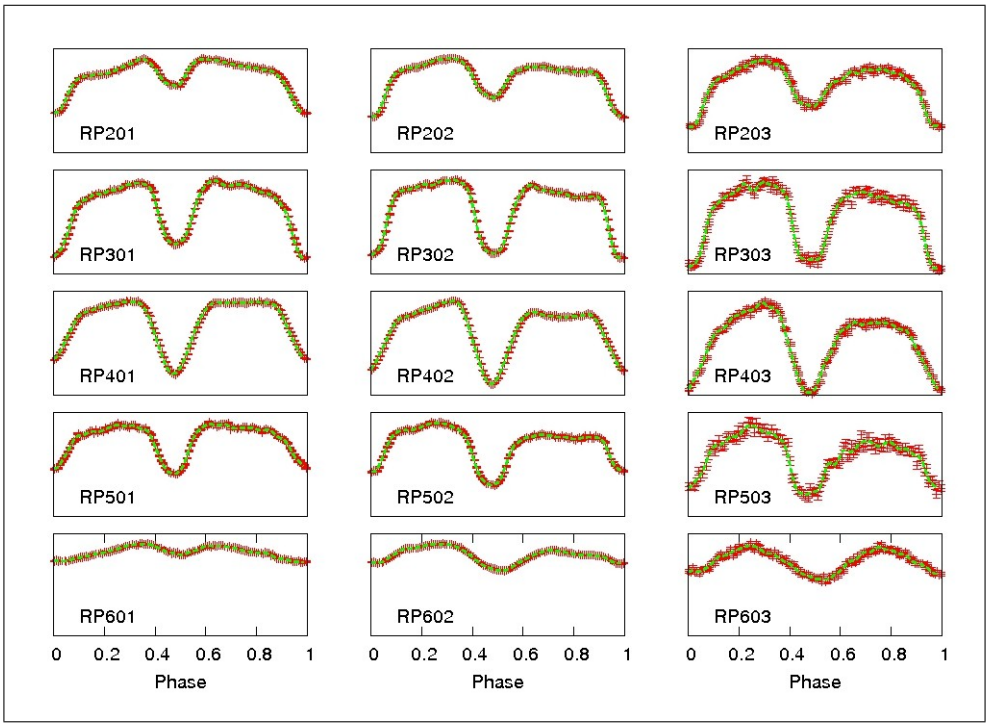

Figure 5.4: Comparison of original total pulse profiles (in green) with their Fourier sum (red data points)

After having found a suggestive number of coefficients representing all main features of the profiles we have to reduce the number of possible decompositions. First of all this number is reduced by only applying the non-negative criterion. But because there are still a huge number of possible decompositions remaining, it makes sense to put decompositions, which look similar together to one type of decomposition, and go on with just one representative for the whole group. Afterwards, we applied the no-ripples criterion by giving a certain value for the **quality function**. The

quality function is given by the value of one divided through the number of ripples U. Kraus (2007). In the script one can define all the values to determine what is defined as a ripple. For the following plots we took a value for the quality function of 0.15. The remaining possible decompositions are then splitted into two groups, one with quality factor <0.15, produces files ***.lis2**, and the other with quality factor >0.15 and output files ***.lis1**. The good solutions have quality factors of 0.15 or higher. Those good solutions can be plotted in a $\boldsymbol{\phi_1 - \Delta}$**-plot** using the gnuplot script **plot.bestdecomps** which produces an output file **bestdecomps.eps**. For the beginning, the space is parameterized with 2° x 2° boxes. We produced one plot for each observation with always four energy bands. For the following process we didn't take into account the fourth energy band with energies $> 30\,\mathrm{keV}$ due to bad statistics. To reduce the number of possible decompositions one has to apply some criteria. Because the solution of the decomposition is a geometric one, namely the location of the two poles, the solution should not depend upon the energy. So, we searched for regions in the ϕ_1-Δ-plot where we had a good solution for all three energy bands. By doing this for all the observations (see figure 5.5 for a selection of observations) and comparing all those plots by searching for regions where we had good solutions for the three energy bands, we got a number of good regions. Those regions are listed in table 5.2 and ahown in figure 5.6.

Region	ϕ_1	Δ
A	75-100	80-90
B	165-180	83-90
C	55-110	3-21
G	0-40	50-75
H	35-110	50-75
I	100-180	50-75

Table 5.2: Regions with good solutions in pulse profile decomposition

5.2.2 Studying different regions

To have a closer look at the regions which emerged from the process described above we first of all made a finer tabulation grid for the space of the interesting region. The ϕ_1-Δ parameter space is divided in boxes of 1° x 1° with kphi=20 and kdphi=20 decompositions per box.

What one gets out are decompositions in two single symmetric pulse profiles. They are plotted using gnuplot and named ***.f1_*** and ***.f2_***. We went through all those

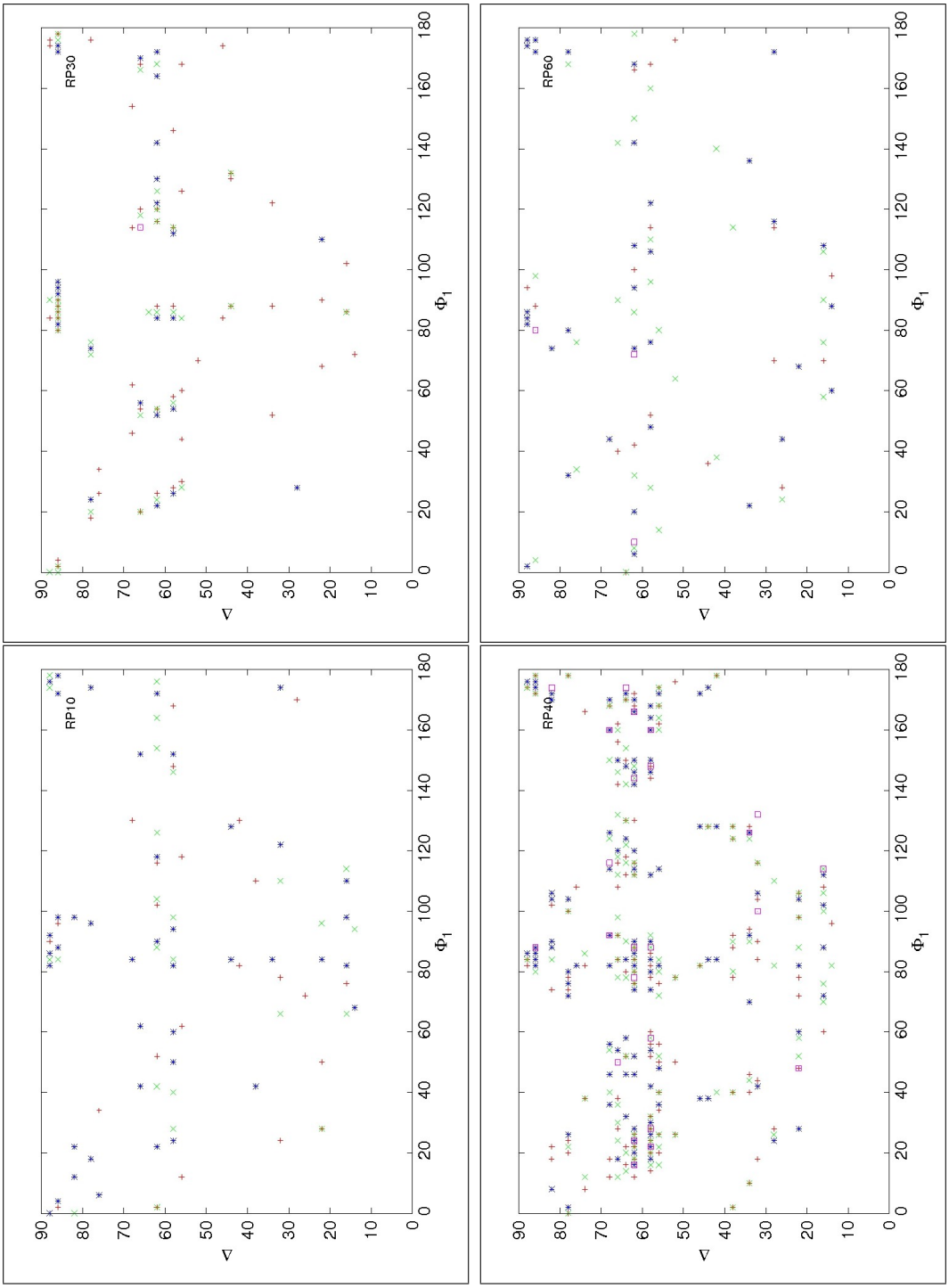

Figure 5.5: ϕ_1-Δ-parameter space with good solutions, represented in different colors (*red:* 0-7 keV, *green:* 7-20 keV, *blue:* 20-30 keV, *purple:* $>$ 30 keV), for four selected observations

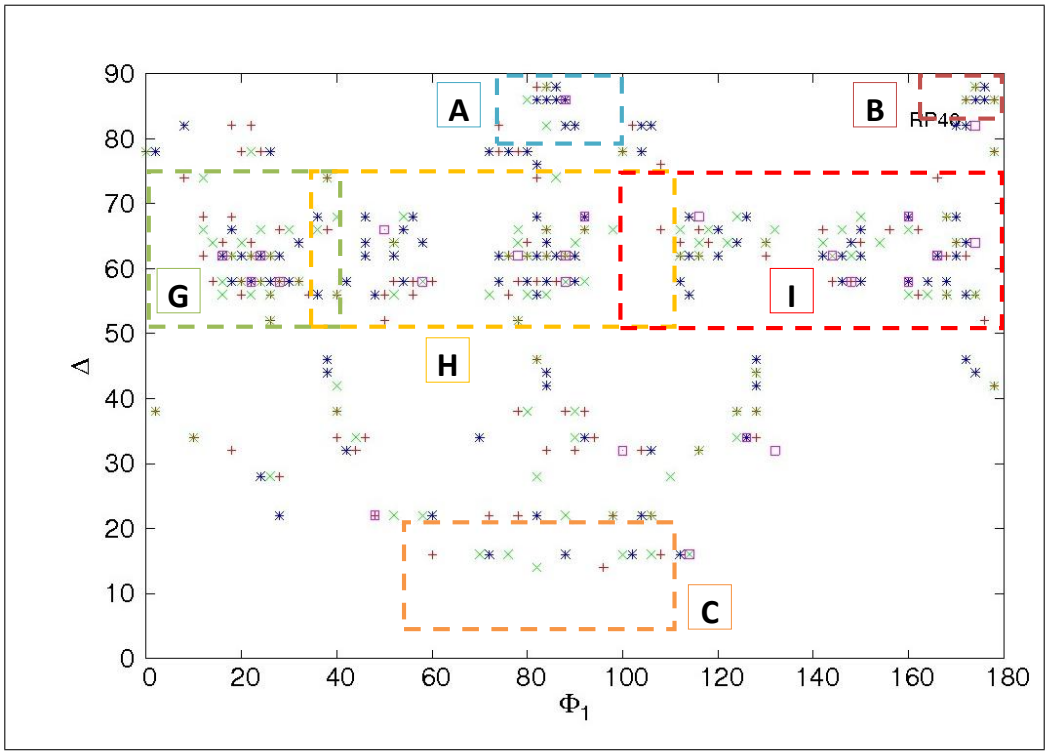

Figure 5.6: ϕ_1-Δ parameter space with marked regions for good solutions (plot from observation 90427-01-01-01)

profiles and tried to find a set of pulse profiles for a certain region by looking at the profiles and trying to find some similarities and evolution in those profiles. As an example, a possible solution for region C is shown below (figure 5.7).

After having found some nice decompositions we transformed the two single-pole pulse profiles into a section of beam pattern by writing them as function of $cos(\phi - \phi_1)$. For a better understanding we plotted the single-pole pulse profiles and their corresponding beam patterns for the first energy band in figure 5.8 for region C.

5.2.3 Total beam patterns

The production of the total beam pattern is done as described in the section *General Method* by trying to find an overlapping region and shifting one beam pattern with respect to the other with a constant value for all energy bands and observations. This process is done with the program **ueb** which calls the input file **ueb.ein**. One has to determine a value for the shift **a** and assume an angle Θ_0 between rotation axis of the neutron star and the observer and for the calculations of the light deflection one has to assume a certain value for the radius and the mass of a neutron star.

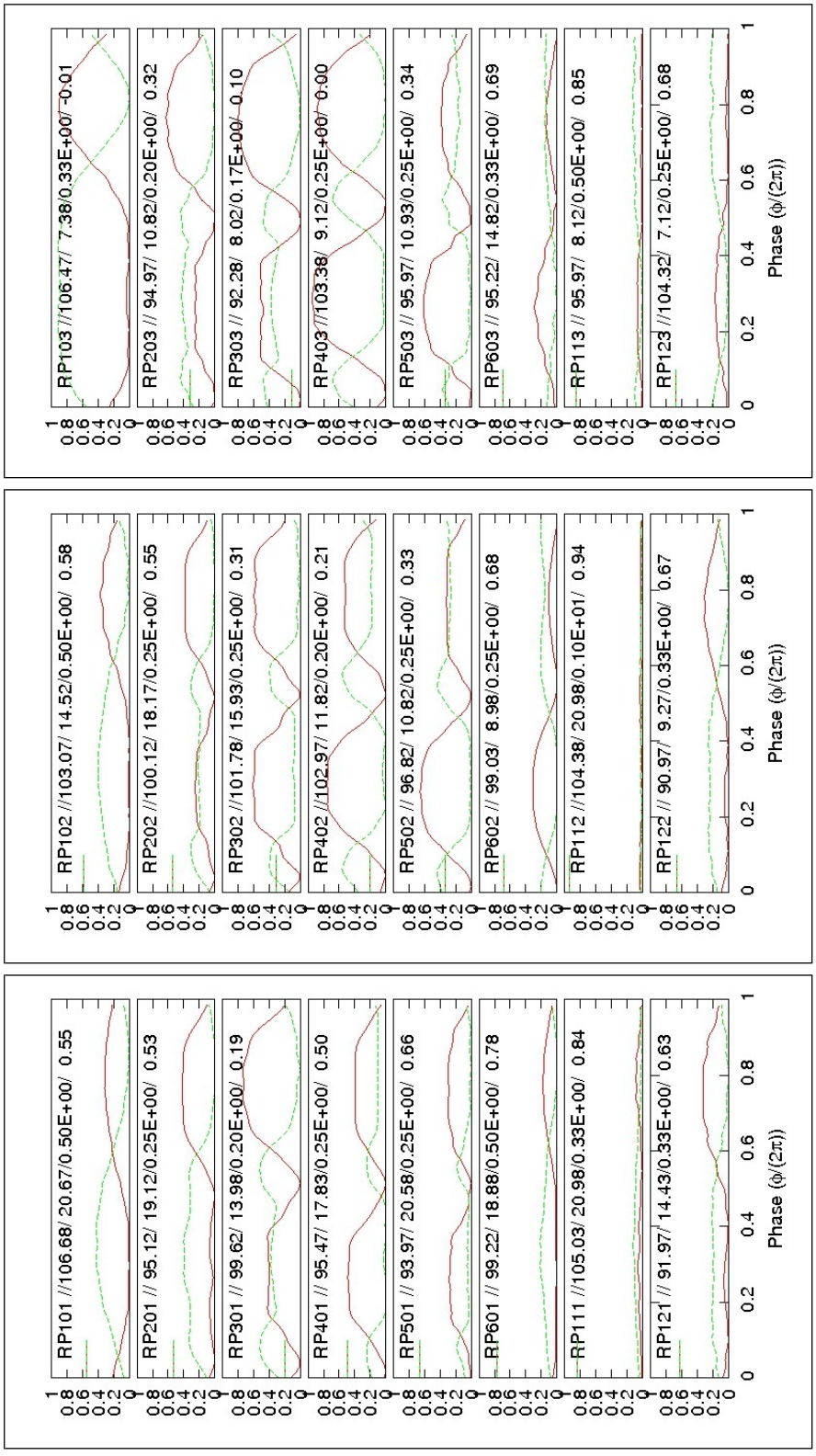

Figure 5.7: Decomposition into single-pole pulse profiles for the three energy bands: *left* 0-7 keV, *middle* 7-20 keV, *right* 20-30 keV. The single-pole pulse profiles for each band are sorted according to the start time of the corresponding observation from up to down.

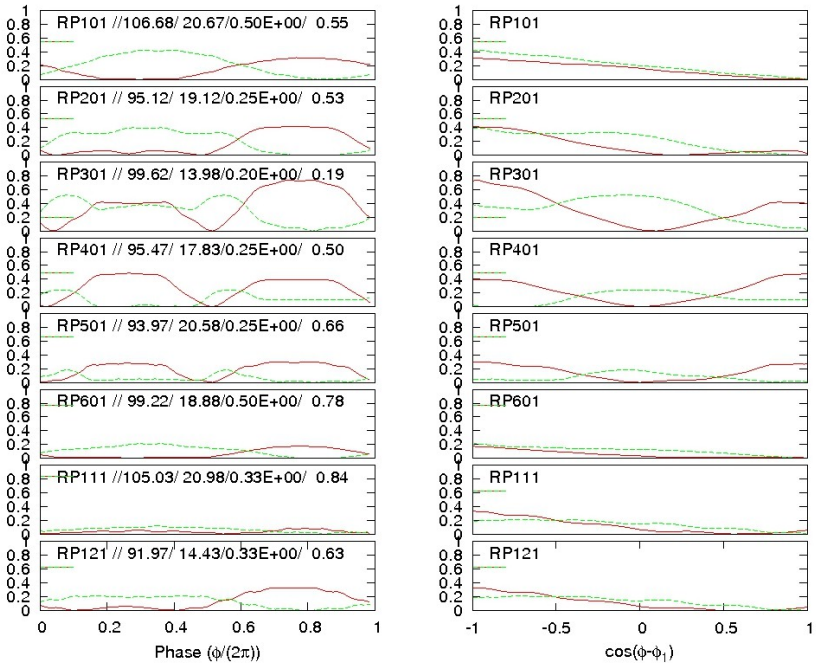

Figure 5.8: Decomposition into single-pole pulse profiles for the first energy band (0-7 keV) and the corresponding sections of beam pattern for all eight observations.

We took the following values:

- $\Theta_0 = 70°$
- $R_{\rm ns} = 10\,{\rm km}$ and $M_{\rm ns} = 1.4\,{\rm M}_\odot$ which corresponds to a Schwarzschild radius of $R_{\rm s} = 4.1\,{\rm km}$

We produced the total beam patterns for the remaining good regions A, C, G and H, to try to reject some solutions. The regions B and I were already completely rejected in the step before, as well as some types from the other regions, because they didn't represent any logical physical solution. For example, for region H, type a, the beam patterns were exactly mirror-symmetric. For region I and B the beam patterns were just one big broad peak over the whole scale and region C, type c, was a mixture of type a and b. Some rejected beam patterns, also from the step before, are shown below in figure 5.9. A list of the remaining regions, for which we produced the total pulse profiles, and the factor a for the shift is listed below.

- Region C, type a: a=+0.20 files *200_ 100*
- Region C, type b: a=-0.95 files *950_100*

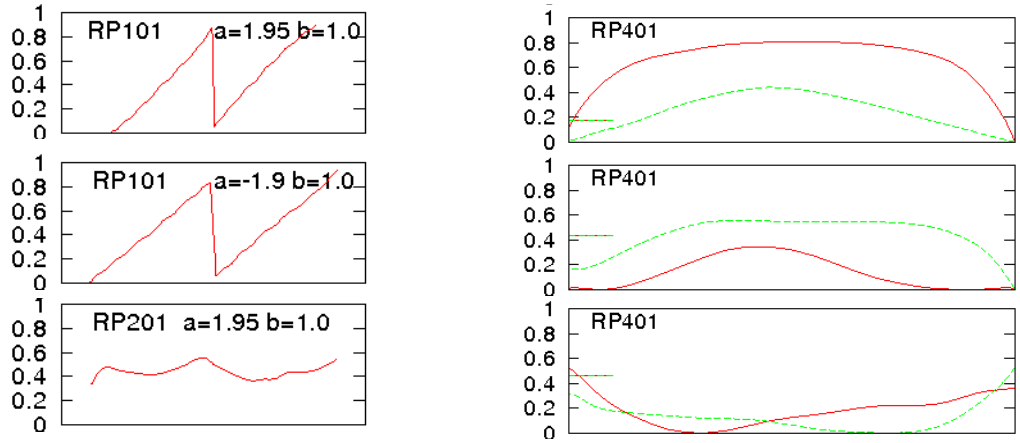

Figure 5.9: Some examples for regions which were rejected during the pulse profile decomposition process: In the two plots up left you see high jumps in the beam patterns. They represent the overlaid beam patterns of region C, type a, for different shift factors. In the plot for region A below, the beam patterns are simply put one behind the other and look very flat without many features. In the figures on the right, there are shown the broad big peaks of region B on top and region I beneath and the mirror-symmetric profile of region H at the bottom.

- Region C, type d: a=+1.00 files *100_100*
- Region A : a=+1.65 files *165_100*
- Region H : a=+1.80 and a=-0.30 files *180_ 100* and *300_100*
- Region G: a=-1.25 files *125_100*

Because there are so many good regions remaining, we decomposed some additional data for the time of the end of the outburst. Afterwards, some decompositions and regions were rejected.

We rejected the beam patterns of type d in region C because the beam patterns appeared very similar to those of region C, type b, and we decided to go on with just one type of decomposition for one region. Likewise, the beam patterns of region H and G looked pretty similar, therefore we just took one of them to go on, namely region G. The beam patterns for region A were also sorted out. First of all, they were not really overlaid but only put one behind the other one, which is nearly always possible. And secondly, the beam patterns appeared very flat, which means they didn't show many features which could be identified as some kind of emission. For the beam patterns of type a in region C we observed discontinuities, which doesn't make any physical sense. They were rejected as well.

The overlaid beam patterns for region C (shift a=-0.95) are shown in figure 5.12 and the total beam pattern as function of the observation angle $\Theta_{\rm obs}$, for which we have

a *plus* and a *minus* solution, can be seen in figure 5.13 and 5.14. All of those beam patterns haven't yet taken into account relativistic light deflection. If we calculate the effects of relativistic light deflection we get the beam patterns as function of the intrinsic observation angle (see figure 5.15 and 5.16).

The same was done for the second good region, namely region G (shift a=-1.25). The different beam patterns for this region can be seen below (figures 5.17, 5.18, 5.19 and the intrinsic beam patterns in 5.20and 5.21).

5.3 Geometry of the emission region

A summary of the geometric solution, namely the position of the two magnetic poles for region C, as well as for region G is listed below (see table 5.3).

The results of the pulse profile decomposition method strongly depend on the assumed observation angle Θ_0. One can plot the solution for the location of two magnetic poles as a function of the observation angle. We attached a plot for the region, which appears more meaningful to us below, namely for region C (see figure 5.10). The reason, why we select exactly this region is explained in the next chapter. The geometry plots of region G are shown in the appendix (see figure B.1 and B.2).

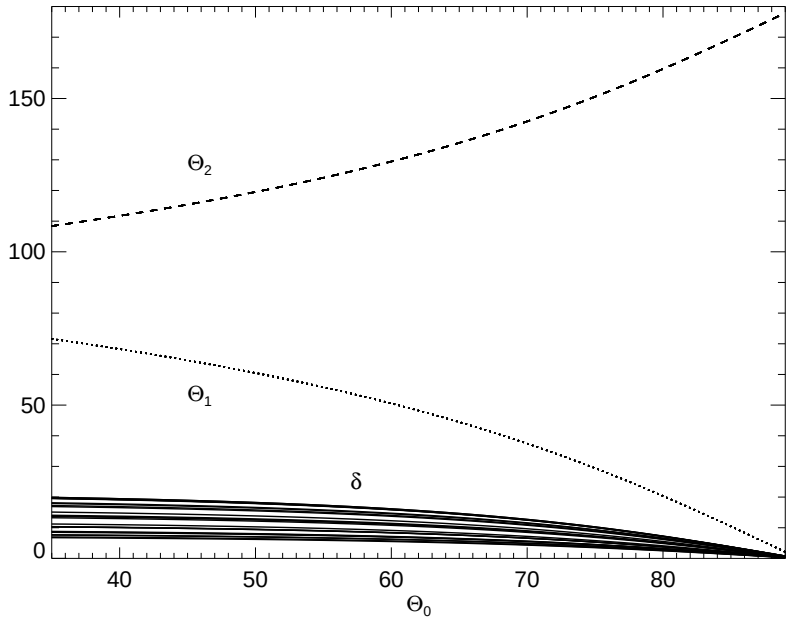

Figure 5.10: Geometric solution for region C: Position of the two magnetic poles Θ_1 and Θ_2 as a function of the observation angle Θ_0 and the shift δ from the antipodal position for all eight observations.

	region C	region G
ϕ_1	100°	12°
Θ_1	38°	30°
ϕ_2	295°	260°
Θ_2	142°	142°
Δ	15°	68°
a	−0.95	−1.25

Table 5.3: Geometric solution for region C and G for an assumed observation angle of $\Theta_0 = 70°$

And finally, to give you a better idea of the geometric solution for region C, we made a plot of the geometry of the neutron star with the position of the two magnetic poles marked (figure 5.11).

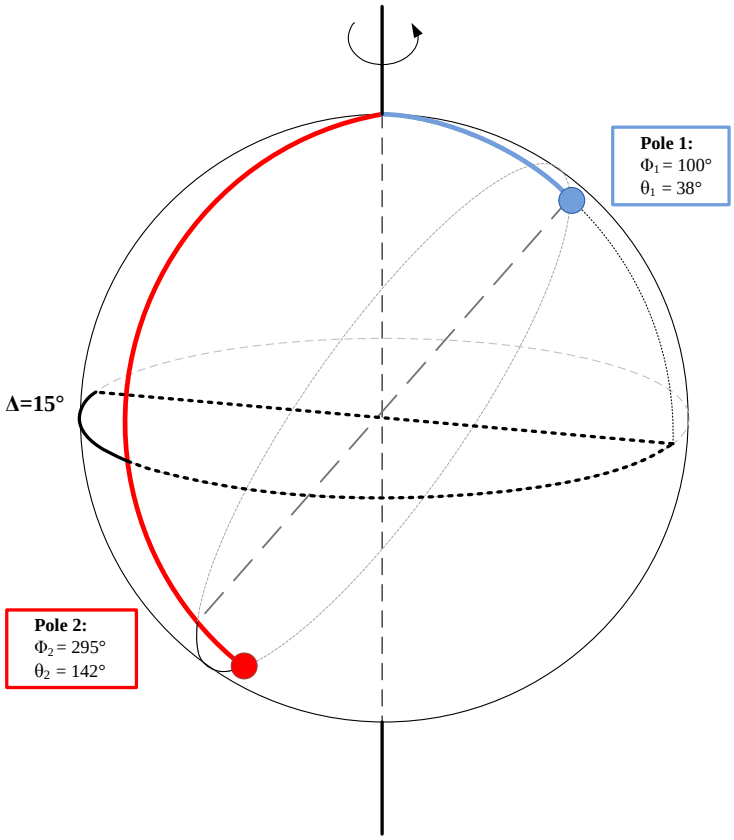

Figure 5.11: Position of the two magnetic poles for the solution of region C and for an observation angle of $\Theta_{obs} = 70°$

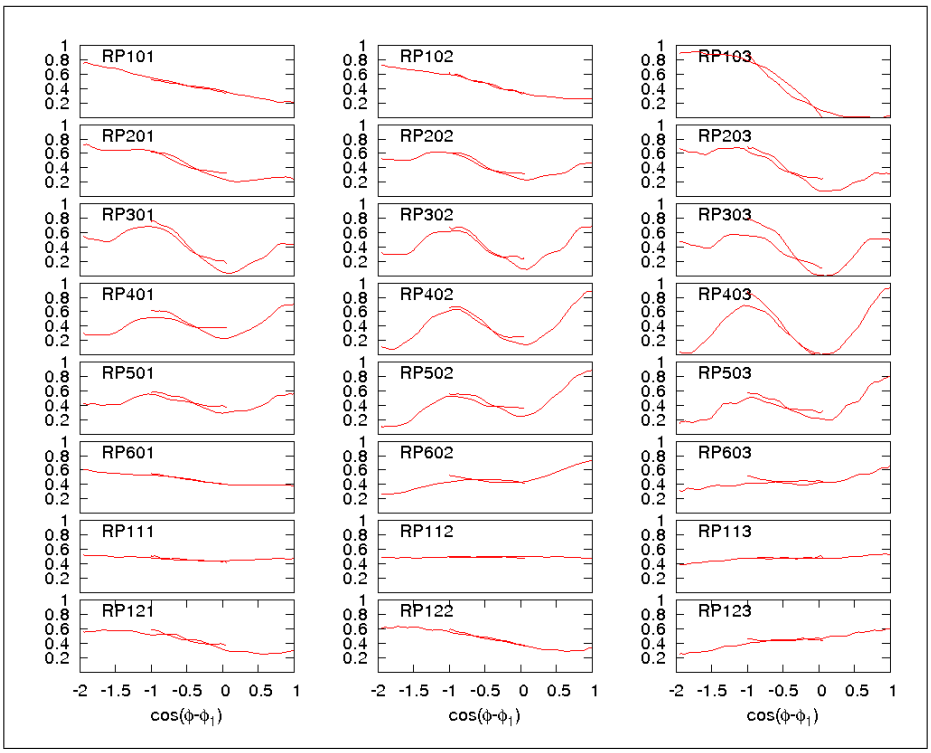

Figure 5.12: Overlaid beam patterns for region C

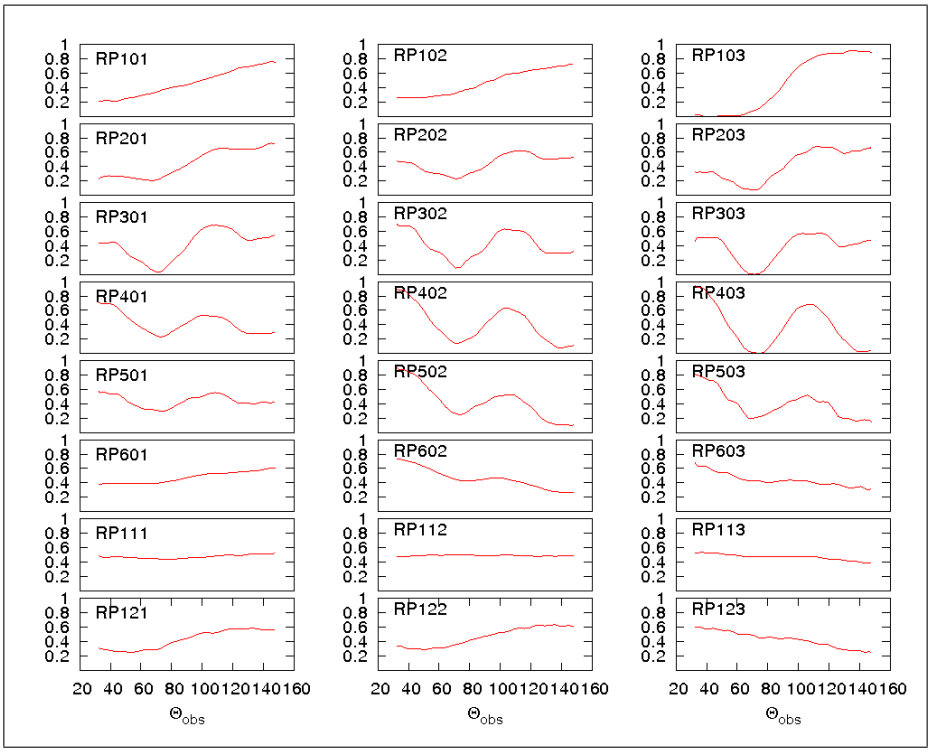

Figure 5.13: *Plus* solution for the beam patterns as function of observation angle Θ_{obs}

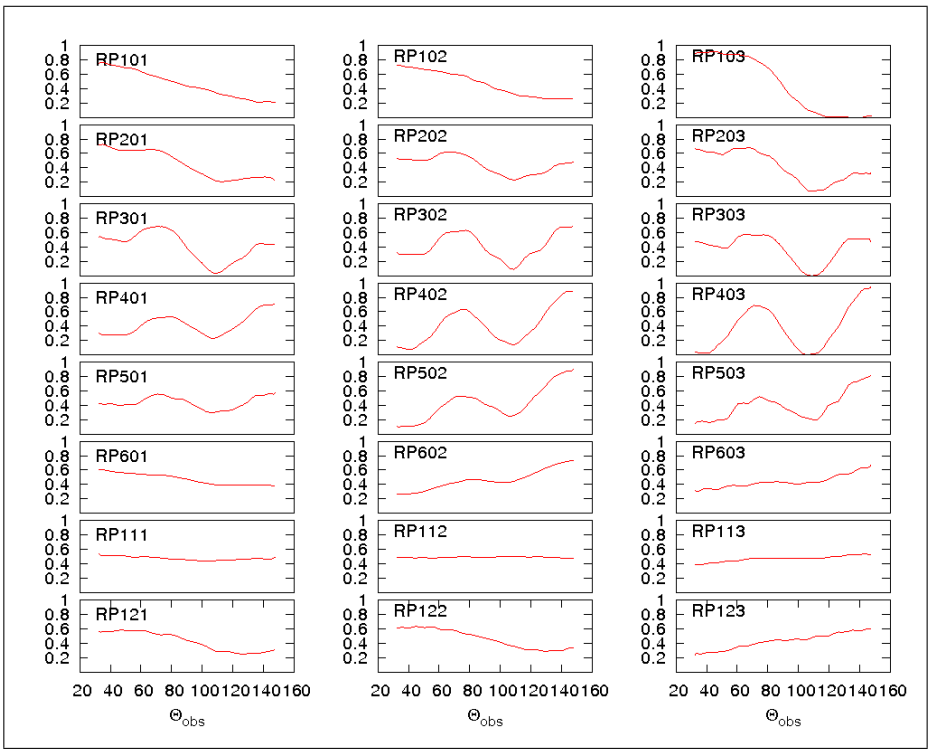

Figure 5.14: *Minus* solution for the beam patterns as function of observation angle $\Theta_{\rm obs}$

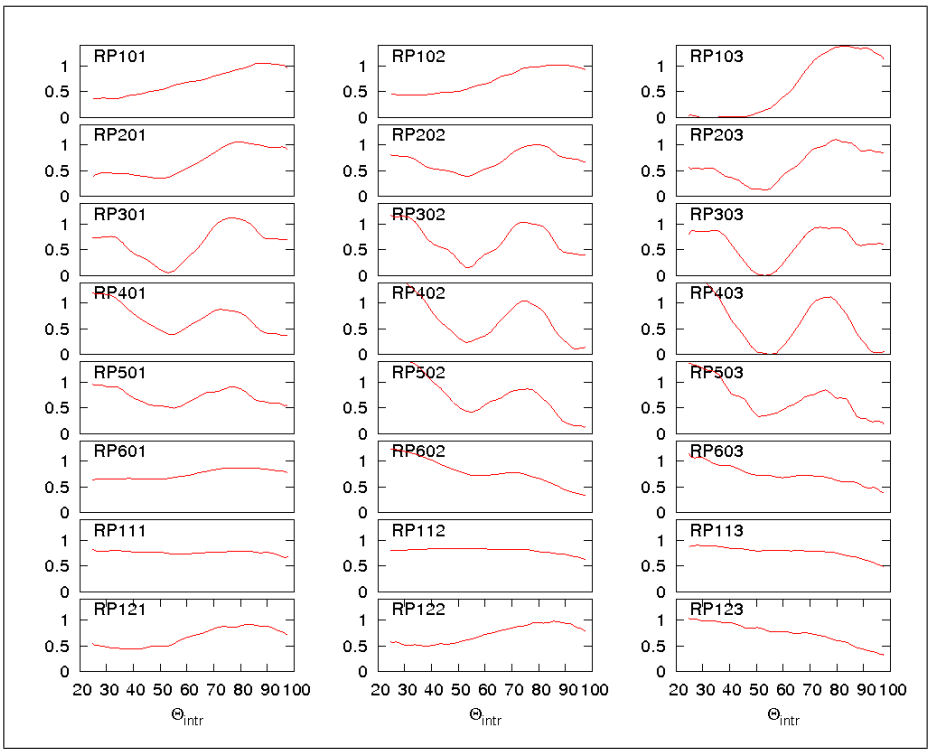

Figure 5.15: Intrinsic beam patterns for the *plus* solution as function of intrinsic emission angle $\Theta_{\rm intr}$

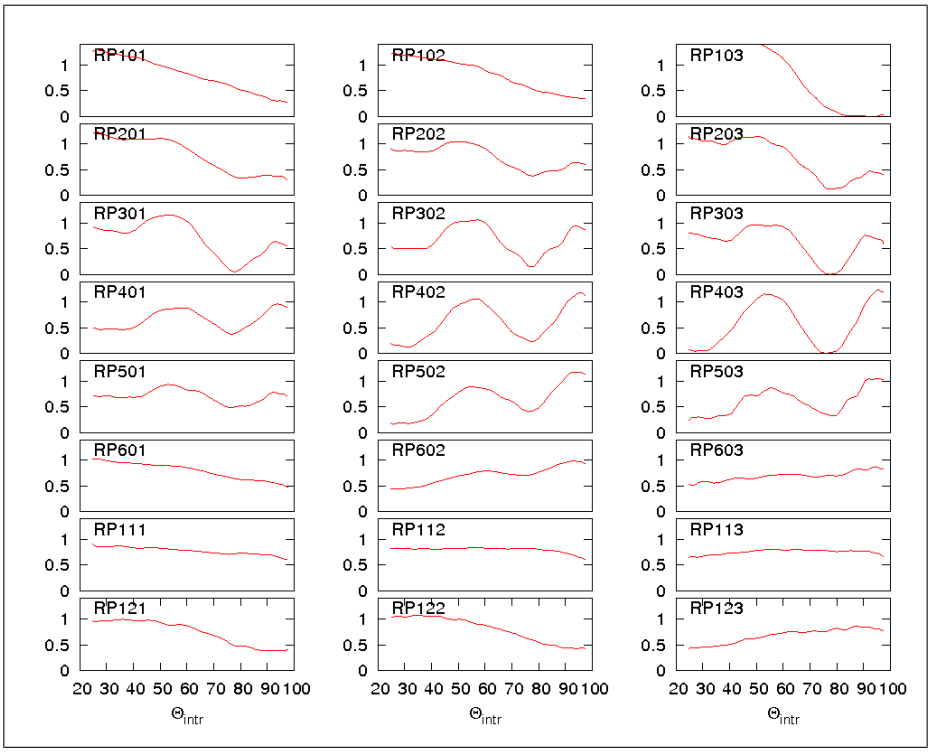

Figure 5.16: Intrinsic beam patterns for the *minus* solution as function of intrinsic emission angle Θ_{intr}

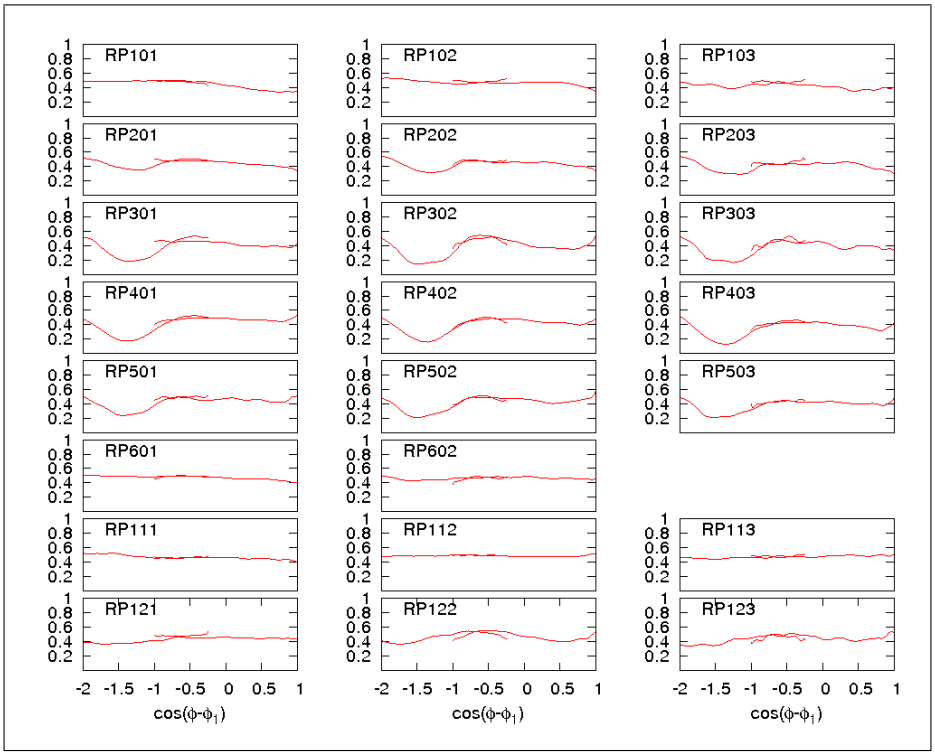

Figure 5.17: Overlaid beam patterns for region G

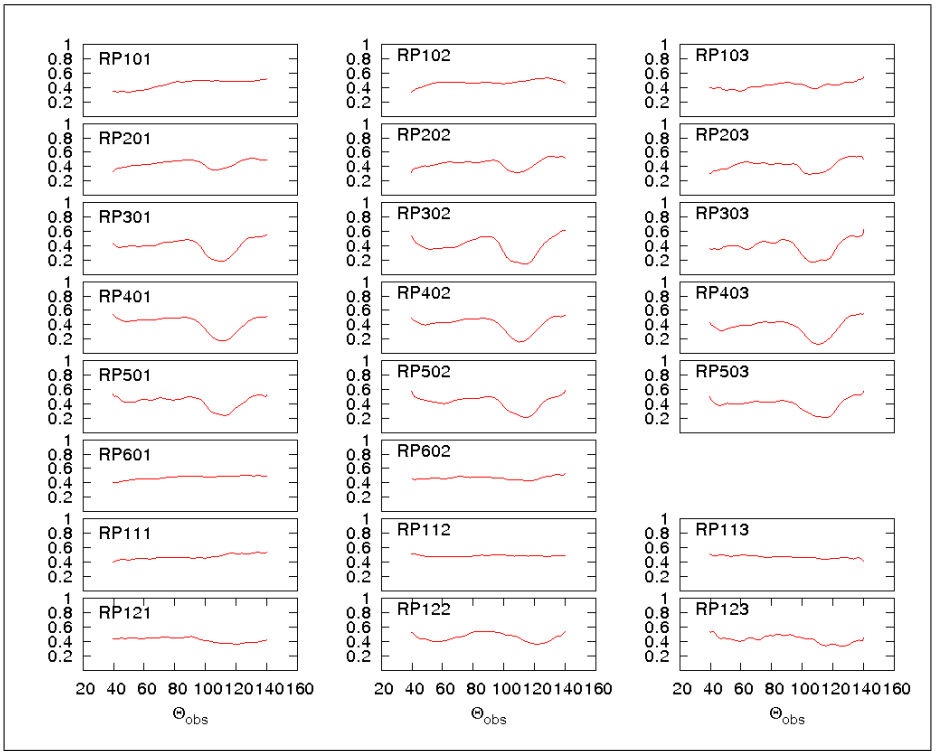

Figure 5.18: *Plus* solution for the beam patterns as function of observation angle $\Theta_{\rm obs}$

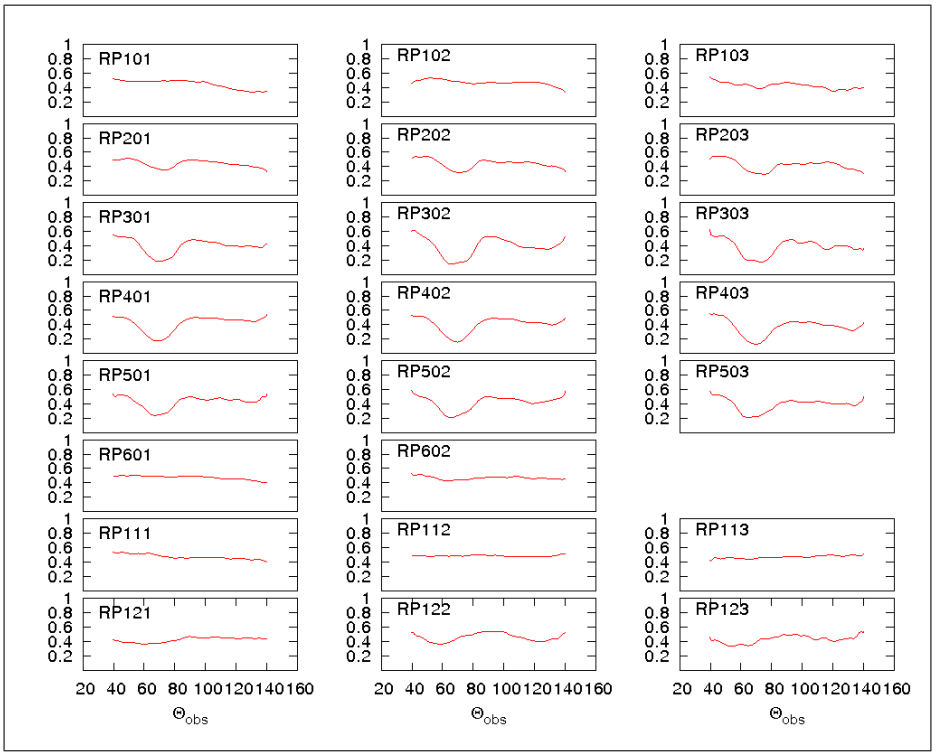

Figure 5.19: *Minus* solution for the beam patterns as function of observation angle $\Theta_{\rm obs}$

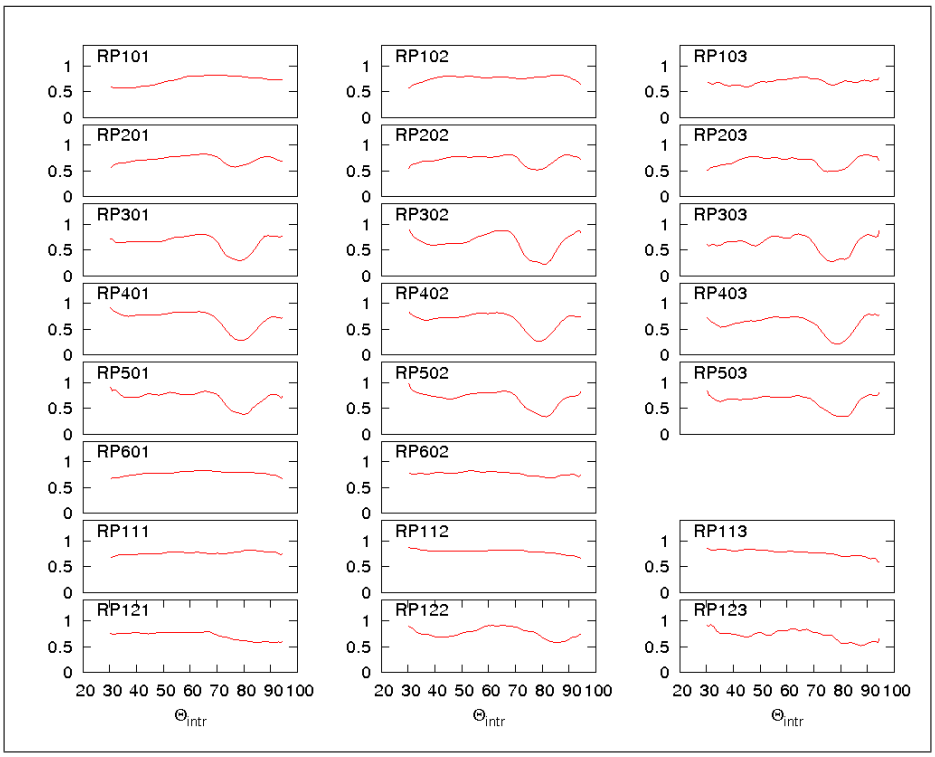

Figure 5.20: Intrinsic beam patterns for the *plus* solution as function of intrinsic emission angle Θ_{intr}

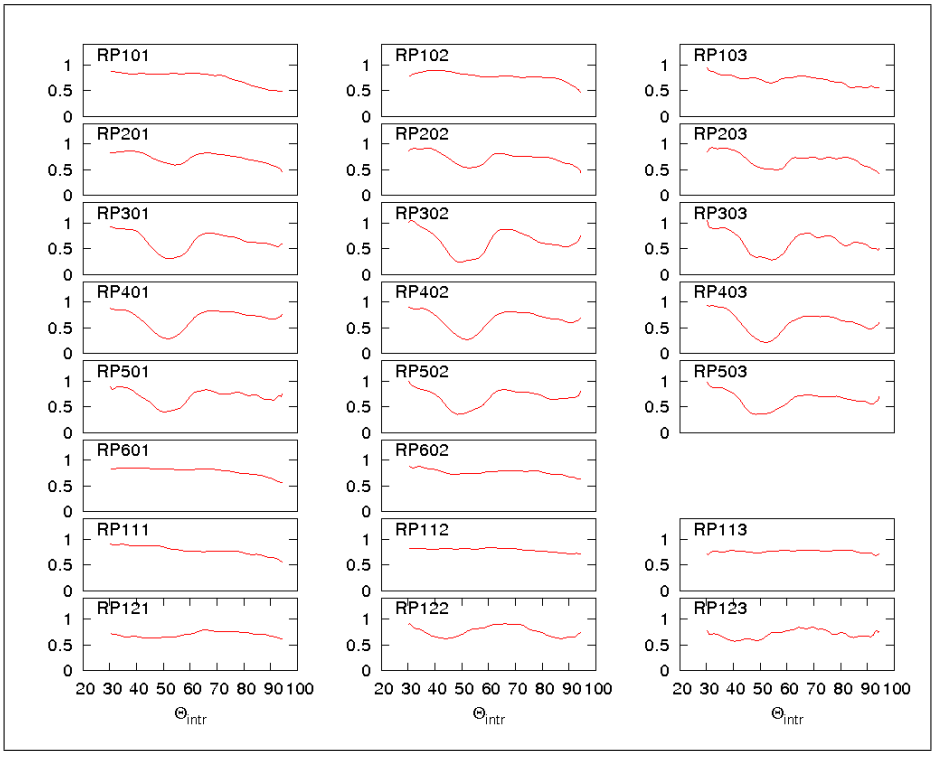

Figure 5.21: Intrinsic beam patterns for the *minus* solution as function of intrinsic emission angle Θ_{intr}

Chapter 6

Interpretation of the beam patterns

In the chapter *Decomposition*, we described the general method of pulse profile decomposition as well as the solutions we obtained while applying this method. What we got were two possible solutions, a *plus* and a *minus* solution, for each region due to the ambiguous assignment of the symmetry points. What remains is the interpretation of the beam patterns. From the set of solutions we got from the decomposition method, we should first of all determine the physically most plausible solution.

6.1 Starting with region C

For region C, we think the *minus* solution for the beam patterns makes more sense. The reason why we take this solution will become clear when having a look at the interpretation of the beam patterns in the following sections. A plot of the whole spectrum of beam patterns is again shown in figure 6.1 on page 72.

Looking at the plot, one can see an evident evolution in the beam patterns. For low luminosities, the main emission takes place at small emission angles. While the source is getting brighter, we get additional components at emission angles of around $\Theta_{\mathrm{obs}} = 50-90^{\circ}$ and at angles above $\Theta_{\mathrm{obs}} = 110^{\circ}$. Just as well, a distinctive minimum arises at about $\Theta_{\mathrm{obs}} = 45^{\circ}$ and at $\Theta_{\mathrm{obs}} = 110^{\circ}$. For decreasing source luminosity, the beam patterns get similar to those from the beginning of the outburst.

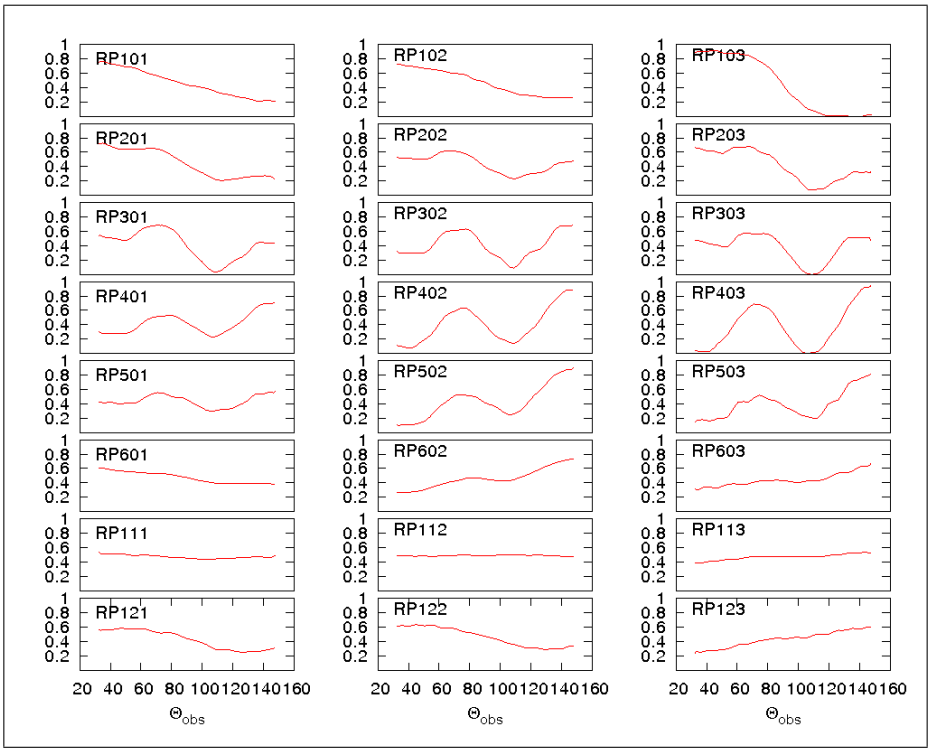

Figure 6.1: Beam patterns for the *minus* solution of region C as function of the observed emission angle Θ_{obs}

6.2 Interpretation: Hollow column

One idea to interpret the structure and evolution of the beam patterns is the concept of a **hollow column** as described in Kraus (2001). The main idea is that the emission at small angles is related to the emission and scattering processes from inside the hollow column. The first minimum (in our case at about $\Theta_{\mathrm{obs}} = 45°$) may be assigned to the column wall, while emission from the outside of the hollow column is responsible for the arising main peak ($\Theta_{\mathrm{obs}} = 50 - 90°$). This contribution is getting less with increasing angles until reaching a second peak (above $\Theta_{\mathrm{obs}} = 110°$), which possibly originates from scattering of the halo and column radiation in the upper accretion stream. A schematic view of the geometry of such a system may be seen in figure 6.2. We will devote further discussion on the detailed process of emission by a hollow column in the following.

6.2.1 Hollow column model

How the accretion process on a compact object really takes place remains an unsolved problem. However, from the beam patterns obtained and from other examples (see e.g. Blum & Kraus, 2000; Kraus et al., 1996), we can try to conclude a little bit more

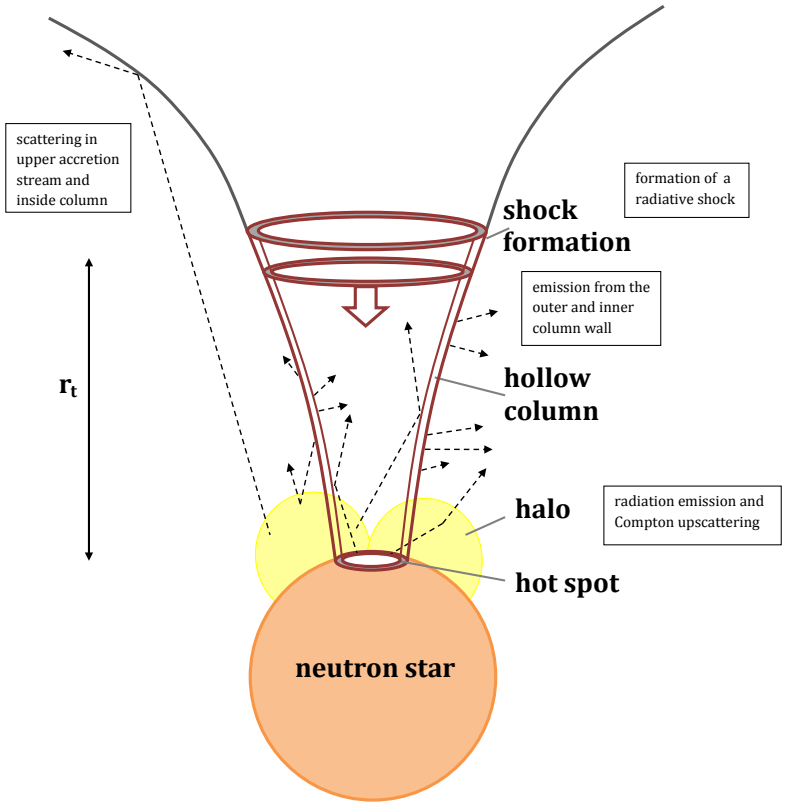

Figure 6.2: Schematic view of the hollow column accretion model

about the real structure of the accretion funnel. The model of a hollow accretion column can explain our results from the analysis on V0332+53, as well as the beam patterns of Cen X-3 relatively good. The following discussion is mainly based on Kraus (2001).

For high-luminosity sources the matter is decelerated above the stellar surface in a radiative shock, that separates a region of freely falling plasma above from a settling region of nearly stagnate plasma below. We have

$$L > L_* = \frac{\alpha}{4} L_{\mathrm{edd}} \frac{\sigma_{\mathrm{T}}}{\sigma_{\mathrm{S}}} \tag{6.1}$$

with L_{edd}: Eddington luminosity; σ_{T}: Thomson cross section; σ_{S}: magnetic scattering cross section; α: half-opening angle at base of funnel.

The radiation mainly originates from the deceleration and settling regions and escapes from the sides of the column. What we expect is a thin-walled hollow funnel which emits radiation from the inner and the outer walls of the optically thick settling

mound below the shock. For small observation angles, while looking nearly straight onto the magnetic poles, one can view directly into the hollow column. Considering the effects of scattering, the flux should slightly decrease for small angles, while scattering in the antipodal accretion stream should affect the flux at large angles (Kraus et al., 2003). For high luminosities $L > L_*$ and considering the nonmagnetic Thomson cross section σ_{T}, the free-fall region is marginally optically thick. However, for increasing source luminosity the free-fall region will more and more get optically thick. Taking into account magnetic scattering due to the star's intense magnetic field, the cross section equates roughly the Thomson cross section for frequencies near the cyclotron frequency $\omega_{\mathrm{c}} = \frac{eB}{m_{\mathrm{e}}}$ but is reduced for lower frequency radiation. Thus, the free-fall region gets optically thin to low-frequency radiation. Consequently, the radiation from the inner column wall should make an important contribution to the beam patterns at low frequencies.

Apart from the emission by the column we have also emission from the halo. The halo emission comes from an area that is larger and cooler than the wall of the column and therefore dominates at lower energies (Kraus et al., 2003). The beam patterns of the halo are even more energy dependent and without any interaction they would simply be a broad pencil beam (Kraus et al., 2003). However, the flux is reduced by shadowing and, as well, for example by scattering in the free-fall stream, as mentioned above. This affects mainly the beam patterns at higher energies, because the scattering cross section in a strong magnetic field increases with the photon energy for energies below the cyclotron energy (Kraus et al., 2003). Scattering in the upper accretion stream is not that effective due to the smaller plasma density, but nevertheless, about 5-15% of the halo radiation is scattered, mostly downwards, in the upper accretion stream (Kraus et al., 2003).

Finally, the combined beam patterns of the halo and the accretion column are also strongly energy dependent. The hollow column accounts for additional structures, mainly at low energies due to the smaller scattering optical depth across the accretion funnel (Kraus et al., 2003), while the relative importance of the halo is related to the emission model. For isotropic emission and also for beamed emission, the contribution from the halo first goes down with increasing energy due to the lower temperature of the halo with respect to the one of the column wall. However, for beamed emission, the halo importance increases again for higher energies. This can be explained by the fact, that the direct column emission is decreasing more than the flux of the halo, because the column radiation is stronger beamed downwards due to the high velocity of accretion and a growing percentage of the flux is intercepted by the neutron star (Kraus et al., 2003).

The energy dependence of the beam patterns and pulse profiles arises from (Kraus et al., 2003)

- a local column emission pattern that is energy dependent. The column beam pattern, but not the one of the halo, is affected by the effects of downwards beaming.
- a different spectrum from radiation that is reemitted by the neutron star's surface. The reemitted spectrum is different from the one of the column and therefore we get different spectra from the column and the halo.
- an energy dependent magnetic scattering in the free-fall stream. This determines the shape of the halo beam pattern at small viewing angles.

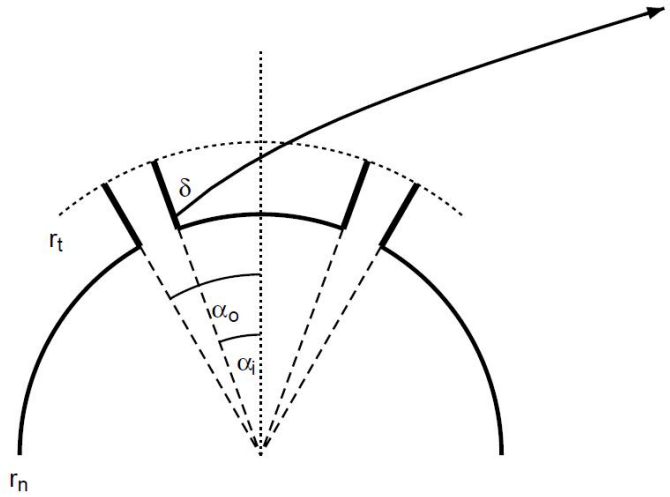

Figure 6.3: Hollow cone model with α_{o}: outer half-opening angle, α_{i}: inner half-opening angle, δ: angle between direction of emission and radial direction (Kraus, 2001).

In the phenomenological model of a hollow column, there is a radial hollow cone, representing the shock and extending up to a radial coordinate r_{t}, where the radiative shock is formed (see figure 6.3). Above this point, the free-fall region is optically thin to free-free absorption and to scattering, whereas below, the column is optically thick. In this model, the upper part shall not radiate and the neutron star rotates slowly, so that we can apply the Schwarzschild metric to calculate the way of the photons.

Having a look at the beam patterns, the part before the minimum can be assigned to the inside component of the hollow column while the minimum itself marks the point

when the observer looks directly onto the wall. This point is a geometric solution and is mainly related to the compactness of the neutron star. The maximum flux depends on the cone height and width, but also on the compactness of the neutron star. For the radiation that originates from the outer wall of the column, the position of the flux maximum and the point, at which the cone disappears behind the star, depends on the compactness of the neutron star and therefore on the ratio $r_{\rm n}/r_{\rm s}$. For a very compact neutron star the outer wall may even be visible from all directions due to light deflection around the neutron star. And, as briefly discussed before, one can also include beamed emission, which mainly influences the width of the flux maximum, but not the point of the minimum flux.

6.2.2 Application to V0332+53

The beam patterns of V0332+53 may be interpreted in terms of a **hollow column** or in terms of an optically thick **filled column**. At low luminosities, the main emission originates from small emission angles $\Theta_{\rm obs}$ and decreases for higher values. For small angles one looks directly on the magnetic pole and therefore, we think that this emission can mainly be assigned to the pencil beam emission coming from the hot spot or the accretion mound. That's the reason why we picked the minus solution and not the opponent plus solution. For higher luminosities, we get contributions from other parts. While comparing the different beam patterns one always has to keep in mind that the pulse profiles are normalized and therefore, the emission from the hot spot and accretion mound is still present for higher luminosities, but is simply much smaller than the emission from the arising new components. If we now have a look at the beam pattern at the maximum of the outburst we can clearly see two peaks. One at about $\Theta_{\rm obs} = 50 - 90^\circ$ and one for values above $\Theta_{\rm obs} = 110^\circ$. Also visible are striking minima at values of about $\Theta_{\rm obs} = 45^\circ$ and $\Theta_{\rm obs} = 110^\circ$. It is mentionable that those minima do not move with the energy and/or the luminosity. The location of the zero point should be a geometric result and therefore not depend upon those values, what we can confirm by looking at our beam patterns.

The flux at small angles (up to $\Theta_{\rm obs} = 110^\circ$) can be assigned to the emission from the halo. For small luminosities one can only see this emission but for increasing luminosities there arises a minimum at about $\Theta_{\rm obs} = 45^\circ$ which might also suggest a hollow column. This minimum is present due to the fact that the observer is looking directly onto the column wall and probably also because the accretion stream gets in the line of sight of the observer and covers the halo. For higher luminosities the accretion stream gets denser and the shock height increases, therefore it sheets a bigger area of the halo. Thus, the minimum of the accretion column becomes more significant. Just as well, the minimum gets stronger for higher energies, which fits

quiet well to the idea, that lower energy radiation is not as much scattered as higher energetic radiation. Even though the plots indicate some emission for angles smaller than the minimum, it is difficult to say if the flux really goes up again and therefore shows emission from inside the hollow column. Also because the angular scale is simply limited to values of about $\Theta_{\text{obs}} = 30°$ due to the geometry of the system.

Whether we take the hollow column model or the idea of an optically thick filled column with no radiation escaping from inside the column walls, in both cases it still remains to explain the rising component above $\Theta_{\text{obs}} = 110°$. Our idea, which fits to the ideas described in the papers by Ute Kraus, is that this emission originates from the scattering of the radiation from the halo and the accretion column in the upper accretion stream. We already described this process while explaining the model of a hollow column and now just want to mention that this theory can be confirmed looking at our our beam patterns.

6.2.3 Comparison to Cen X-3 and Her X-1

Cen X-3

According to Ute Kraus et al. (Kraus et al., 1996), Cen X-3 has got energy-dependent asymmetric pulse profiles, which are thought to originate from a distorted magnetic field. Applying the pulse profile decomposition method to Cen X-3 results in a shift of the magnetic poles of 10° from the antipodal position. The beam patterns (see figure 6.4) look very similar to the ones we obtained from our analysis of V0332+53.

The results of the analysis prove, that even such a small shift from an antipodal pole position can lead to an asymmetry, as it is observed in the pulse profiles. It is also shown that the beam patterns of the two poles of Cen X-3 are very likely to be identical, which means that there should be two equal emission regions. The features, which are thought to evolve by applying the hollow column model are clearly visible for Cen X-3.

There are two components, which are well separated by a minimum at an angle of about $\Theta \approx 105°$. They are assigned to the emission from the inside, respectively from the outside of a hollow column. All the features described in the section *Hollow column model* are represented in the beam patterns of Cen X-3. This suggests that the model of a hollow column may be appropriate to explain the accretion process of this source.

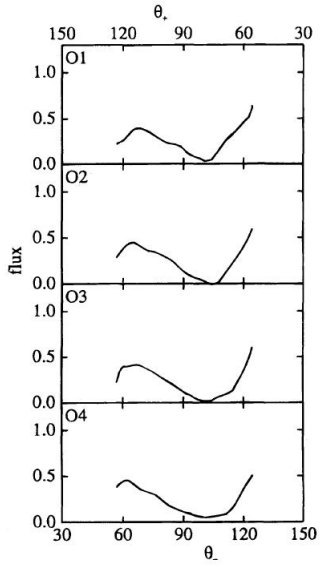

Figure 6.4: Beam patterns of Cen X-3 as a function of the observation angle Θ_+, respectively Θ_-, with one axis for each solution. The four plots correspond to four energy ranges, namely from 1.0-2.3 keV, 2.3-8.3 keV, 8.3-12.5 keV and 12.5-25.0 keV (Kraus et al., 1996).

Her X-1

The method of pulse profile decomposition was also applied to the well-known X-ray pulsar Her X-1 and is described in the paper *Geometry and beam pattern of Hercules X-1* by S. Blum and U. Kraus (Blum & Kraus, 2000). The results of their analysis are similar to those of Cen X-3. The pulse profiles and beam patterns of Her X-1 are compatible with the idea of a symmetric emission of each single pole and with the concept, that a distorted magnetic dipole field is responsible for the asymmetric pulse profiles. Some beam patterns of Her X-1 are shown in figure 6.5.

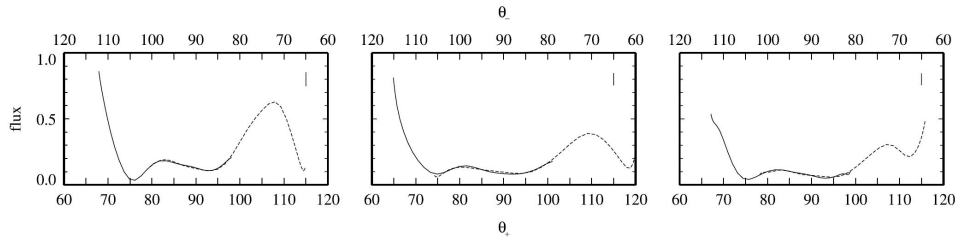

Figure 6.5: Beam patterns of Her X-1 as a function of the observation angle Θ_+, respectively Θ_-, with one axis for each solution. The three plots correspond to three energy ranges, namely from 6.0-8.3 keV, 10.0-13.0 keV and 20.0-23.0 keV (Blum & Kraus, 2000).

However, it is still possible that the asymmetry in the pulse profiles results from an asymmetric beam pattern. But considering a small asymmetry in the beam patterns, the results Blum and Kraus got from the decomposition are still thought to be all right or at least an approximation to the azimuthally averaged beam patterns. The beam patterns, which they obtained for various observations, all have the same basic structure and energy dependence, only the relative sizes of the different features are varying. The main features are thought to be a pencil- respectively a fan-beam, with the contribution of the fan-beam going down with the energy. They also mention that the radiation, which escapes in the direction of the magnetic axis, is blocked as a result of electron cyclotron absorption. Summaryzing the analysis on Her X-1, all data is compatible with the assumption of a slightly distorted magnetic dipole field as unique cause of the asymmetry of the observed pulse profiles. Further, the analysis provides evidence that the emission from both poles is equal. They determined an angle of 20° between the rotation axis and the local magnetic axis, as well as an offset of $\delta < 5°$ for each pole from the antipodal position of the opposite pole. Furthermore, the beam patterns show structures that can be interpreted as pencil- and fan-beam configurations.

6.3 Region G

So far, we only reported on the solution of region C. Now, we also want to take a look at the second possible solution, that of region G. The interpretation of the beam patterns in this region is maybe not as straightforward as before, but anyway, there are no reasons to discard this solution. For region G we favor the *plus* solution, for which the beam patterns are shown in figure 6.6.

The beam patterns show a clear development with changing source luminosity. Because the beam patterns are only scaled relatively it is possible, that for low luminosities, the beam patterns are very flat without many features. For increasing source luminosity we get some additional components. There is also a distinctive minimum at around $\Theta_{\mathrm{obs}} = 110°$ and a hint of a minimum at about $\Theta_{\mathrm{obs}} = 40 - 50°$. The beam patterns could be explained similar to the beam patterns of region C before. There is some emission for low luminosities and for higher luminosities there arise some additional components. But the beam patterns are notable different to those of Her X-1, Cen X-3 and also to the ones of region C. The main difference is that the shape of the beam patterns for low angles varies. The minimum, possibly representing the column wall, which was detected for the other sources is not existent for region G or there is only a hint of it. Just as well, the structure of the beam pattern between the two minima looks different from the beam patterns of the other

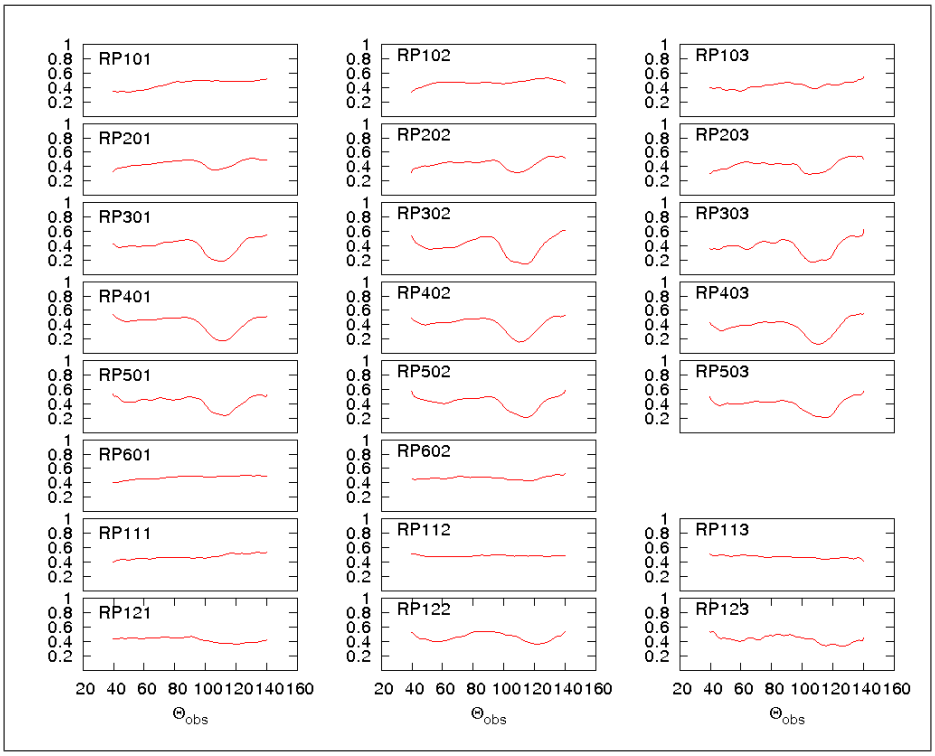

Figure 6.6: Beam patterns for the *plus* solution of region G as function of the observed emission angle Θ_{obs}

sources.

Chapter 7

Summary and outlook

In this work we have first performed the timing analysis of the X-ray binary transient pulsar V0332+53, observed by RXTE and Integral in the outburst in 2004/2005. After having obtained a series of profiles for different energy bands and different luminosities, we applied the pulse profile decomposition method as described in the chapter *Decomposition*. A key goal of this analysis was to understand the structure of the dipole field and in particular the position of the two magnetic poles of the neutron star companion. To apply the method we made two fundamental assumptions: the asymmetric pulse profiles originate from a distorted magnetic dipole field and each of the two emission regions is symmetric and equal to the other one. We then obtained several sets of single-pole pulse profiles which were overlaid and transformed into beam patterns. Two regions with good decompositions emerged after applying several criteria: region C with magnetic poles at $\phi_1 = 100°$, $\Theta_1 = 38°$, $\phi_2 = 295°$, $\Theta_2 = 142°$ and region G with $\phi_1 = 12°$, $\Theta_1 = 30°$, $\phi_2 = 260°$, $\Theta_2 = 142°$. We also calculated the intrinsic beam patterns, assuming the canonical values of mass and radius for the neutron star. As we show in our thesis, these intrinsic beam patterns strongly depend on the assumed observation angle Θ_0.

From the two solutions we discussed in details the one labeled as region C. The reason for this is, that the beam patterns of region C can be naturally reproduced assuming the so called hollow column model for the formation of the accretion structure. We of course observe that the hollow column model is similar to the one of an optically thick accretion column. The beam patterns obtained for V0332+53 definitely resemble the ones of Cen X-3 and Her X-1, which Ute Kraus et al. already discussed in the framework of a hollow column model.

More specifically, our findings on beam patterns properly reproduce all the different emission features (radiation coming from the wall, from a halo on the neutron star or reprocessed in the upper accretion stream) expected from the model and therefore

reinforce the idea of the formation of a hollow column in these systems.

However, a number of open questions remains: can we really assume symmetric emission regions at the poles? And is the configuration of the two misaligned magnetic poles stable? Is the hollow column model universal or should other models be invoked for other sources?

To answer those questions and to confirm the method of pulse profile decomposition, as well as the idea of the model of a hollow accretion model, it is necessary to conduct further analysis on a larger sample of sources.

Bibliography

Abbott, B., et al. 2008, The Astrophysical Journal, Issue 1, 683, L45

Basko, M. M., & Sunyaev, R. A. 1976, Monthly Notices of the Royal Astronomical Society, 175, 395

Bildsten, L., et al. 1997, , 113, 367

Blum, S., & Kraus, U. 2000, Astrophysical Journal, 529, 968

Coe, M. J. 2000, in Astronomical Society of the Pacific Conference Series, Vol. 214, IAU Colloq. 175: The Be Phenomenon in Early-Type Stars, ed. M. A. Smith, H. F. Henrichs, & J. Fabregat, 656–+

Coe, M. J., Haigh, N. J., & Reig, P. 2000, Monthly Notices of the Royal Astronomical Society, 314, 290

Duncan, R. C., & Thompson, C. 1992, , 392, L9

Ghosh, P., & Lamb, F. K. 1978, , 223, L83

—. 1979a, , 232, 259

—. 1979b, , 234, 296

Ghosh, P., Pethick, C. J., & Lamb, F. K. 1977, , 217, 578

Giacconi, R., Gursky, H., Kellogg, E., Schreier, E., & Tananbaum, H. 1971, , 167, L67+

Hanuschik, R. W. 1996, Astronomy and Astrophysics, 308, 170

Hewish, A., Bell, S. J., Pilkington, J. D. H., Scott, P. F., & Collins, R. A. 1968, , 217, 709

I. Caballero, D. 2009, PhD thesis, Eberhard Karls Universität Tübingen

Klochkov, D. 2007, PhD thesis, Eberhard Karls Universität Tübingen

Kraus, U. 2001, Astrophysical Journal, 563, 289

Kraus, U., Blum, S., Schulte, J., Ruder, H., & Meszaros, P. 1996, Astrophysical Journal, 467, 794

Kraus, U., Nollert, H., Ruder, H., & Riffert, H. 1995, Astrophysical Journal, 450, 763

Kraus, U., Zahn, C., Weth, C., & Ruder, H. 2003, Astrophysical Journal, 590, 424

Kretschmar, P. 2006, PhD thesis, Eberhard Karls Universität Tübingen

Kreykenbohm, I., et al. 2005, Astronomy and Astrophysics, 433, L45

Kreykenbohm, I., et al. 2006, in ESA Special Publication, Vol. 604, The X-ray Universe 2005, ed. A. Wilson, 275–+

Lamb, F. K., Pethick, C. J., & Pines, D. 1973, , 184, 271

Liu, Q. Z., van Paradijs, J., & van den Heuvel, E. P. J. 2006, Astronomy and Astrophysics, 455, 1165

Longair, M. S. 2002, High energy astrophysics. Vol.2: Stars, the galaxy and the interstellar medium, ed. Longair, M. S.

—. 2004, High energy astrophysics. Vol.1: Particles, photons and their detection, ed. Longair, M. S.

Mereghetti, S. 2001, X-ray Astronomy: Stellar Endpoints, AGN, and the Diffuse X-ray Background, 599, 219

Meszaros, P. 1984a, , 38, 325

—. 1984b, Space Science Reviews, 38, 325

Mowlavi, N., et al. 2006, Astronomy and Astrophysics, 451, 187

Negueruela, I. 1998, Astronomy and Astrophysics, 338, 505

Okazaki, A. T., & Negueruela, I. 2001, Astronomy and Astrophysics, 377, 161

Oppenheimer, J. R., & Volkoff, G. M. 1939, Physical Review, 55, 374

P. A. Charles, F. D. S. 1995, Exploring the X-ray Universe (Cambridge University Press)

Pottschmidt, K., et al. 2005, The Astrophysical Journal, Issue 1, 634, L97

Pringle, J. E., & Rees, M. J. 1972, , 21, 1

Quirrenbach, A., et al. 1997, Astrophysical Journal, 479, 477

Riffert, H., & Meszaros, P. 1988, Astrophysical Journal, 325, 207

Riffert, H., Nollert, H., Kraus, U., & Ruder, H. 1993, Astrophysical Journal, 406, 185

Schönherr, G. 2007, PhD thesis, Eberhard Karls Universität Tübingen

Stella, L., White, N. E., Davelaar, J., Parmar, A. N., Blissett, R. J., & van der Klis, M. 1985, The Astrophysical Journal, Issue 1, 288, L45

Stella, L., White, N. E., & Rosner, R. 1986, Astrophysical Journal, 308, 669

Trümper, J., Pietsch, W., Reppin, C., Voges, W., Staubert, R., & Kendziorra, E. 1978, The Astrophysical Journal, Issue 1, 219, L105

Trümper, J., Sacco, B., Pietsch, W., Reppin, C., Kendziorra, E., & Staubert, R. 1977, Mitteilungen der Astronomischen Gesellschaft Hamburg, 42, 120

Trümper, J. E., & Hasinger, G. 2008, The Universe in X-Rays, ed. Trümper, J. E. & Hasinger, G.

Tsygankov, S. S., Lutovinov, A. A., Churazov, E. M., & Sunyaev, R. A. 2006, Monthly Notices of the Royal Astronomical Society, 371, 19

Tsygankov, S. S., Lutovinov, A. A., & Serber, A. V. 2010, Monthly Notices of the Royal Astronomical Society, 401, 1628

U. Kraus, S. B. 2007, 185

Unsöld, A., & Baschek, B. 1999, Der neue Kosmos. Einführung in die Astronomie und Astrophysik., ed. Unsöld, A. & Baschek, B.

Zhang, S., Qu, J., Song, L., & Torres, D. F. 2005, The Astrophysical Journal, Issue 1, 630, L65

Ziolkowski, J. 2002, Memorie della Societa Astronomica Italiana, 73, L1038

Zwicky, F. 1938, , 88, 522

Online references

The UHURU Satellite, *NASA*:
http://heasarc.gsfc.nasa.gov/docs/uhuru/uhuru.html
Visited: August 2010

Rossi X-Ray Timing Explorer, *NASA*:
http://heasarc.gsfc.nasa.gov/docs/xte/XTE.html
Visited: August 2010

The Rossi X-ray Timing Explorer Learning Center, *NASA*:
http://heasarc.nasa.gov/docs/xte/learning_center
Visited: August 2010

NASA's High Energy Astrophysics Science Archive Research Center, *NASA*:
http://heasarc.gsfc.nasa.gov
Visited: August 2010

Particle Effects on the ISGRI Instrument On-Board the INTEGRAL Satellite, *A. Claret*:
http://hal.archives-ouvertes.fr/docs/00/03/04/06/PDF/PC3paper.pdf
Visited: August 2010

JEM-X, *ESA*:
http://sci.esa.int/science-e/www/object/index.cfm?fobjectid=31175
&fbodylongid=721
Visited: August 2010

NASA Browse, *NASA*:
http://heasarc.gsfc.nasa.gov/W3Browse/
Visited: August 2010

The ABC of XTE. *NASA*:
http://heasarc.nasa.gov/docs/xte/abc/contents.html
Visited: August 2010

The RXTE cook book, *NASA*:
http://heasarc.gsfc.nasa.gov/docs/xte/recipes/cook_book.html
Visited: August 2010

Jörn's X-Ray Data Analysis Pages, *Jörn Wilms*:
http://pulsar.sternwarte.uni-erlangen.de/wilms/research/analysis/rxte/standard.html
Visited: August 2010

Pulsars, *Lifeng*:
http://lifeng.lamost.org/courses/astrotoday/CHAISSON/AT322/HTML/AT32202.HTM
Visited: August 2010

Pulsar Properties, *National Radio Astronomy Observatory*:
http://www.cv.nrao.edu/course/astr534/images/ PSRs_pulsar_sketch.png
Visited: August 2010

Inverse Compton X-rays from relativistic flare leptons, *University of Wisconsin, Department of Astronomy*:
http://www.astro.wisc.edu/~bank/img/inversecompton.jpg
Visited: August 2010

Pair production, *Absolute Astronomy*:
http://image.absoluteastronomy.com/images/encyclopediaimages/p/pa/pairproduction.png
Visited: August 2010

University of Oregon, Department of Physics:
http://physics.uoregon.edu/~jimbrau/BrauImNew/Chap20/FG20_21.jpg
Visited: August 2010

Accretion in Binary Systems and Stellar Outbursts, *C. Palma, Department of Astronomy and Astrophysics*:
https://www.e-education.psu.edu/astro801/content/l6_p6.html
Visited: August 2010

Wind-fed accretion, *J. Poutanen*:
http://ttt.astro.su.se/groups/head//sara/img44.gif
Visited: August 2010

RXTE Learning Center: RXTE Discoveries, *NASA*:
http://heasarc.gsfc.nasa.gov/docs/xte/learning_center/gifs/discover/xte.jpg
Visited: August 2010

Pulsars, magnetars and RRATs, *D. Manchester, newsletter ATNF*:
http://www.atnf.csiro.au/news/newsletter/jun06/RRATs.htm
Visited: August 2010

Appendix A

Tables

ObsID	time	exposure	data format	EA	electron
90014-01-01-00	2005-01-08	1281	SB_62us_0_17_500ms SB_62us_18_49_500ms E_62us_32M_50_1s	EA1 EA2 EA7	0.3
90014-01-01-01	2005-01-11	3523	SB_62us_0_17_500ms SB_62us_18_49_500ms E_62us_32M_50_1s	EA1 EA2 EA7	
90014-01-01-02	2005-01-11	1368	SB_62us_0_17_500ms SB_62us_18_49_500ms E_62us_32M_50_1s	EA1 EA2 EA7	0.3
90014-01-01-03	2005-01-10	10437	SB_62us_0_17_500ms SB_62us_18_49_500ms E_62us_32M_50_1s E_500us_64M_0_1s	EA1 EA2 EA7 EA7	
90014-01-01-04	2005-01-11	3383	SB_62us_0_17_500ms SB_62us_18_49_500ms E_62us_32M_50_1s	EA1 EA2 EA7	0.3
90014-01-01-05	2005-01-11	2906	SB_62us_0_17_500ms SB_62us_18_49_500ms E_62us_32M_50_1s	EA1 EA2 EA7	0.3
90014-01-01-06	2005-01-08	1844	SB_62us_0_17_500ms SB_62us_18_49_500ms E_62us_32M_50_1s	EA1 EA2 EA7	0.3

90014-01-02-00	2005-01-16	10550	E_125us_64M_50_1s SB_125us_0_49_1s	EA1 EA3	0.3
90014-01-02-03	2005-01-15	1190	E_125us_64M_50_1s SB_125us_0_49_1s	EA1 EA3	0.3
90014-01-02-08	2005-01-18	3485	E_125us_64M_50_1s SB_125us_0_49_1s	EA1 EA3	0.2
90014-01-02-10	2005-01-17	2821	E_125us_64M_50_1s SB_125us_0_49_1s	EA1 EA3	0.2
90014-01-02-13	2005-01-20	8352	E_125us_64M_50_1s SB_125us_0_49_1s	EA1 EA3	0.3
90014-01-02-15	2005-01-19	2708	E_125us_64M_50_1s SB_125us_0_49_1s	EA1 EA3	0.3
90014-01-03-00	2005-01-21	2353	E_125us_64M_50_1s SB_125us_0_49_1s	EA1 EA3	0.3
90014-01-03-01	2005-01-23	2816	E_125us_64M_50_1s SB_125us_0_49_1s	EA1 EA3	0.15
90014-01-03-02	2005-01-24	19635	E_125us_64M_50_1s SB_125us_0_49_1s	EA1 EA3	0.15
90014-01-03-03	2005-01-25	6937	E_125us_64M_50_1s SB_125us_0_49_1s	EA1 EA3	0.15
90014-01-04-00	2005-01-28	2741	E_125us_64M_50_1s SB_125us_0_49_1s	EA1 EA3	0.15
90014-01-04-01	2005-01-29	990	E_125us_64M_50_1s SB_125us_0_49_1s	EA1 EA3	0.15
90014-01-04-02	2005-01-31	1152	E_125us_64M_50_1s SB_125us_0_49_1s E_500us_64M_0_1s	EA1 EA3 EA7	0.15
90014-01-04-03	2005-02-02	863	E_125us_64M_50_1s SB_125us_0_49_1s	EA1 EA3	0.15
90014-01-05-00	2005-02-04	862	E_125us_64M_0_1s	EA1	0.1
90014-01-05-01	2005-02-06	8515	E_125us_64M_0_1s	EA1	0.1
90014-01-05-02	2005-02-08	2861	E_125us_64M_0_1s	EA1	0.1
90014-01-05-03	2005-02-09	674	E_125us_64M_0_1s	EA1	0.1

90014-01-05-04	2005-02-06	1700	E_125us_64M_0_1s	EA1	0.1
90014-01-05-05	2005-02-06	2152	E_125us_64M_0_1s	EA1	0.1
90014-01-05-06	2005-02-10	1863	E_125us_64M_0_1s E_500us_64M_0_1s	EA1 EA7	0.1
90014-01-06-00	2005-02-13	2816	E_125us_64M_0_1s	EA1	0.1
90014-01-06-01	2005-02-15	1871	E_125us_64M_0_1s	EA1	0.1
90014-01-06-02	2005-02-16	2494	E_125us_64M_0_1s	EA1	0.1
90014-01-06-03	2005-02-17	1630	E_125us_64M_0_1s	EA1	0.1
90014-01-07-00	2005-02-23	3612	E_125us_64M_0_1s	EA1	0.1
90014-01-07-01	2005-02-18	2035	E_125us_64M_0_1s	EA1	0.1
90014-01-07-02	2005-02-19	1286	E_125us_64M_0_1s	EA1	0.1
90014-01-07-03	2005-02-19	2393	E_125us_64M_0_1s	EA1	0.1
90014-01-07-04	2005-02-21	2637	E_125us_64M_0_1s	EA1	0.1
90014-01-08-00	2005-02-25	3041	E_125us_64M_0_1s	EA1	0.1
90014-01-08-01	2005-02-27	2826	E_125us_64M_0_1s	EA1	0.1
90014-01-08-02	2005-03-01	2722	E_125us_64M_0_1s	EA1	0.1
90014-01-08-03	2005-03-03	2557	E_125us_64M_0_1s	EA1	0.1

Table A.1: Observations P90014

ObsID	time	exposure	data format	EA	electron
90089-11-01-02	2004-12-01	2820	E_125us_64M_0_1s	EA1	0.15
90089-11-01-03	2004-12-01	3108	E_125us_64M_0_1s E_500us_64M_0_1s	EA1 EA7	0.15
90089-11-01-04	2004-12-02	2950	E_125us_64M_0_1s	EA1	0.15
90089-11-02-00	2004-12-03	13610	E_125us_64M_0_1s	EA1	0.15
90089-11-02-01	2004-12-04	2030	E_125us_64M_0_1s	EA1	0.15
90089-11-02-02	2004-12-04	1457	E_125us_64M_0_1s	EA1	0.15

90089-11-02-03	2004-12-04	14036	E_125us_64M_0_1s	EA1	0.15
90089-11-02-04	2004-12-05	3512	E_125us_64M_0_1s	EA1	0.15
90089-11-02-05	2004-12-04	1789	E_125us_64M_0_1s	EA1	0.15
90089-11-02-06	2004-12-04	2372	E_125us_64M_0_1s	EA1	0.15
90089-11-02-07	2004-12-05	1906	E_125us_64M_0_1s	EA1	0.15
90089-11-02-08	2004-12-07	2735	E_125us_64M_0_1s E_500us_64M_0_1s	EA1 EA7	0.15
90089-11-02-09	2004-12-06	3236	E_125us_64M_0_1s	EA1	0.15
90089-11-02-10	2004-12-05	3422	E_125us_64M_0_1s	EA1	0.15
90089-11-03-03	2004-12-13	1401	E_125us_64M_0_1s	EA1	0.3
90089-11-03-04	2004-12-14	3317	E_125us_64M_0_1s	EA1	0.3
90089-11-03-05	2004-12-16	2176	E_125us_64M_0_1s	EA1	0.3
90089-11-04-01	2004-12-18	1922	E_125us_64M_0_1s	EA1	0.3
90089-11-04-03	2004-12-19	1451	E_125us_64M_0_1s	EA1	0.3
90089-11-04-04	2004-12-20	3588	E_125us_64M_0_1s	EA1	0.4
90089-11-04-05	2004-12-22	2555	SB_62us_0_17_500ms SB_62us_18_49_500ms E_62us_32M_50_1s	EA1 EA2 EA7	0.4
90089-11-05-01	2004-12-25	3639	SB_62us_0_17_500ms SB_62us_18_49_500ms E_62us_32M_50_1s	EA1 EA2 EA7	0.5
90089-11-05-02	2004-12-26	1982	SB_62us_0_17_500ms SB_62us_18_49_500ms E_62us_32M_50_1s	EA1 EA2 EA7	0.4

Table A.2: Observations P90089

ObsID	time	exposure	data format	EA	electron

90427-01-01-01	2004-12-29	2248	SB_62us_0_17_500ms SB_62us_18_49_500ms E_62us_32M_50_1s	EA1 EA2 EA7	0.4
90427-01-01-02	2004-12-29	2187	SB_62us_0_17_500ms SB_62us_18_49_500ms E_62us_32M_50_1s	EA1 EA2 EA7	0.4
90427-01-01-03	2004-12-30	2259	SB_62us_0_17_500ms SB_62us_18_49_500ms E_62us_32M_50_1s	EA1 EA2 EA7	0.4
90427-01-02-00	2005-01-04	912	SB_62us_0_17_500ms SB_62us_18_49_500ms E_62us_32M_50_1s	EA1 EA2 EA7	0.3
90427-01-02-01	2005-01-05	838	SB_62us_0_17_500ms SB_62us_18_49_500ms E_62us_32M_50_1s	EA1 EA2 EA7	0.3
90427-01-02-02	2005-01-06	887	SB_62us_0_17_500ms SB_62us_18_49_500ms E_62us_32M_50_1s	EA1 EA2 EA7	0.3
90427-01-02-03	2005-01-06	2901	SB_62us_0_17_500ms SB_62us_18_49_500ms E_62us_32M_50_1s	EA1 EA2 EA7	0.3
90427-01-03-00	2005-01-14	16349	E_125us_64M_50_1s SB_125us_0_49_1s	EA1 EA3	0.3
90427-01-03-01	2005-01-15	10428	E_125us_64M_50_1s SB_125us_0_49_1s	EA1 EA3	0.2
90427-01-03-02	2005-01-15	15155	E_125us_64M_50_1s SB_125us_0_49_1s	EA1 EA3	0.2
90427-01-03-05	2005-01-16	13971	E_125us_64M_50_1s SB_125us_0_49_1s	EA1 EA3	0.2
90427-01-03-06	2005-01-17	12618	E_125us_64M_50_1s SB_125us_0_49_1s	EA1 EA3	0.2
90427-01-03-09	2005-01-18	13325	E_125us_64M_50_1s SB_125us_0_49_1s	EA1 EA3	0.2

90427-01-03-11	2005-01-18	10499	E_125us_64M_50_1s SB_125us_0_49_1s	EA1 EA3	0.2
90427-01-03-12	2005-01-19	10073	E_125us_64M_50_1s SB_125us_0_49_1s	EA1 EA3	0.2
90427-01-04-00	2005-02-12	8284	E_125us_64M_0_1s	EA1	0.1
90427-01-04-01	2005-02-15	8225	E_125us_64M_0_1s	EA1	0.1
90427-01-04-02	2005-02-13	14769	E_125us_64M_0_1s	EA1	0.1
90427-01-04-03	2005-02-13	8758	E_125us_64M_0_1s	EA1	0.1
90427-01-04-04	2005-02-12	10143	E_125us_64M_0_1s	EA1	0.1
90427-01-04-05	2005-02-13	3545	E_125us_64M_0_1s	EA1	0.1

Table A.3: Observations P90427

ObsID	time	exposure	energy channels	pulse period
90089-11-02-08	2004-12-07	2735	0-17 18-49 50-71 72-255	4.3752085 4.3757016 4.3759601 4.3756859
90089-11-03-04	2004-12-14	3317	0-17 18-49 50-71 72-255	4.3751904 4.3751910 4.3752260 4.3749300
90089-11-04-03	2004-12-19	1451	0-17 18-49 50-71 72-255	4.3747110 4.3747428 4.3747111 4.3746414
90427-01-01-01	2004-12-29	2248	0-17 18-49 50-71 72-255	4.3757571 4.3757564 4.3757564 4.3758611

90427-01-02-02	2005-01-06	887	0-17 18-49 50-71 72-255	4.3757841 4.3756827 4.3756754 4.3759694
90014-01-01-04	2005-01-11	3383	0-17 18-49 50-71 72-255	4.3749142 4.3750846 4.3750312 4.3751261
90014-01-05-01	2005-02-06	8515	0-17 18-49 50-71 72-255	4.3754772 4.3754362 4.3754426 4.374884
90427-01-04-04	2005-02-13	10143	0-17 18-49 50-71 72-255	4.3751692 4.3751703 4.3755276 4.4426217

Table A.4: Observations for Pulse Profile Decomposition: lightcurves with background subtracted and bary and binary corrected

Appendix B

Geometry plots for Region G

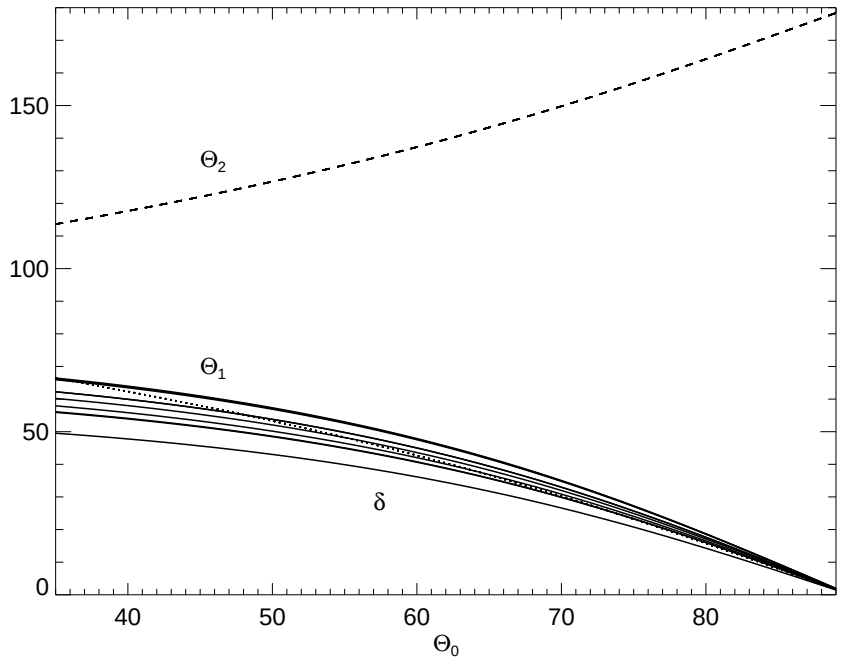

Figure B.1: Geometric solution for region G: Position of the two magnetic poles Θ_1 and Θ_2 as a function of the observation angle Θ_0 and the shift δ from the antipodal position for a selection of observations covering the whole timespan of the outburst. We didn't plot all observations because otherwise the position of the first pole cannot be identified.

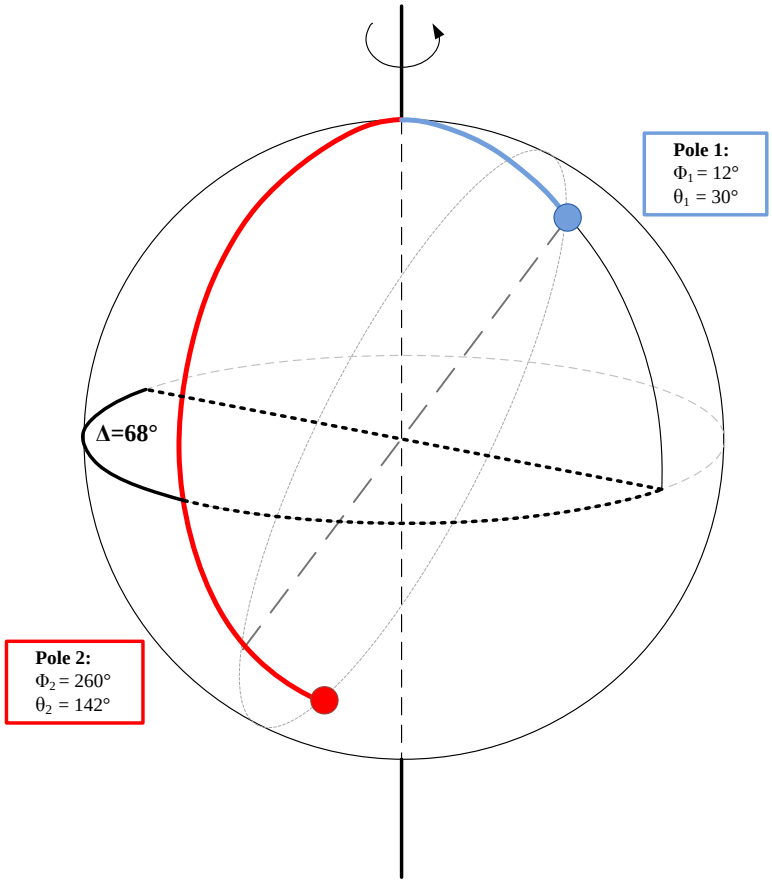

Figure B.2: Position of the two magnetic poles for the solution of region G and for an observation angle of $\Theta_{\rm obs} = 70°$

Acknowledgment

I thank all the people who supported me, especially

my supervisor *Manami Sasaki* as well as *Dmitry Klochkov* who helped me with many problems,

my prof *Andrea Santangelo*,

all the people from the institut who I always felt free to ask all kind of stupid questions,

and last but not least

my family and all my friends: you are the best, especially the "gang" who is going to **Ibiza** ;)

Erklärung zur Selbstverfassung:

Ich erkläre, dass ich die vorliegende Diplomarbeit mit dem Titel *Pulse Profile Decomposition of the Accreting X-ray Pulsar V0332+53* selbstständig verfasst habe und dass ich dazu keine anderen als die angegebenen Quellen und Hilfsmittel verwendet habe.

Ort, Datum Unterschrift